ORNL/Sub/87-SB045/2

ANALYTICAL AND EXPERIMENTAL EVALUATION OF JOINING SILICON CARBIDE TO SILICON CARBIDE AND SILICON NITRIDE TO SILICON NITRIDE FOR ADVANCED HEAT ENGINE APPLICATIONS PHASE II

Glenn J. Sundberg
Ara M. Vartabedian
Jon A. Wade
Charles S. White

Date Published-October 1994

FINAL REPORT

Prepared by Norton Company
Advanced Ceramics
Goddard Road
Northboro, Massachusetts 01532-1545

Funded by
Propulsion System Materials Program
Office of Transportation Technologies
the Assistant Secretary for Energy Efficiency
and Renewable Energy
U.S. Department of Energy
EE 51 01 00 0

Subcontract No. 86X-SB045C

for
OAK RIDGE NATIONAL LABORATORY
Oak Ridge, Tennessee 37831
managed by
MARTIN MARIETTA ENERGY SYSTEMS, INC.
for the
U.S. DEPARTMENT OF ENERGY
under Contract DE-AC05-84OR21400

DISCLAIMER

Portions of this document may be illegible in electronic image products. Images are produced from the best available original document.

TABLE OF CONTENTS

Research sponsored by the U.S. Department of Energy, Assistant Secretary for Energy Efficiency and Renewable Energy, Office of Transportation Technologies, as part of the Ceramic Technology Project of the Propulsion System Materials Program, under contract DE-AC05-84OR21400 with Martin Marietta Energy Systems, Inc.

1 EXECUTIVE SUMMARY

Joins of hot isostatically pressed (HIP'ed) Si_3N_4-4wt% Y_2O_3 (NCX-5100 family) and sintered Beta-SiC (NCX-4500) developed during Phase I of the contract demonstrated attractive mechanical properties for advanced heat engine applications.[1] An experimental database was developed for both materials based upon limited MOR and buttonhead tensile tests. Within the limitations of this database, analytical/numerical models were developed for prediction of join life. The purpose of joining Phase II was to develop joining technologies for HIP'ed Si_3N_4 with 4wt% Y_2O_3 (NCX-5101) and for a siliconized SiC (NT230) for various geometries including: butt joins, curved joins and shaft to disk joins. In addition, more extensive mechanical characterization of silicon nitride joins to enhance the predictive capabilities of the analytical/numerical models for structural components in advanced heat engines was provided. Mechanical evaluation were performed by: flexure strength at 22°C and 1370°C, stress rupture at 1370°C, high temperature creep, 22°C tensile testing and spin tests.

Silicon nitride joins with excellent room temperature and high temperature (1370°C) mechanical properties were developed during Joining, Phase I using an albeit simple, planar butt join geometry. Certain heat engine components could benefit from development of curved join geometries with mechanical performance similar to the planar butt joins. Consequently, considerable effort during Joining Phase II was spent on development and testing of silicon nitride curved joins.

The selection of joining methods was guided by an objective to produce join interlayers with properties similar to the parent materials. The method for silicon nitride joining developed within this contract resulted from improvements upon the approach used during Phase I and incorporation of independent developmental efforts by Norton Advanced Ceramics (NAC) Division of Saint-Gobain/Norton Industrial Ceramics Corporation (SGNICC). The silicon nitride joining method consisted of the following steps.

NCX-5101 Si_3N_4, formed by cold isostatic pressing and green machining into curved shapes, was joined in the green state prior to HIP densification. Join interlayers were made from various types of aqueous dispersions (or slips) of NCX-5101 powder, or made without slip. The aqueous slips although applied similarly, differed in method of preparation, additive content and the manner in which silicon nitride green joins were pre-conditioned.

Improved green strength was desired for silicon nitride joins to minimize the handling rejections experienced prior to hot isostatic pressing during Phase I of the contract. Curved silicon nitride joins demonstrated a 5.5-fold improvement of pre-sintered green strength compared with methods used for Phase I of the contract. The mechanical properties of the improved joining method were also measured by flexure strength tests at 22°C and 1370°C. There was no statistical difference between the 22°C and 1370°C flexure strength populations as a function of location within joined samples. The combined average 22°C flexure strength for curved silicon nitride joins was 886.3 MPa with a Weibull modulus of 16.4 as determined by 156 flexure specimens from five curved join disks. The combined average 1370°C flexure strength for curved silicon nitride joins was 516 MPa with a Weibull modulus of 16.0 as determined by 59 flexure specimens from five curved join disks. Only 1.2% of the 22°C flexure failures and 5.1% of the 1370°C flexure failures originated within the join interlayer. Shear tests of densified joins were not able to fail specimens at the join interlayer due to the high strength of joins relative to the parent material.

The demonstration of curved join quality similar to planar butt joins developed during Phase I of the contract allowed application of the joining technique to more complex shapes, such as a simulated rotor geometry. Shaft to disk joins made by the procedure developed for curved joins were ground to obtain spin test specimens. Additional joins of the shaft-to-disk configuration were used to manufacture tensile specimens to determine tensile strength of the actual spin test specimen join geometry.

Tensile strength of curved joins averaged 636 MPa with an estimated Weibull modulus of 8.2 with no failure originating from the join interlayer. The spin test specimens failed at angular velocities ranging between 17,000 and 42,530 revolutions per minute corresponding to a maximum principal stress from finite element analysis between 88.0 and 550.6 MPa. The angular velocity and stress at failure were less than predicted by the models developed within this contract due to failure origination from grinding damage. The size of surface flaws as determined by fractography were consistent with the flaw size calculated from the Griffith relationship for brittle failure of solids. This emphasizes the need for development of improved machining techniques for complex shaped structural ceramic components.

Tensile creep tests of the silicon nitride planar butt joins demonstrated behavior that was similar to the parent unjoined material. Creep was evaluated between temperature of 1250°C to 1420°C and stress between 100 and 250 MPa. Creep curves display a well defined primary creep regime with a gradual transition into secondary creep. None of the creep tests exhibited tertiary creep even though some tests were as long as 1,692 hours. A novel method of data acquisition allowed the measurement of creep strain from different positions upon the gauge length within a single creep specimen during each test. As a consequence, it was noted that the largest variations of creep strain at test termination were observed within specimens as opposed to between specimens. The percent difference of total strain at test termination between opposing halves of the parent material typically ranged from 5% to 57%. This was attributed to the inherent variable nature of creep within typical ceramic materials. Five of the 29 failures during tensile creep tests, originated within the join interlayer. Failed specimens exhibited cavitation at bi-grain junctions and wedge cracking at triple grain junctions. The creep data was incorporated into three models to develop a predictive tool that could be utilized for specimens of different geometry.

The widely accepted Norton's (or Arrhenius) equation approach was first considered to model creep behavior. Values of activation energy (Q), stress exponent (n) and material constant (A) were determined for the creep experiments using an iterative procedure. This was done to determine a single estimate of these parameters for the entire creep matrix from which a reasonable, good correlation of predicted and actual creep strain rate was obtained.

The above model used the minimum creep rate for a given experiment since this represented the creep rate at failure or test suspension within the secondary creep regime.

A less widely accepted approach, but interesting alternative to the Arrhenius equation approach, was to model the creep behavior theta projection. The theta projection method described time dependent creep strain with a series of shape terms to reproduce the creep strain curve at a specific stress and temperature. One term of the equation represented the decaying primary component and another an accelerating tertiary component of creep strain. The theta projection method deviated from classical creep modeling by defining the secondary creep regime mathematically as the resultant contribution of the tertiary and primary creep. Alternatively, the theta projection method provided a way to not only represent the experimental creep curves, but to interpolate to other testing conditions as well. However, some of the experimental data were not satisfactorily fit by this method. The theta projection method is limited by a dependence upon modeling tertiary creep, which was not observed experimentally. In addition, the method requires determination of sixteen coefficients, which is excessive. The highly variable behavior within the primary creep regime experienced between specimens strongly contributed to an unacceptable error for predicted creep strain values. The third model that was applied to the data involved an internal variable. This method predicts the primary creep through the evolution of a scalar internal variable. The creep strain is determined by the integration of a system of two, first order, differential equations. Validation of the approach was obtained through comparison with the actual creep behavior of nine specimens that were tested to failure.

Creep failure modeling was facilitated by a correlation of creep strain rate with time to failure which allowed application of a Monkman-Grant relationship. It was unnecessary to plot separate curves for each temperature since a good correlation of all the experimental data was obtained with a single curve.

The development of material models above was useful only if the model could predict the performance of structural components. The Norton's law was used to predict the behavior of a notched tensile specimen which served to simulate behavior of an actual component. Reasonable prediction of the time of failure for three specimens tested under different loads was an encouraging demonstration of the value of the use of a finite element code such as ANSYS in conjunction with the Norton's law model.

Attempts to join NT230 silicon carbide began with manufacture of planar butt joins. If the planar butt join quality proved acceptable then curved join geometries were to be undertaken. The processing steps to manufacture the NT230 material were to form green components by pressure casting and subsequently pre-sinter and siliconize. This contract attempted to join like parent billets at two different stages of processing: siliconized and pre-sintered, unsiliconized. The joining approach to be evaluated borrowed from the successful silicon nitride joining attempts whereby the join interlayers were applied as aqueous dispersions, or slips, of the parent material with other additives. The aggregate bodies joined with slip were subsequently pre-sintered and siliconized.

Initial screening trials using two types of slip interlayer for joining siliconized and unsiliconized parent materials resulted with joins of lower strength than the parent materials. Join quality was affected by pronounced silicon enrichment and porosity. Additional silicon carbide joins were made to improve quality. A total of six interlayer types consisting of various mixtures of silicon carbide and other additives were applied to join both siliconized and unsiliconized parent materials. Quality of the silicon carbide joins was evaluated by room temperature flexure strength tests of specimens ground from the joined bodies. All flexure specimens failed at the join interlayer. Join strength was lower than the strength of unjoined NT230 of similar cross sectional thickness, with respective average strengths of 152 MPa and 233 MPa. Although, the joins exhibited an improved, more homogeneous distribution of silicon carbide and silicon, all of the joins lacked a contiguous network of silicon carbide that extended into the parent material. All of the join methods resulted in join interlayers that were discrete relative to the parent materials and of higher silicon concentration. The distinct interface between the join interlayer and parent material consisted largely of silicon within the join and silicon carbide within the parent material with an absence of interpenetration across the interface. In addition, voids within the join interlayer were strength limiting.

While the silicon nitride joins were produced with sufficient integrity for many applications, the lower join strength would limit its use in the more severe structural applications. Thus, the silicon carbide join quality was deemed unsatisfactory to advance to more complex, curved geometries. The silicon carbide joining methods covered within this contract, although not entirely successful, have emphasized the need to focus future efforts upon ways to obtain a homogeneous, well sintered parent/join interface prior to siliconization. In conclusion, the improved definition of the silicon carbide joining problem obtained by efforts during this contract have provided avenues for future work that could successfully obtain heat engine quality joins.

2 LIST OF TABLES

3 LIST OF FIGURES

W.B.S. Element 1.4.2.1

ANALYTICAL AND EXPERIMENTAL EVALUATION OF JOINING SILICON CARBIDE TO SILICON CARBIDE AND SILICON NITRIDE TO SILICON NITRIDE FOR ADVANCED HEAT ENGINE APPLICATIONS PHASE II

Glenn J. Sundberg
Ara M. Vartabedian
Jon A. Wade
Charles S. White

4 ABSTRACT

Techniques were developed to produce reliable silicon nitride to silicon nitride (NCX-5101) curved joins which were used to manufacture spin test specimens as a proof of concept to simulate parts such as a simple rotor. Specimens were machined from the curved joins to measure the following properties of the join interlayer: tensile strength, shear strength, 22°C flexure strength and 1370°C flexure strength. In parallel, extensive silicon nitride tensile creep evaluation of planar butt joins provided a sufficient data base to develop models with accurate predictive capability for different geometries. Analytical models applied satisfactorily to the silicon nitride joins were Norton's Law for creep strain, a modified Norton's Law internal variable model and the Monkman-Grant relationship for failure modeling. The Theta Projection method was less successful. Attempts were also made to develop planar butt joins of siliconized silicon carbide (NT230).

5 INTRODUCTION

The fabrication capabilities for silicon nitride and silicon carbide have improved since the beginning of Joining, Phase I in 1987. However, it is still difficult to fabricate reliable components of silicon nitride and silicon carbide of large size and complex geometries for heat engine applications. Two favored near net shape forming techniques, injection molding and pressure casting, suffer from limitations that become more pronounced when the thickness and complexity of the part increases. Warpage and cracking during binder removal of injection molded heat engine components still occurs. Long casting time, cracking during drying (caused by high capillary forces), density gradients and non-uniform shrinkage are limitations of pressure casting parts.

Consequently, joining of smaller sub-components of simpler geometry to manufacture a larger, complex shaped aggregate component is currently attractive. Theoretically, the reliability of components made by joining simpler shape parts can be superior to the single-part complex shape containing angles and discontinuities. Furthermore, joining is the only viable alternative when a complex component is comprised of sub-components of dissimilar composition that are each manufactured by separate processes (e.g. reinforced CMC vanes attached to a monolithic hub in a rotor).

Joining serves as an appealing solution to current fabrication problems. Methods developed during Joining, Phase I and II have been the only effective approach available to date to obtain heat engine quality joins with good strength, acceptable creep and stress rupture life at 1370°C.

Silicon nitride joins with excellent room temperature and high temperature (1370°C) mechanical properties were developed during Joining, Phase I using an albeit simple, planar butt join interlayer. Certain heat engine components could benefit from development of curved join interlayer geometries with mechanical performance similar to the planar butt joins. Consequently, considerable effort during Joining, Phase II was spent on development and testing of silicon nitride curved joins. A final evaluation of the joining method was to demonstrate performance of simulated joined rotors by spin testing.

Concurrent, with curved join development was testing of high temperature creep behavior of planar butt joins developed during Joining, Phase I to expand the database begun during Phase I for creation of valid analytical numerical models. A number of models were evaluated to develop acceptable predictive capability for silicon nitride components of different geometries subjected to complex temperature and stress fields.

Silicon carbide joining was also investigated in an attempt to create acceptable join quality for heat engine applications.

6 PROGRAM OBJECTIVES

This program had the following main objectives:

1) silicon nitride curved join development and optimization
2) silicon nitride shaft-to-disk join development
3) silicon nitride spin testing
4) silicon nitride tensile creep evaluation
5) analytical/numerical modeling for life prediction in different conditions of temperature and stress
6) silicon carbide planar (flat) butt join development
7) silicon carbide curved join development
8) silicon carbide shaft-to-disk join development
9) silicon carbide spin testing

The program was initially divided into the main tasks, as described below.

<u>Task 1.1</u> <u>Silicon Nitride Butt Joins - Creep Resistance</u>
Silicon nitride butt joins shall be evaluated in the primary and secondary or steady state regions. Creep behavior shall be determined at three temperatures and three stresses. Specimens shall be evaluated after fracture by microscopy methods to determine microstructural changes during deformation.

<u>Task 1.2</u> <u>Silicon Nitride Curved Join - Join Development</u>
Silicon Nitride - 4wt% yttria disks shall be joined to hollow rings made from the same material. Joining shall be attempted with and without a slip interlayer. Approximately 15 joined sets shall be prepared.

Join strength shall be measured by MOR in 4 point bending at 25°C and 1370°C. One shear strength measurement at 25°C and one at 1370°C shall be attempted on the whole joined disk by supporting the outer ring and loading the inner circle until failure occurs. Optical and SEM fractography shall be performed on both MOR bars and sheared parts to identify fracture mode and origin.

<u>Task 1.4</u> <u>Silicon Nitride Shaft to Disk - Join Development</u>
Ten components of a shaft to disk configuration will be fabricated. The shaft/disk assembly shall be evaluated by using microfocus x-ray radiography to detect flaws in the join interface.

<u>Task 1.4B</u> <u>Silicon Nitride Shaft to Disk - Spin Test</u>
The database developed in Phase I and the tensile test specimens prepared in this task shall be used to model fast fracture behavior of the shaft to disk join during a spin test. Five of the components prepared in Task 1.4A shall be machined into a rotor configuration and spin tested to failure using high speed photography. Following testing, fractographic analysis shall be attempted to determine fracture mode and origin. Spin test results shall be utilized to verify the analytical model.

Task 2.1A Siliconized Silicon Carbide Butt Joins
Join Development of Siliconized (dense) materials shall be joined by using slip interlayers which are subsequently sintered and siliconized. Joining shall use billets 2 X 2 X 1.5 inch. The effect of slip composition and grain size shall be evaluated. Later studies shall consist of evaluating the joining of unsiliconized bodies with slip interlayers followed by sintering and siliconization.

MOR bars shall be machined to include the joined region, then tested for join strength at 25°C and 1370°C. Results shall provide feedback to optimize slip composition and processing conditions. Control (no join) MOR bars shall also be tested. Flexural stress rupture performance at 1370°C shall be evaluated on joined materials exhibiting the best MOR performance. Optical and SEM microscopy shall be utilized to identify fracture mode and origins.

Task 2.1B Siliconized SiC Butt Joins
Creep Resistance Time dependent strain deformation in siliconized silicon carbide butt joins shall be evaluated and compared to results obtained with unjoined material. Creep deformation prediction capabilities developed in Phase I and verified with silicon nitride butt joins shall be utilized.

Task 2.2 Siliconized Silicon Carbide Curved Join - Join Development
The approach for this effort is essentially the same as described in Task 1.2 for curved silicon nitride joins. However, the siliconized silicon carbide join may be prepared by machining green (unsiliconized) material or dense (siliconized) material depending on the results from butt joining this material (Task 2.1A). Flexural and shear strengths of the join shall be measured.

Task 2.4A Siliconized Silicon Carbide Shaft to Disk - Join Development
The joining method for siliconized silicon carbide shall be as developed in Task 2.1A. The approach shall be identical to that for silicon nitride as described in Task 1.4A.

Task 2.4B Siliconized Silicon Carbide Shaft to Disk - Spin Test
The model developed in Task 1.4B shall be utilized to predict failure. Five of the components in Task 2.4A shall be spin tested to failure. Fractographic analysis of failed parts shall be utilized to determine fracture mode and origin. A database consisting of 45 MOR specimens tested at room temperature shall be utilized to predict spin performance of the component. The spin test results shall be utilized to further verify the analytical model.

During Task 2.1A, Siliconized Silicon Carbide Butt Joins - Join Development, difficulties with manufacture of heat engine quality joins could not be overcome. Consequently, the dependent Tasks 2.1B, 2.2, 2.4A and 2.4B were removed from the Statement of Work.

7 MECHANICAL EVALUATION PROCEDURE

7.1 TENSILE CREEP

7.1.1 Specimen Preparation

The tensile creep specimen is shown in Figure 1. It has a dogbone shape with grip end holes for pin loading. The specimen is 3.5" long, 0.100" thick and has a grip end width of 0.750". The gauge region is 1.00" long and 0.1" wide. A large radius transition region (radius = 1.0") was used to minimize stress concentration within the grip and transition regions. A detailed finite element study was conducted to optimize the specimen geometry. A requirement is that the highest creep strain rates should be confined to the gauge section. The finite element analysis suggests that the maximum stress at the pin hole is less than 0.9 of the stress magnitude in the gauge length (Figure 2), which is acceptable. There is a stress concentration at the surface where the transition region blends into the gauge length. The stress concentration at the transition is 1.03 which is typical of other tensile specimens[2].

7.1.2 Load Application

The typical profile included a pre-load of 20 lbs. The pre-load was maintained throughout the temperature ramp and pre-soak. After 24 hours, the load was ramped at a rate of 50 pounds per minute to 85% of the final load. The rate was then reduced to 25 pounds per minute to the final load and maintained +/- 1 pound for the duration of the test.

7.1.3 Temperature Profile

The furnaces were ramped from 22°C to the temperature of creep evaluation. The furnace was heated to 1200°C at 25°C per minute, then to soak temperature at 10°C per minute, and maintained +/- 1°C to the conclusion of the test.

7.1.4 Extensometry

Multiple laser extensometer targets are positioned about the join to determine the variation of strain rate within the region containing the join as compared with the two regions not containing the join (Figure 3). Two targets positioned at the extremities of the gauge section and two targets positioned adjacent to the join provide the comparative strain data.

A modified target (Figure 4) with a 45° bevel slot and the thickness decreased to 1.27 mm minimized the tendency for slipping as the gauge section elongates. Additionally, a longer moment arm increased the normal force along the line contact and improved the resistance to slipping. This change proved to be more effective than the original unslotted targets.

The actual strain is measured with laser dimensional sensors manufactured by Z-Mike Corporation.[3] Z-Mike model 1101 sensors were modified for hot object measurement and an increased passline extension for ten to twelve inch transmitter to object separation to accommodate the furnace. The system measurement resolution is 0.1 µm, and the measurement precision is +/- 1 µm at 1400°C. Both the laser transmitter and receiver are mounted on precision linear translation tables with one inch manual barrel micrometer drives.

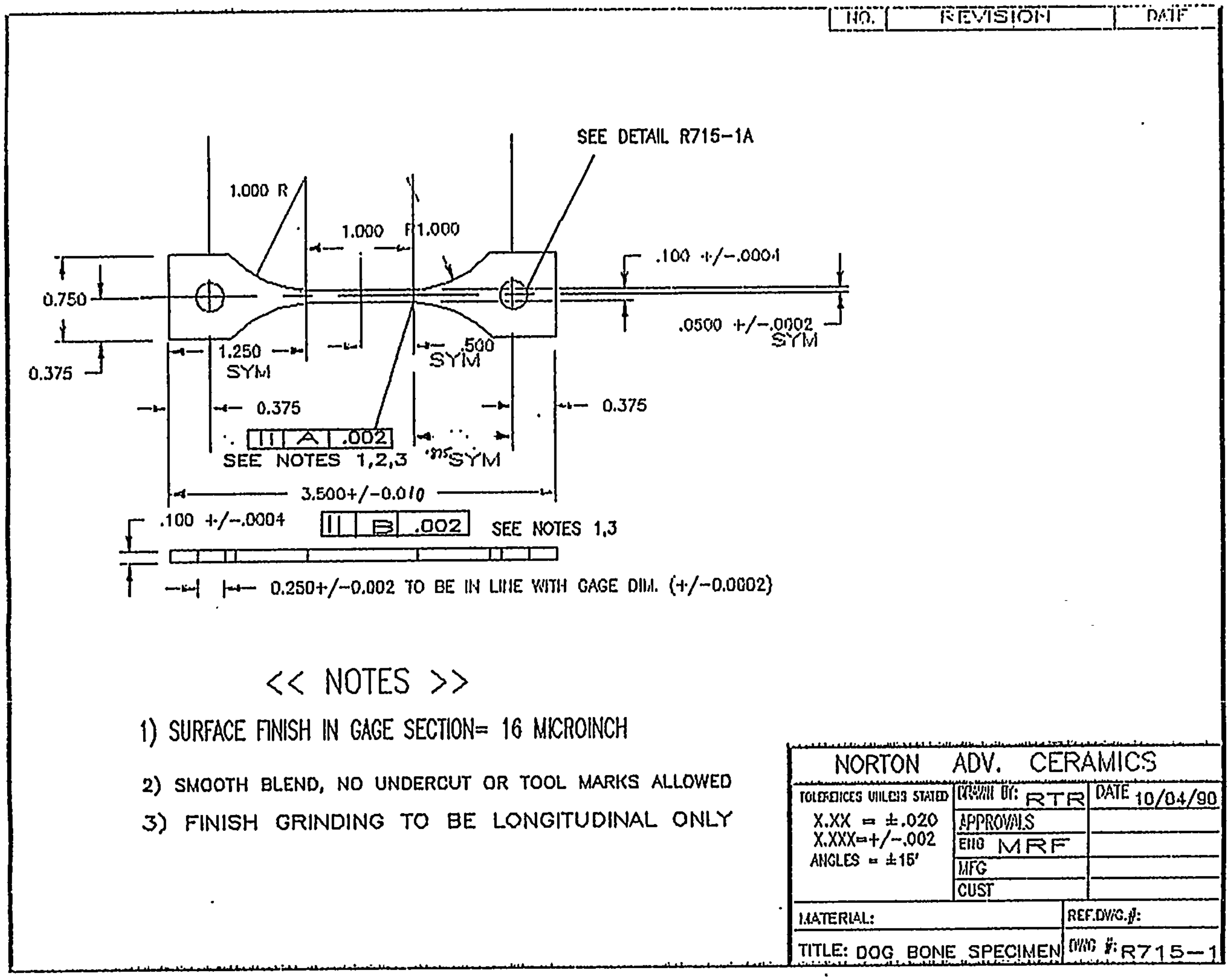

Figure 1: Tensile Creep Specimen

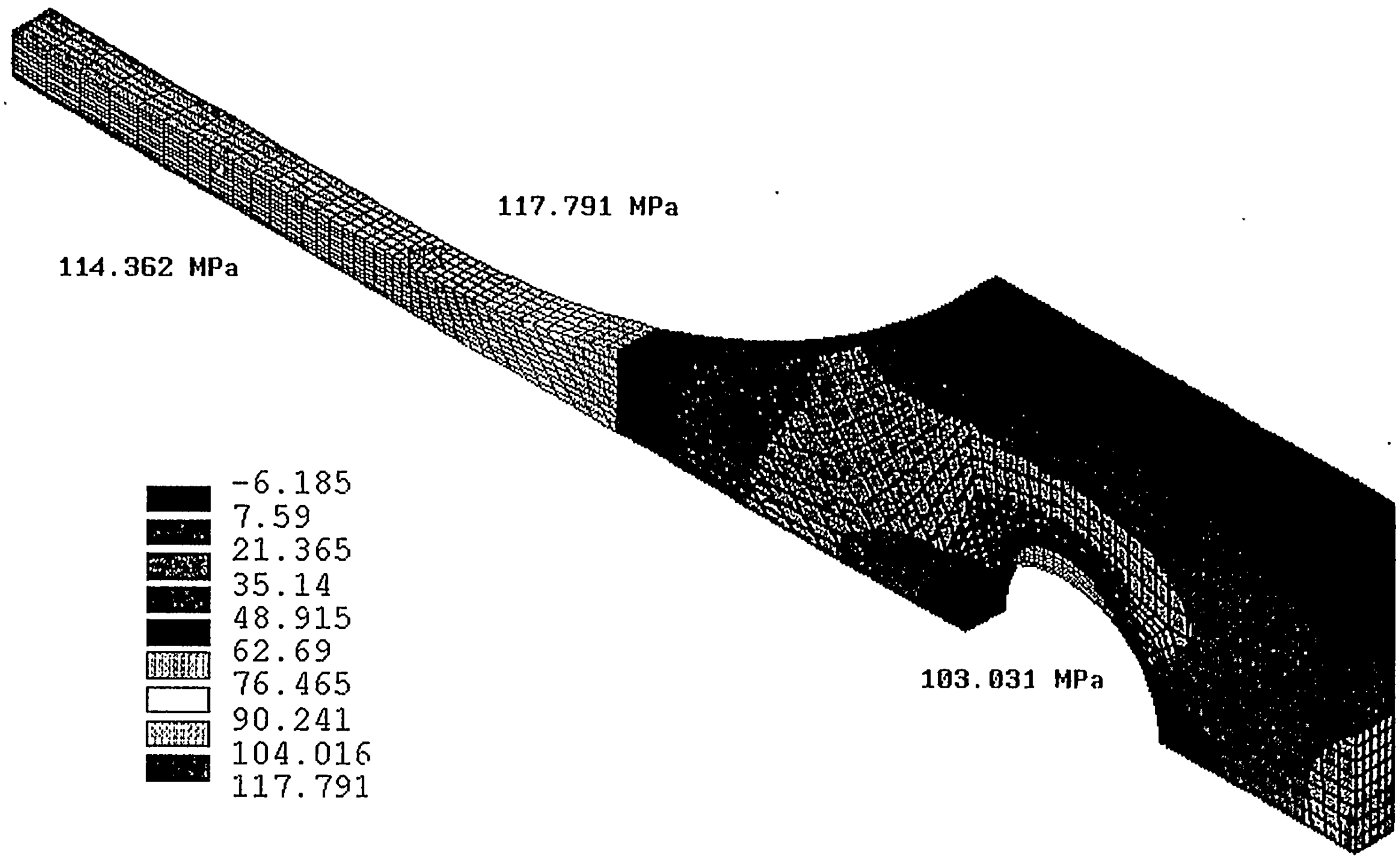

Figure 2: Contours of Maximum Principal Stress for Tensile Creep Specimen

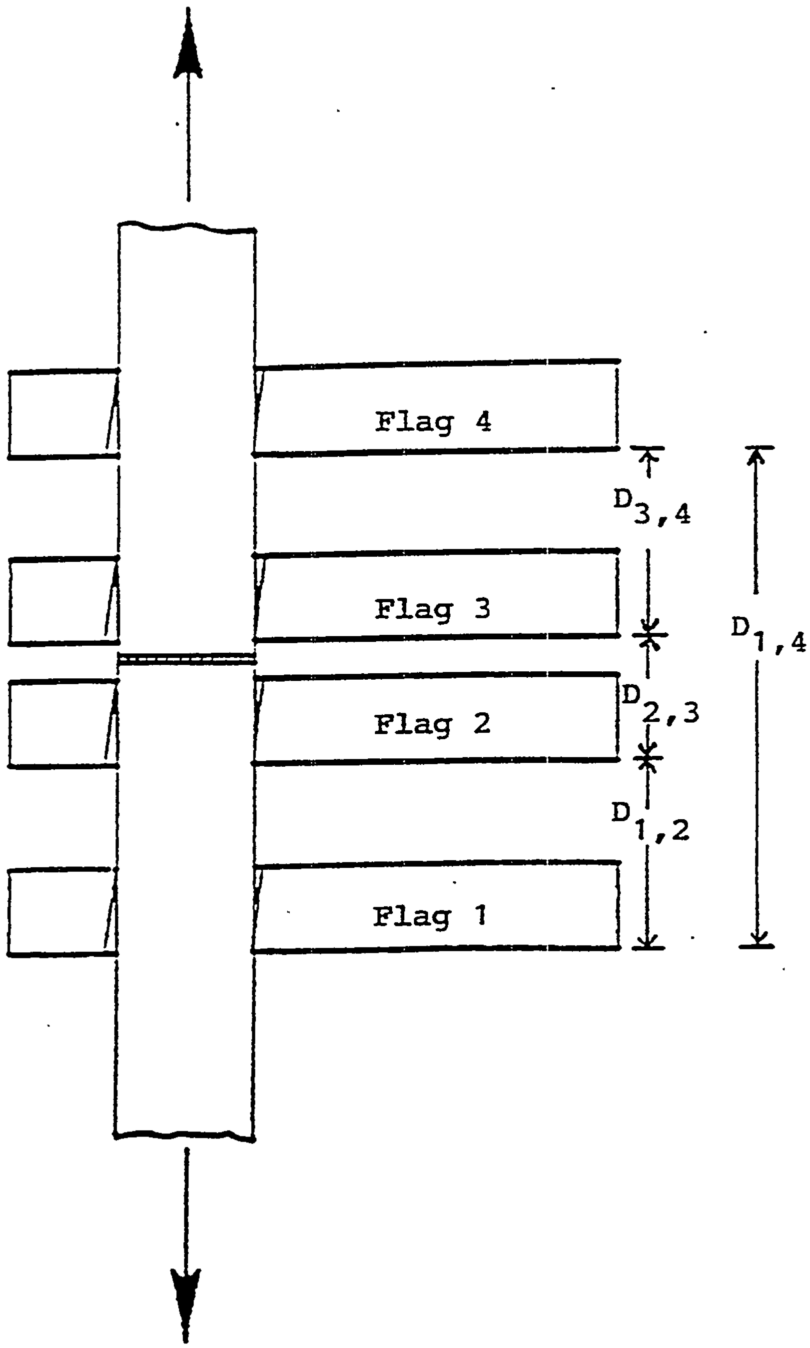

Figure 3: Extensometer Flag Arrangement

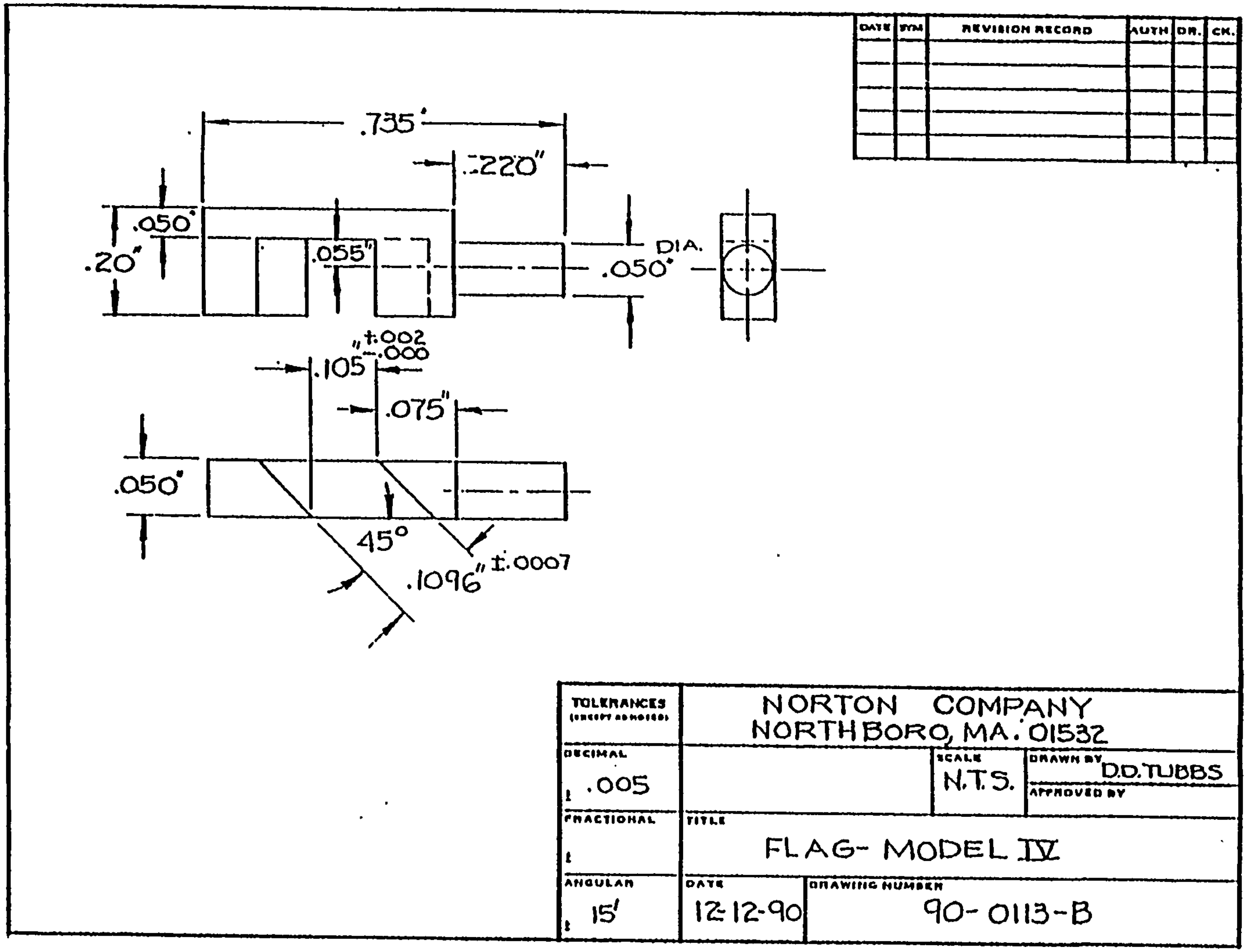

Figure 4: Laser Extensometry Target

The laser extensometry system was used to measure and store the displacement of four flags upon each tensile creep specimen (Figure 3). The relative displacement between any two flags has been used to calculate the strain of different segments of the gauge section. Creep data is reported for a specific flag couple. For example, the creep of the parent material (segments D1,2 and D3,4) and the join (segment D2,3) may be calculated independently or the combined creep of parent material and the join (segment D1,4) may be determined. In this manner, creep strain as a function of time has been plotted to compare the creep of the join interlayer and the parent material at varying temperature and applied stress.

The measurement data was conditioned and formatted in the Z-Mike-1100 processor. The system can be programmed to measure several dimensions simultaneously. Measurements were always taken between the same side of laser target pairs to allow for any uniform dimensional changes of the targets due to oxidation or other reactions at high temperature.

7.1.5 Data Acquisition

The testing supervisory computer was linked to the Z-Mike-1100 processor via synchronous RS-232 communication line. The test system control program prompts the 1100 processor for the average of the 100 most recent measurements in a moving queue. The data was parsed and logged into fields with a time stamp. The load was also logged with a time stamp in a separate file or recorded on a stripchart. At the end of a test, the data is run through an RPL procedure in RS/1[4] to check for proper column entry and deletion of errors and empty fields. A preliminary creep strain versus time plot is generated at this time to evaluate the test run. A sample curve of the raw data (Figure 5) displays creep strain for the entire gauge section (*Strain 1-4*) and the regions above and below the join (*Strain 3-4 and Strain 1-2*). The curve labeled *Strain Independent Laser Target* is used to record the linearity of the laser system over time. This curve should be near zero strain for the entire length of the test. The test is useful in distinguishing actual strain related phenomena from logging errors and is a good check of the system.

7.2 GREEN SHEAR STRENGTH

Green shear strength tests were used to guide silicon nitride curved join development to obtain a joined, pre-sintered body with improved strength. Join shear strength was measured after a pre-sintering step, prior to hot isostatic pressing on the entire green join. A disc on ring shear fixture (Figure 6) was mounted on an Instron 4206. The load rate was 0.02 inches per minute. The shear fixture had a load/support ring diameter ratio of 0.802.

7.3 FIRED SHEAR STRENGTH

The fired shear strength of curved joins were measured after completion of join development stage. Three shear test specimens were ground from each dense join by sectioning across the diameter to create three disks of 2.50 mm thickness x 70 mm diameter. This decreased the load required to fracture the dense join to a level acceptable to the testing on the Instron 4206. Five specimens were shear tested at 25°C and one at 1370°C. Two load-disc/support-ring diameter ratios were used (0.802 and 0.918) at room temperature to observe difference of failure mode.

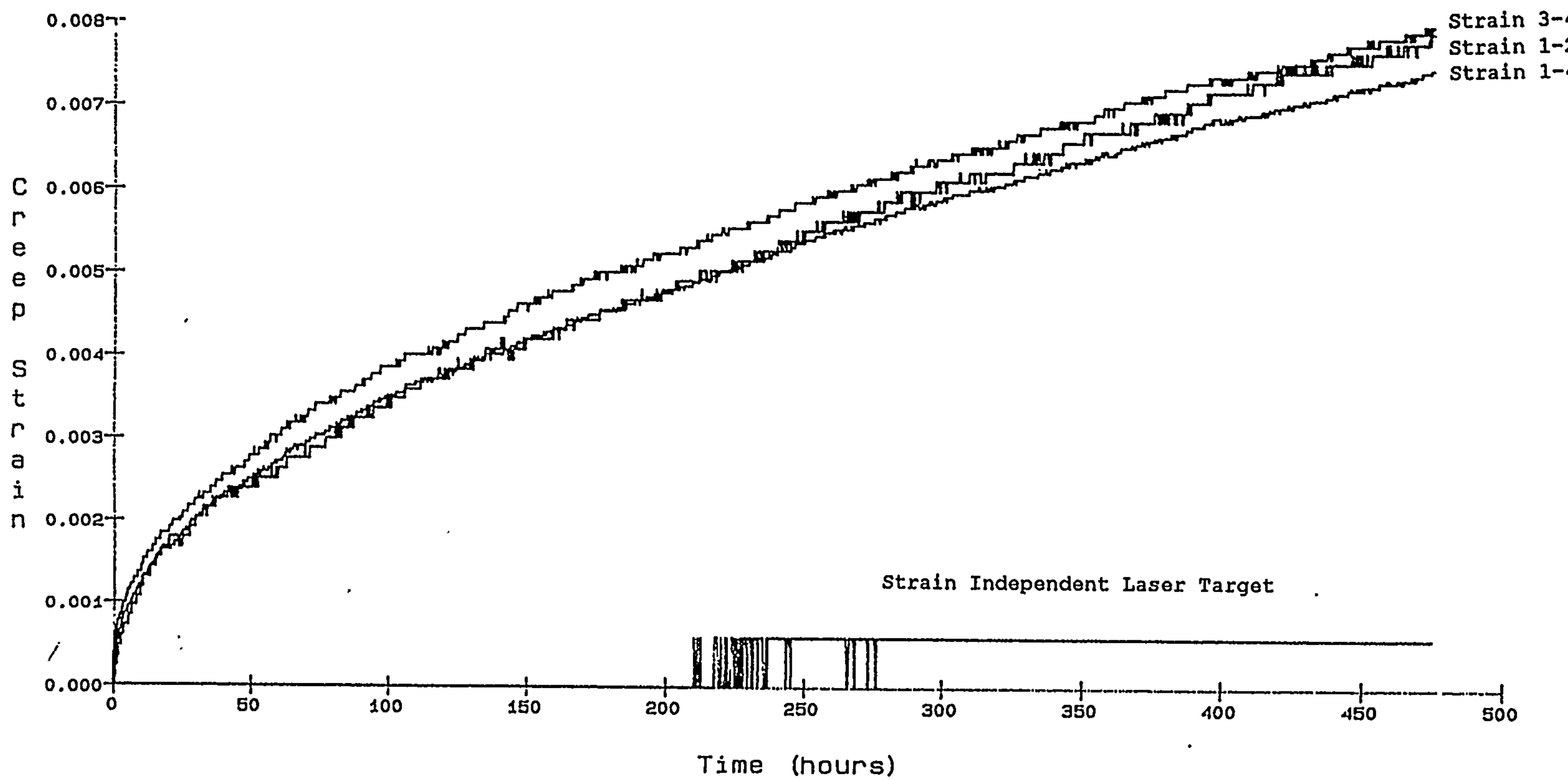

Figure 5: Creep Strain as a Function of Time

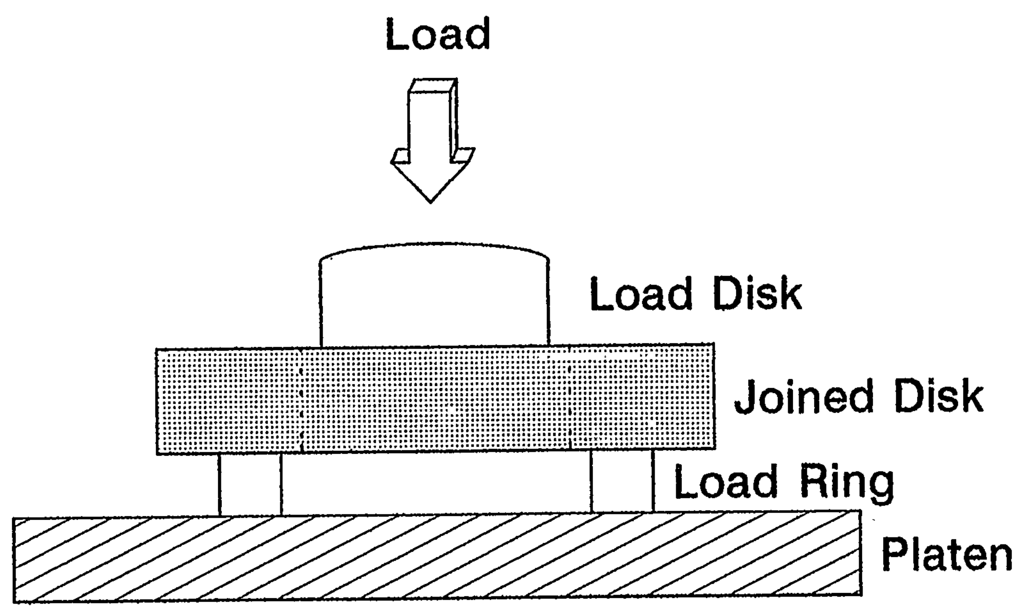

Figure 6: Disk on Ring Shear Fixture

7.4 FLEXURE STRENGTH

7.4.1 Specimen Preparation - Silicon Nitride Curved Join Development

All joins were diamond sectioned after x-ray microfocus radiography for optical inspection to determine join integrity. Additional diamond grinding yielded 12 flexure specimens per each curved join. Flexure specimens were made and tested according to the ASTMC1161-90 A geometry specifications. Deviation from the ASTMC1161-90 during tests will be explained in section 7.4.4, Flexure Strength Test Method. The join plane was located at the center of the bar, perpendicular to the longitudinal (tensile) axis of the specimen.

7.4.2 Specimen Preparation - Final Testing of Curved Silicon Nitride Joins

Experience with grinding flexure specimens from the curved joins allowed a greater yield of flexure specimens from each curved join. Thirty-two ASTMC1161-90 A-geometry flexure specimens were obtained from each curved join billet according to the configuration illustrated in Figure 7. Deviation from the ASTMC1161-90 during tests will be explained in section 7.4.4 Flexure Strength Test Method.

7.4.3 Specimen Preparation - SiC Butt Join Development

Specimens were diamond sectioned for optical inspection to determine join integrity. Additional machining yielded 15 flexure specimens per each join. Flexure specimens were made and tested according to ASTMC1161-90 B geometry specifications. Deviation from the ASTMC1161-90 during tests will be explained in section 7.4.4 Flexure Strength Test Method.

7.4.4 Test Method

Room temperature testing utilized a Sintech Model 1 test frame. An Instron 4206 test frame was used for high temperature tests. Flexure tests for silicon nitride curved join development used an outer span of 20 mm and an inner span of decreased size, 5 mm, on a rolling pin fixture to increase the probability of failure within the join. Flexure tests for silicon carbide join development used an outer span of 40 mm with the same inner of 5 mm. Flexure fixtures were manufactured from silicon carbide (NC-203) and complied with ASTMC1161-90 B. The fixture was mounted horizontally with the load applied normally, transmitted through a ball bearing, at room temperature. A hemispherical anvil was used at elevated temperatures to compensate for any loading eccentricity. The specimens were loaded at a cross-head speed of 0.20 mm/minute and data acquisition was handled by automated machine control. Specimen width and thickness was measured and recorded using a digital micrometer to accuracy of 0.01 mm. Peak load, break load, peak stress, and percent strain at break data were recorded and saved on computer file. Elevated temperature testing was performed in air using a CM Rapid Temp moly-disilicide furnace heated at a rate of 50°C per minute to the test temperature and equilibrated at the test temperature for 10 minutes prior to testing.

7.5 SILICON NITRIDE SPIN TEST

Shaft to disk joins (Figure 8) were ground to yield the four-bladed spin test specimens (Figure 9). Five additional joins of the shaft-to

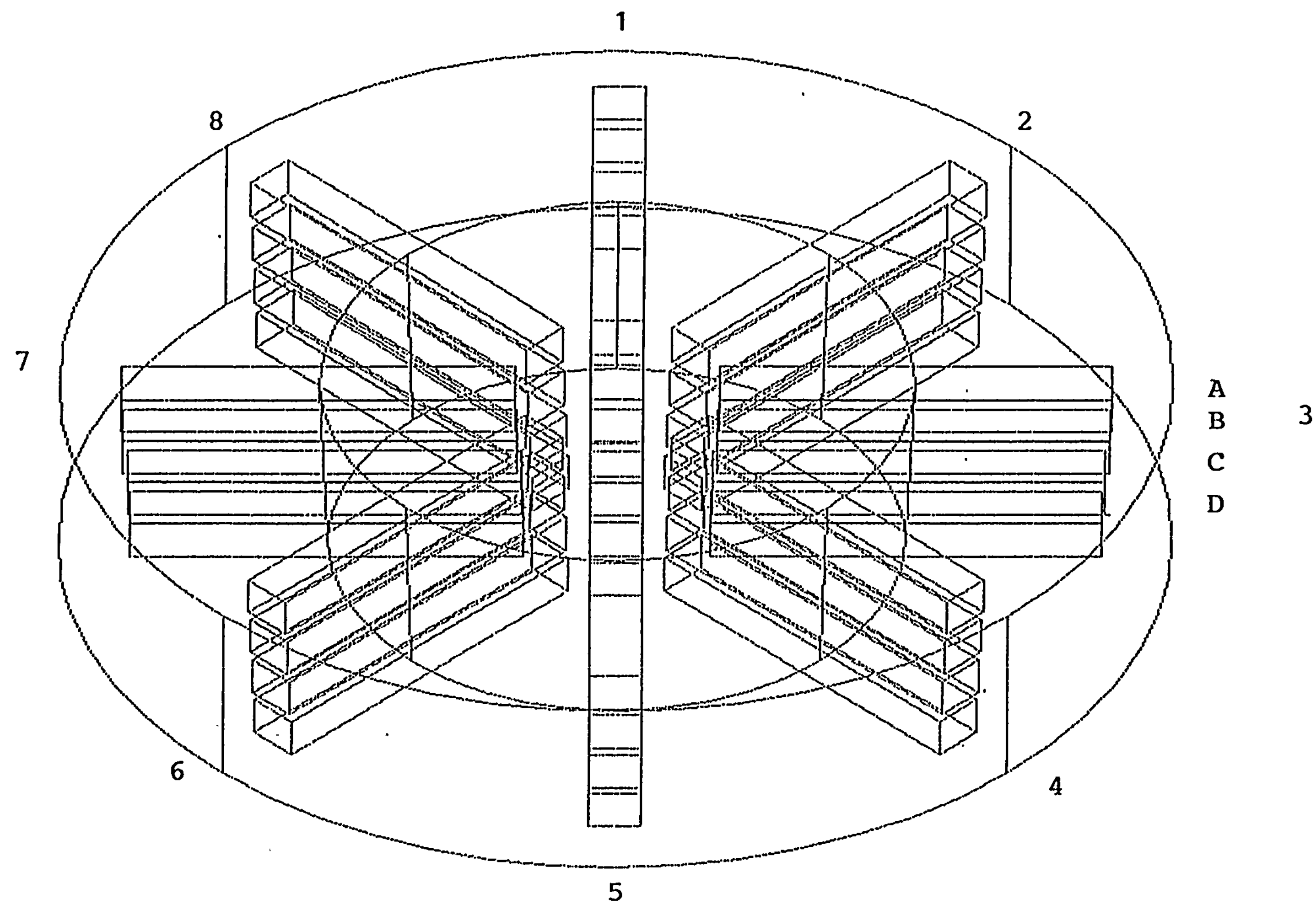

Figure 7: Configuration of Join Sectioning for Flexure Test Specimen Preparation (Task 1.2 - Final Iteration)

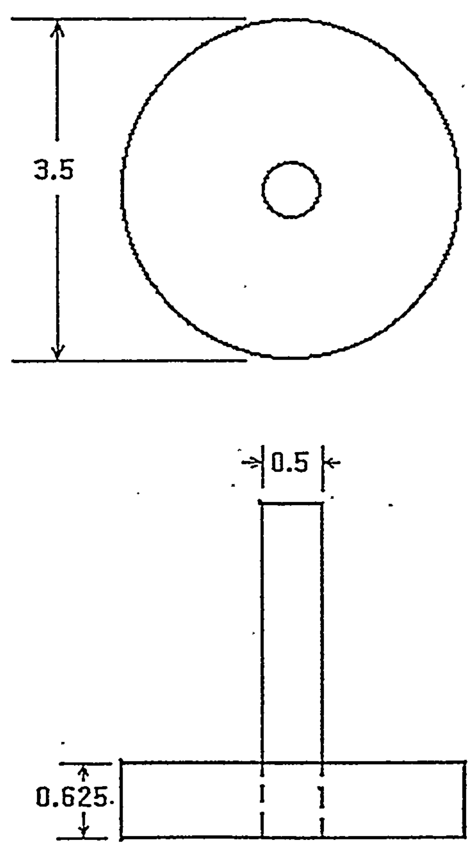

Figure 8: Spin Test Specimen Blanks (Dimensions in Inches)

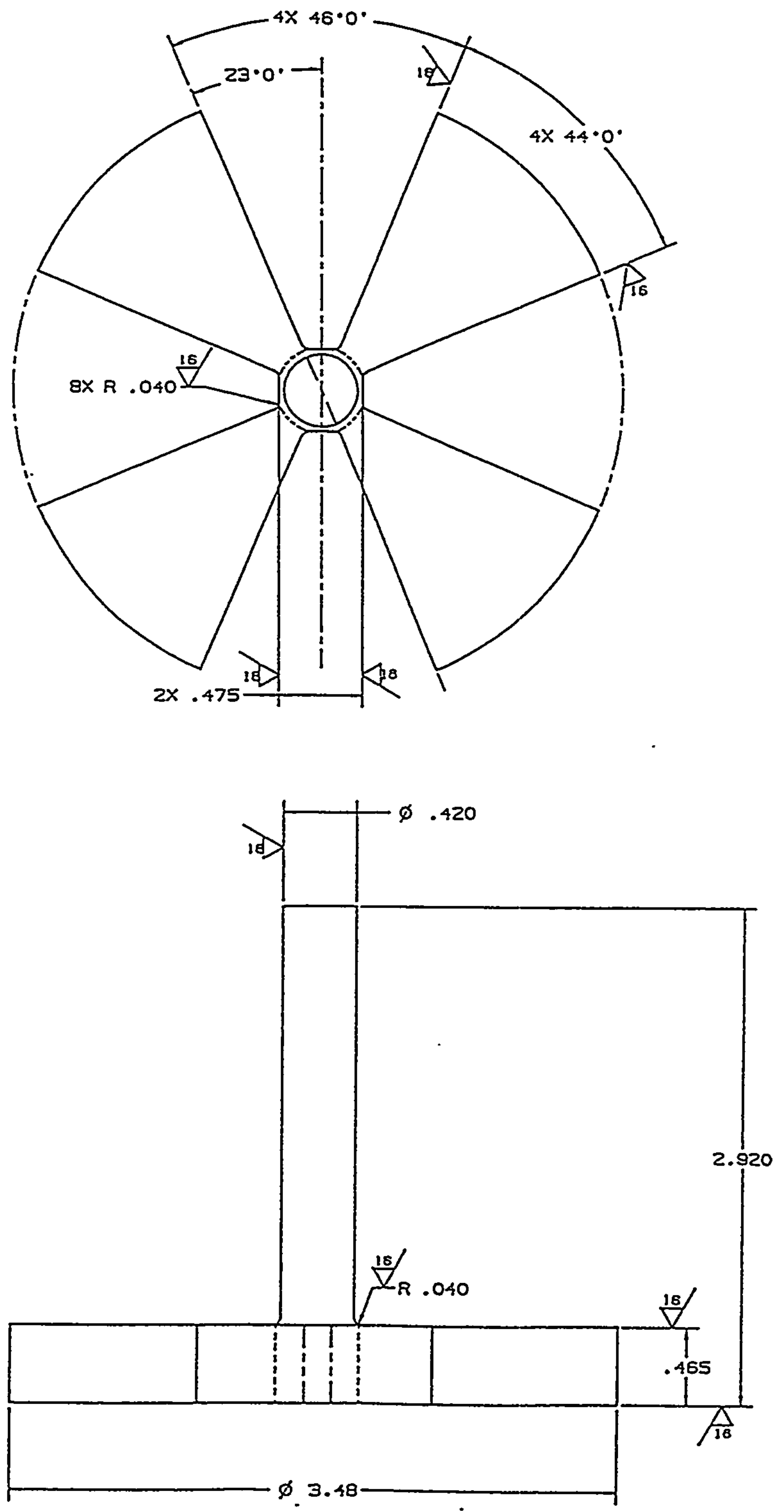

Figure 9: Spin Test Specimen Design (Dimensions in Inches)

-disk configuration were used to manufacture tensile specimens to determine tensile strength of the actual spin test specimen join geometry.

The spin specimens were tested by The Balancing Company, Vandalia, Ohio. Specimens were balanced and slowly accelerated at a rate of approximately 8.0 revolutions/sec^2, to limit rotational acceleration stress effects, until a failure occurred. Failures were recorded by high speed photography (Figure 10).

7.6 TENSILE FAST FRACTURE

Tensile specimens ground from shaft-to-disk joins contained two join interlayers within the gauge length and these were oriented perpendicular to the gauge length. The fast fracture tensile specimens had flat grip heads and 0.1" diameter by 1.0" in length cylindrical gauge sections (Figure 11). These specimens were tested at room temperature on an Instron Model 8562 utilizing the Instron "supergrips". In the load train the tensile specimen was attached to two stainless steel rods which were connected to the "supergrips". The specimen was attached to the rods in a pin and clevis arrangement using stainless steel dowel pins. The specimens were loaded to failure using a displacement rate of 0.100 inches per minute.

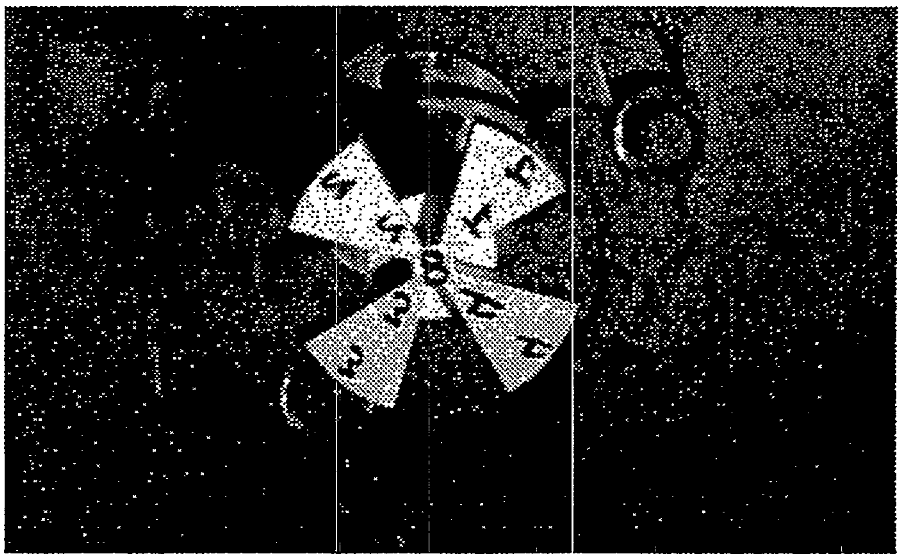

A) Prior To Failure

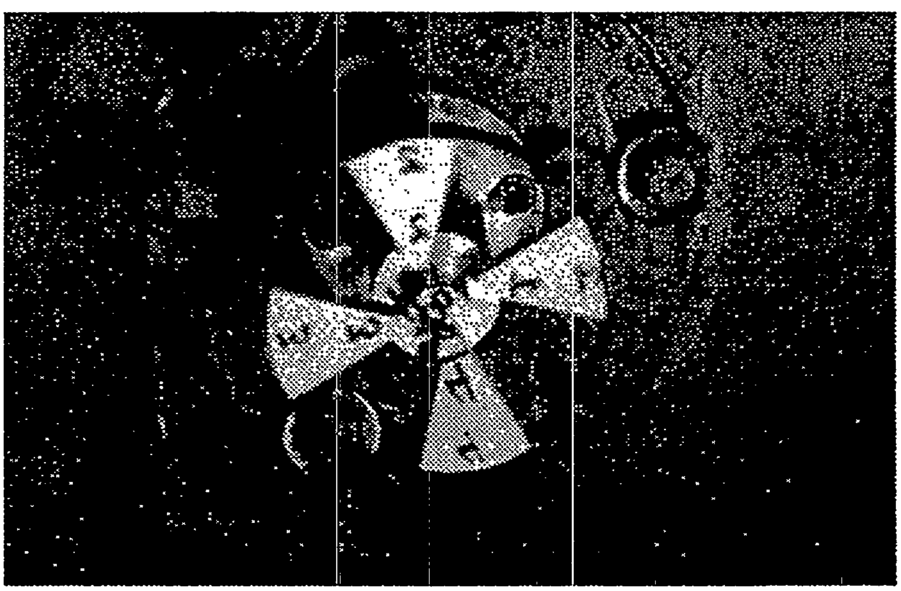

B) Immediately After Failure

Figure 10: High Speed Photography of Spin Test

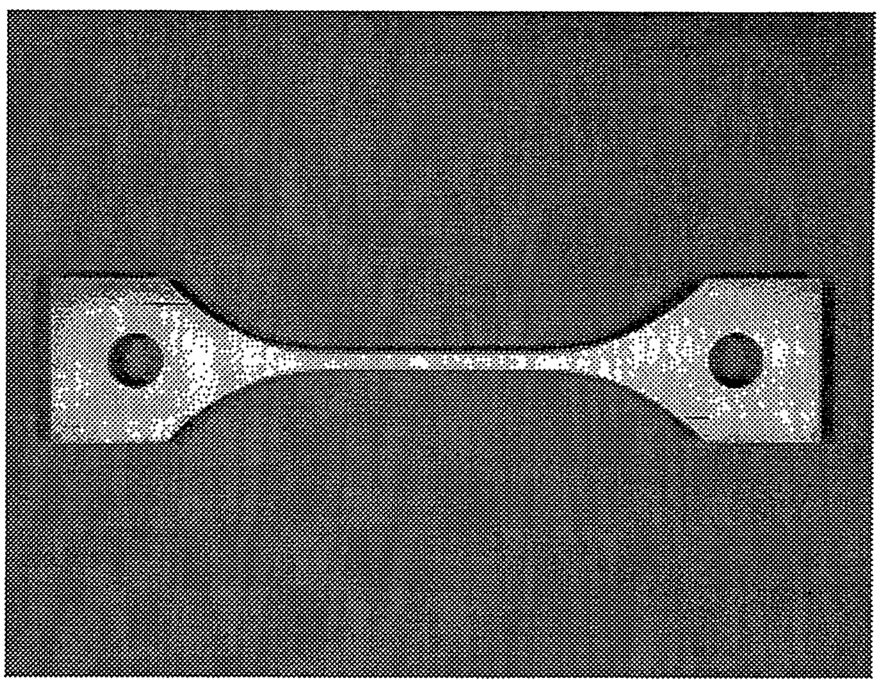

Figure 11: Cylindrical Gauge Tensile Fast Fracture Specimen

8 JOIN DEVELOPMENT

8.1 SILICON NITRIDE CURVED JOIN DEVELOPMENT (TASK 1.2)

Silicon nitride joins with excellent room temperature and high temperature (1370°C) mechanical properties were developed during Joining, Phase I using an, albeit simple, planar butt join geometry. Certain heat engine components could benefit from development of curved join geometries with mechanical performance similar to the planar butt joins. Consequently, considerable effort during Joining, Phase II was spent on development and testing of silicon nitride curved joins.

NCX-5101 Si_3N_4 was formed by cold isostatic pressing, green machined into curved shapes, joined in the green state and HIP densified to theoretical density. Join interlayers were either of various types of aqueous dispersions (or slips) made with NCX-5101 powder, or without slip. The aqueous slips although applied similarly, differ in method of preparation, additive content and the manner in which silicon nitride green joins were pre-conditioned. The resultant aggregate curved silicon nitride join after HIP densification was comprised of two joined sub-components: a disk of 83.8 mm outside diameter and 41.9 mm inside diameter into which a solid cylindrical disk was bonded. The join plane, within the resultant aggregate body, was formed at the contact of the two disks at a diameter of 41 mm (Figure 12).

8.1.1 Initial Join Development Trial

Initial curved joining trials were conducted on a small-scale with three types of join interlayers: no slip and two different aqueous slips, designated A and B. The Slip A and method of application was formerly used for the mechanical characterization and analytical modeling[1] tasks in Joining, Phase I and also Task 1.1 of Joining, Phase II. The aggregate join were determined to be theoretically dense after HIPing. ASTM C373-88 Microfocus x-radiography of each join showed complete densification of the join interlayer, with the exception of two areas of 1 mm x 0.5 mm dimension on the Type A join at the external surface. All joins were diamond sectioned after x-ray microfocus radiography for optical inspection to determine join integrity (Figures 13 and 14). The sectioned Slip A join and no slip join both exhibit incomplete closure of the join interlayer at the external surface of the joins (Figures 15 and 16). Sectioned surfaces of the Type B join appeared entirely dense. The Slip B join could be observed as a dark line in Figure 17 while the dense regions of the Slip A and no slip joins were not optically detected.

Mechanical Evaluation

Improved green strength was desired for silicon nitride joins to minimize handling rejections experienced prior to hot isostatic pressing during Joining, Phase I. Green shear strength tests were performed according to procedure of Section 7.2. The Type B slip join interlayer provided a significant improvement in green shear strength over no slip and Type A join interlayer (Table 1). The Type A joins and the no slip joins failed at the join interlayer. Type B joins after failure exhibited separation at the join interlayer in addition to fracture of the external and internal join disk. The origin of fracture for the Type B joins was uncertain. However, it is known that the B joins had markedly improved shear strength over the other treatments. Analysis of

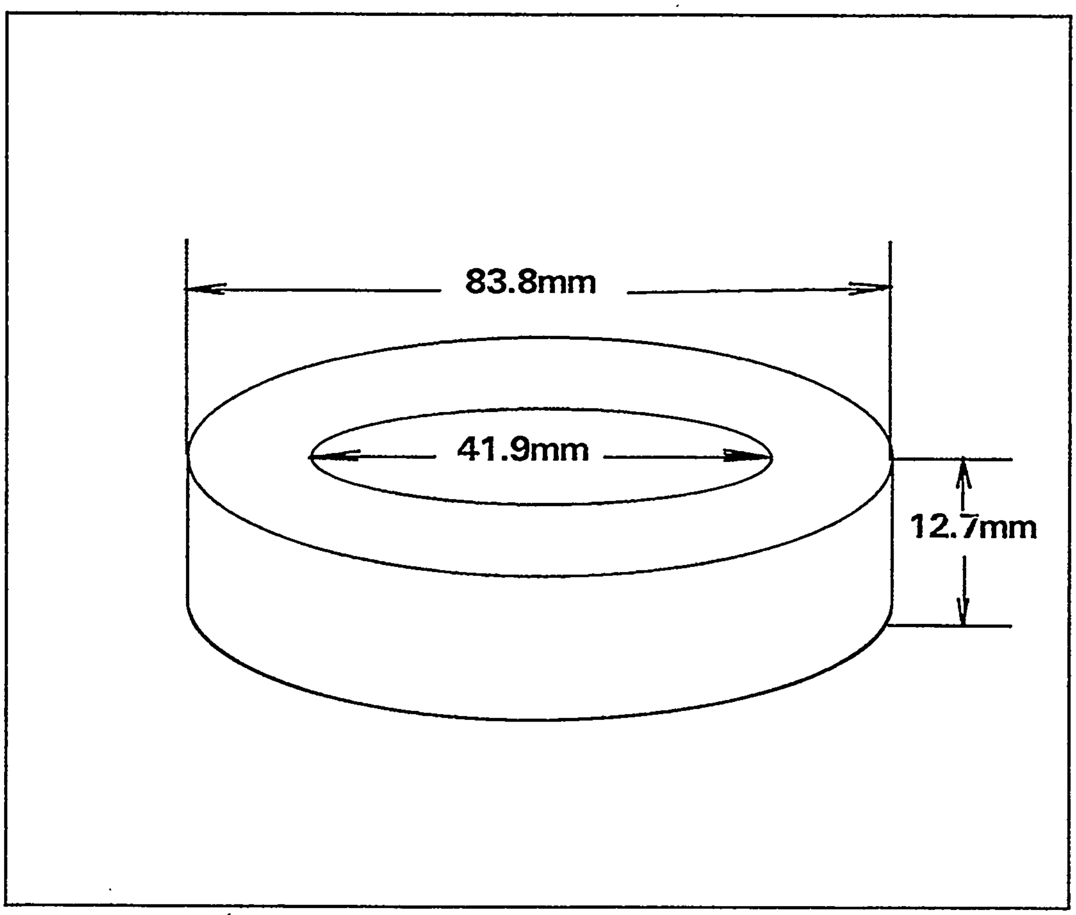

Figure 12: Curved Join Configuration

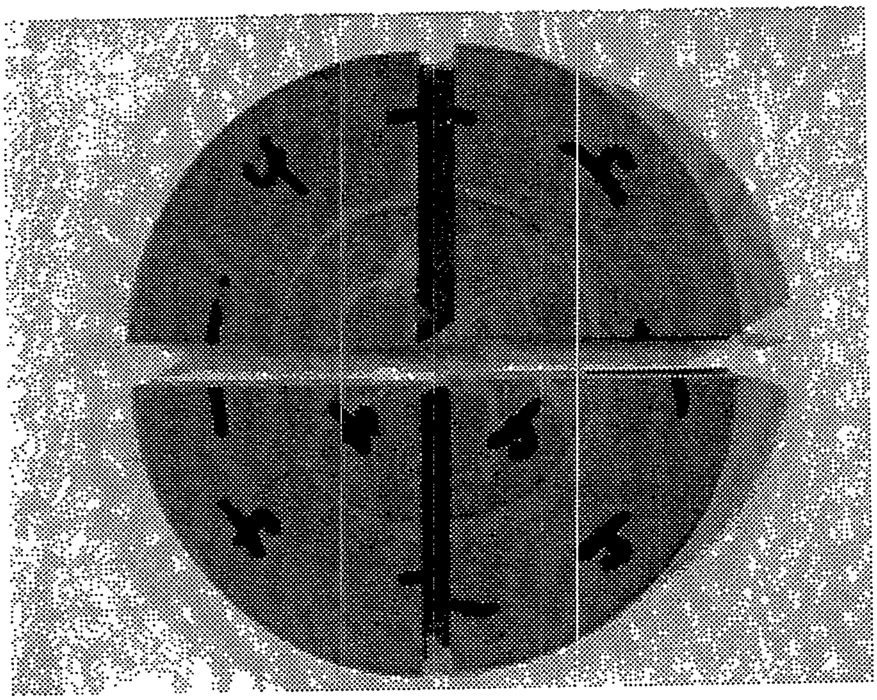

Figure 13: Sectioned NCX-5101 Silicon Nitride Curved Join

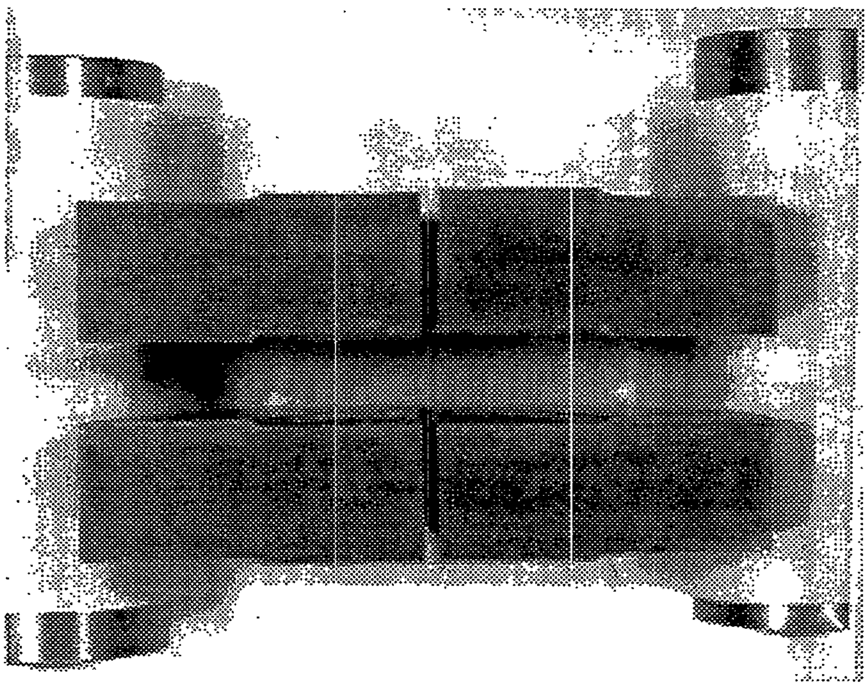

Figure 14: Cross-Section of NCX-5101 Silicon Nitride Curved Join

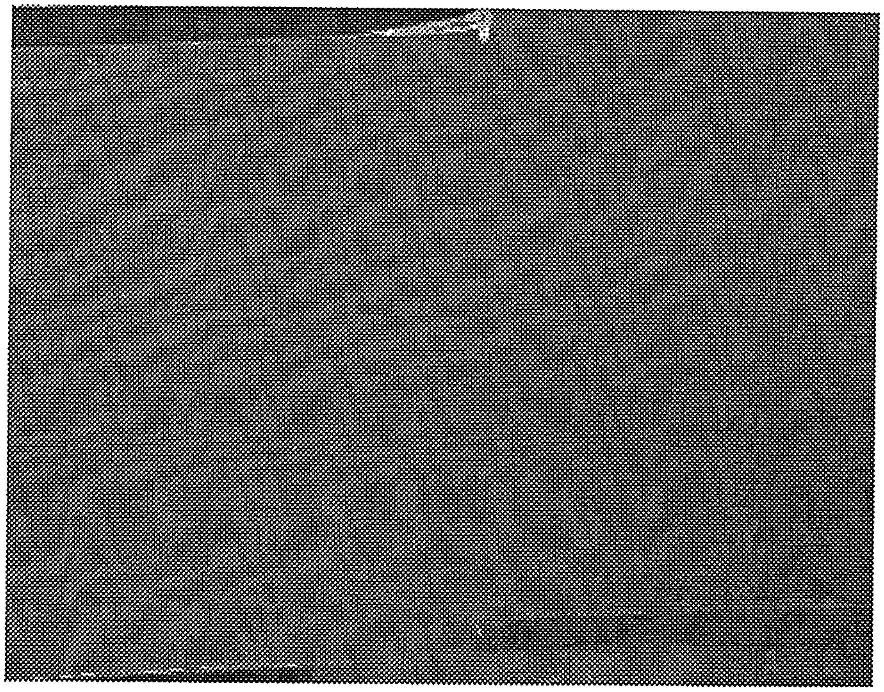

Figure 15: NCX-5101 Silicon Nitride Curved Join Cross Section With Type "A"Slip Interlayer

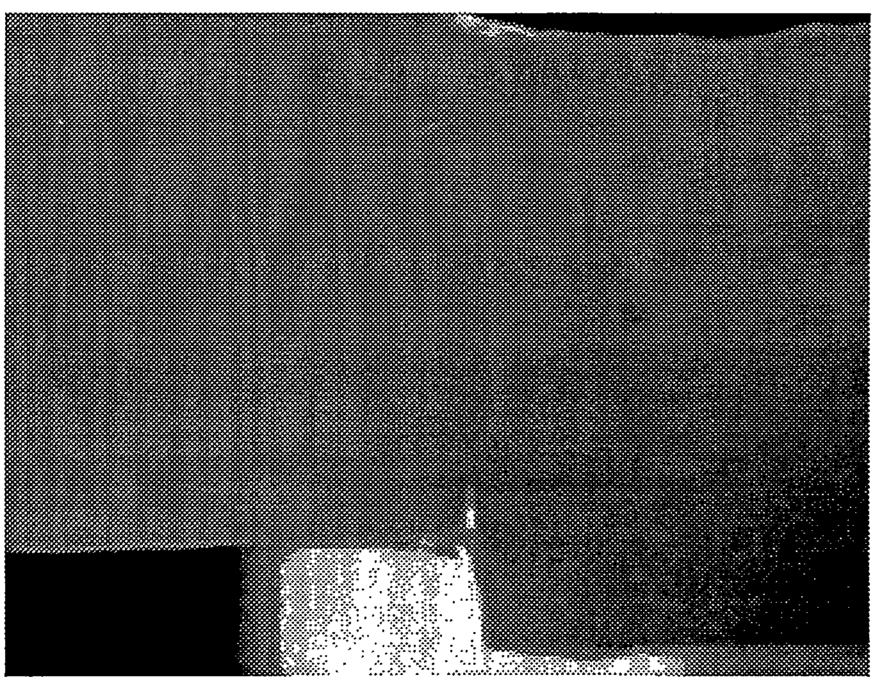

Figure 16: NCX-5101 Silicon Nitride Curved Join Cross Section With No Slip Interlayer

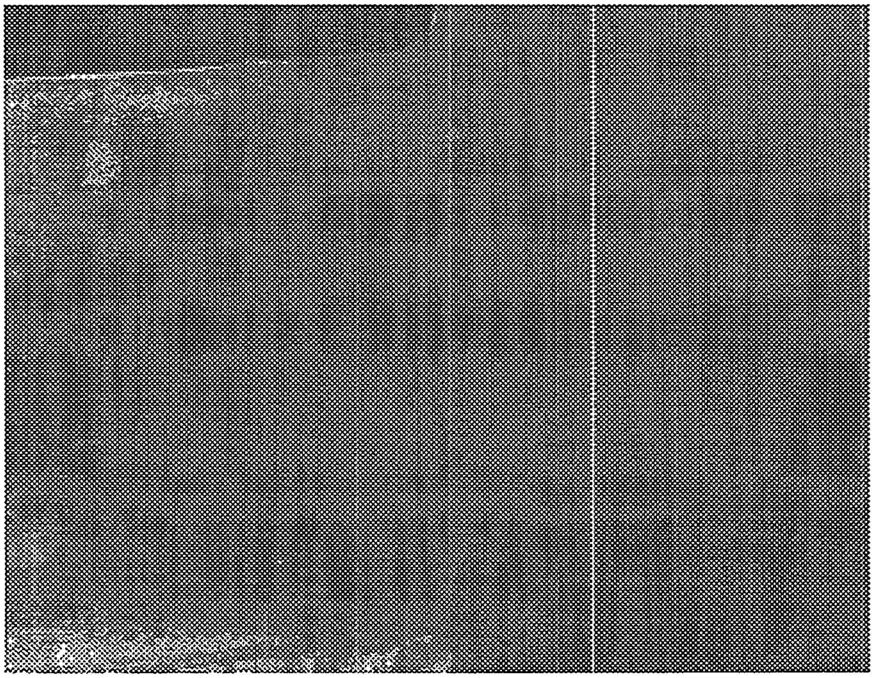

Figure 17: NCX-5101 Silicon Nitride Curved Join Cross Section With Type "B"Slip Interlayer

post shear tested Type A join interlayers exhibited a powdery slip residue that was easily removed. Slip residue of Type B join interlayers was firmly bonded to the parent materials.

Table 1: Silicon Nitride Curved Join - Green Shear Strength at 22°C

Slip Type	Join I.D.	Mean Green Shear Strength (kPa)	Standard Deviation (MPa)	Quantity Tested
No Slip	8, 9	589.8	121.8	2
A	5, 6	330.9	81.3	2
B	2, 3	1831.3	515.9	2

The results of 22°C and 1370°C flexure strength tests of specimens ground from the curved silicon nitride joins are summarized in Tables 2 and 3. The first attempts with joining of silicon nitride curved joins were promising although the small number of flexure tests of each join type made the analysis preliminary.

Table 2: Silicon Nitride Curved Join - Flexure Strength at 22°C

Slip Type	Join I.D.	Mean Flexure Strength (MPa)	Standard Deviation (MPa)	Quantity Tested	Join Interlayer Failures
B	1	771	108	6	0
A	4	832	130	5	1
No Slip	7	722	132	7	3

Table 3: Silicon Nitride Curved Join - Flexure Strength at 1370°C

Slip Type	Join I.D.	Mean Flexure Strength (MPa)	Standard Deviation (MPa)	Quantity Tested	Join Interlayer Failures
B	1	626	28	5	1
A	4	623	28	6	0
No Slip	7	582	30	4	1

There appeared to be an insignificant statistical difference between the 22°C and 1370°C flexure strengths of each type of joining method. However, the joins manufactured without slip exhibited the lowest mean flexure strength and the highest frequency of failures within the join interlayer at 22°C and 1370°C. Join interlayers without slip were not pursued further. Additional join manufacture and testing of slip join interlayers was undertaken to obtain a conclusive analysis.

8.1.2 Second Curved Join Development Trial

Encouraging results of the screening trial prompted a more rigorous application of the slip interlayer joining method using two of the slips from the screening trial (A and B) and the inclusion of two more, designated C and D. Two curved joins were made for each of four different types of slip interlayer to yield a total of 8 joins. Ground join sections indicate that incomplete closure of the near external surface of the join interlayer (~1 mm depth) was not controlled by application of a varying amounts of slip to the external join seam. No apparent trend of incomplete closure of the near external surface of the joins with the type of slip interlayer was noted as with earlier work.[6] More work was required to address this limitation of the joining method.

All joins were HIP'ed to theoretical density and provided sufficient flexure strength data to statistically evaluate the mechanical properties of joins made with Types A, B and variations of these slip interlayers. Flexure strength tests of specimens machined from the dense joins were performed at 22°C and 1370°C.

Mechanical Evaluation

22°C Flexure Strength

Mechanical evaluation of the final iteration of silicon nitride curved join development is summarized in Table 4. While certain disk joins have visible join lines the failures do not often originate at the join. Joins 11 and 13 had the highest frequency of join failures with incomplete join interlayer closure during hot isostatic pressing as the primary cause. A statistical comparison of data sets using a non-parametric robust analysis[5] found no difference between most of the flexure strengths at the 95% confidence level. Joins 15 and 16, made with Slip D, showed a significantly greater room temperature strength and Weibull modulus relative to the other join types, complete join closure and an absence of failures originating in the join interlayer. The Type D slip was chosen for the remainder of silicon nitride joining on this contract.

1370°C Flexure Strength

Results from 1370°C temperature fast fracture of MIL STD 1942A, Specimen A type bars for the second iteration of curved join development are shown in Table 5. There were no statistically significant differences of 1370°C strength as a function of slip type. The joins made with Types B and D slips demonstrated an absence of failure initiation within the join interlayer at 1370°C and gave the best high temperature strength. The high temperature performance and the room temperature properties for Type D joins supported selection of Type D joins for the remainder of the contract.

Table 4: Silicon Nitride Curved Join Development - Flexure Strength at 22°C

Disk Number	Interlayer Slip	Specimens Tested	Mean Strength (Mpa)	Std. Dev. (Mpa)	Min. Strength (Mpa)	Join Failures	Join Non Closure	Weibull Modulus
10	A	11	765	103	593	1	0	9.5
11	A	11	572	228	193	4	3	2.9
12	C	11	738	159	276	0	0	6.7
13	C	11	745	214	262	4	2	5
15	D	11	855	76	676	0	0	14.9
16	D	11	793	55	710	0	0	14.2
17	B	11	793	62	717	0	0	11.7
18	B	11	765	110	448	1	0	12.1

Table 5: Silicon Nitride Curved Join Development - Flexure Strength at 1370°C

Disk Number	Interlayer Slip	Specimens Tested	Mean Strength (Mpa)	Std. Dev. (Mpa)	Min Strength (Mpa)	Join Failures	Weibull Modulus
10	A	7	530	40	462	0	14.6
11	A	7	455	110	186	2	6.4
12	C	7	524	41	455	1	17.5
13	C	7	448	131	131	1	5
15	D	7	524	48	462	0	12.1
16	D	7	538	35	469	0	16.1
17	B	7	538	41	462	0	13.2
18	B	7	531	28	503	0	19.8

8.2 FINAL SILICON NITRIDE CURVED JOIN MECHANICAL CHARACTERIZATION (TASK 1.2)

8.2.1 Room Temperature Fast Fracture

Results of flexure tests on a 5 mm x 20 mm span are summarized in Table 6. Data was labelled by the curved join disk number and the layer (A, B, C or D) within the disk from which specimens originated (Figure 7). A statistical comparison of the outer layers (A, D) to the inner layers (B, C) using a robust non-parametric paired analysis found no difference at the 95% confidence interval within each joined disk. A similar analysis was run for all layers of a disk with each of the other disks. The results indicated a lower strength in joins 20 and 24. The cause of the lower strength of join 24 was not apparent, although, it may be related to a slightly lower density relative to other joins. Optical fractography showed failure origins to be located primarily at the surface and in most cases near a chamfer. The Weibull modulus for all outer layers (A, D) and all inner layers (B, C) were essentially identical at 16.4 and 16.5 respectively (Figure 18). The Weibull modulus for the combined groups was 16.4. The combined average strength was 886.3 +/- 56 MPa.

Table 6: Silicon Nitride Curved Join Development - 22°C Flexure Strength

Room Temperature Fast Fracture Data (Task 1.2)							
Disk Number	Slice	Specimens Tested	Mean Strength (Mpa)	Std. Dev. (Mpa)	Join Failures	Join Non Closure	Density gms/cc
19	A-D	16	925.3	38.6	0	0	3.229
19	B-C	16	914.3	75.2	0	0	
20	A-D	16	840.5	55.2	2	0	3.208
20	B-C	16	843.2	42.1	0	0	
21	A-D	16	906.1	69	0	0	3.229
21	B-C	15	926	60.7	0	0	
23	A-D	14	885.3	61.4	0	0	3.226
23	B-C	16	885.3	51.7	0	0	
24	A-D	15	867.4	49	0	0	3.229
24	B-C	16	869.4	64.1	0	0	

8.2.2 1370°C Fast Fracture

There were no significant differences between join strength at 1370°C as a function of position within the join (Table 7). The average strength for all specimens tested was 516 MPa +/- 47 MPa. The Weibull modulus was 16.0 (Figure 19).

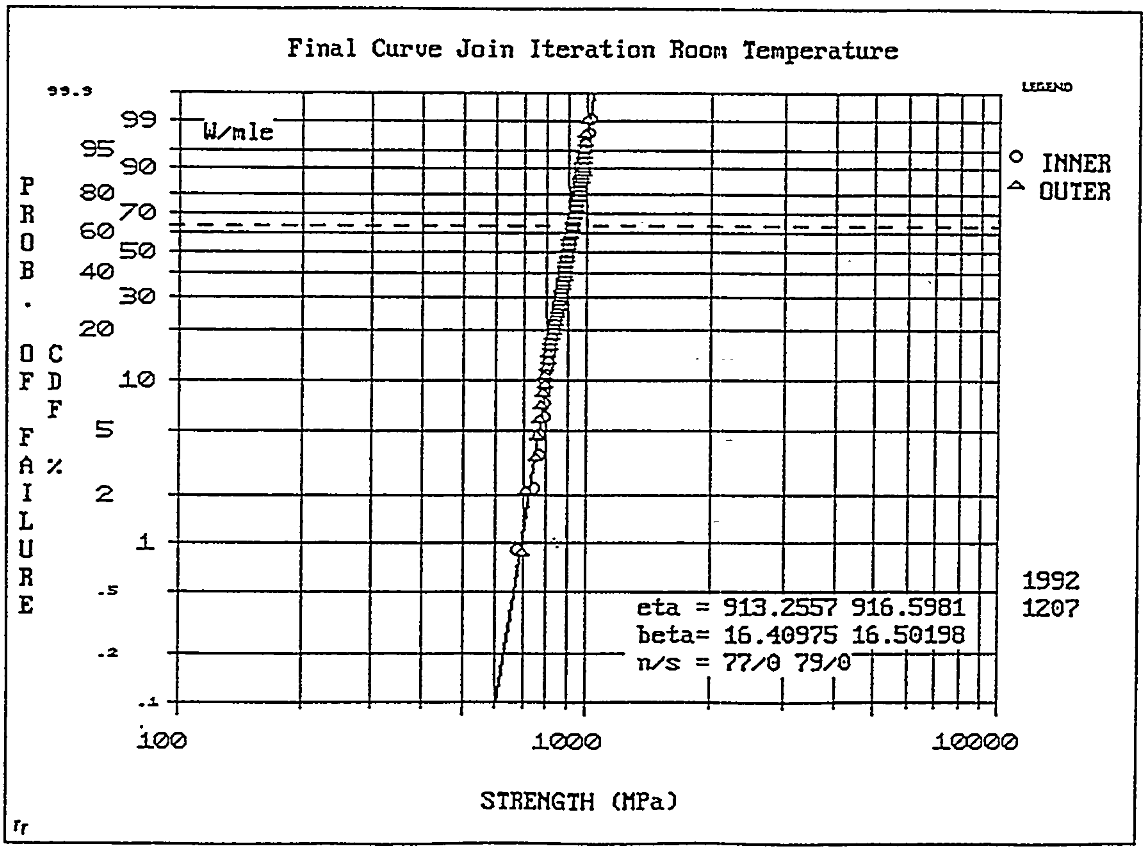

Figure 18: Weibull Probability Plot for Room Temperature Flexure Strength Evaluation

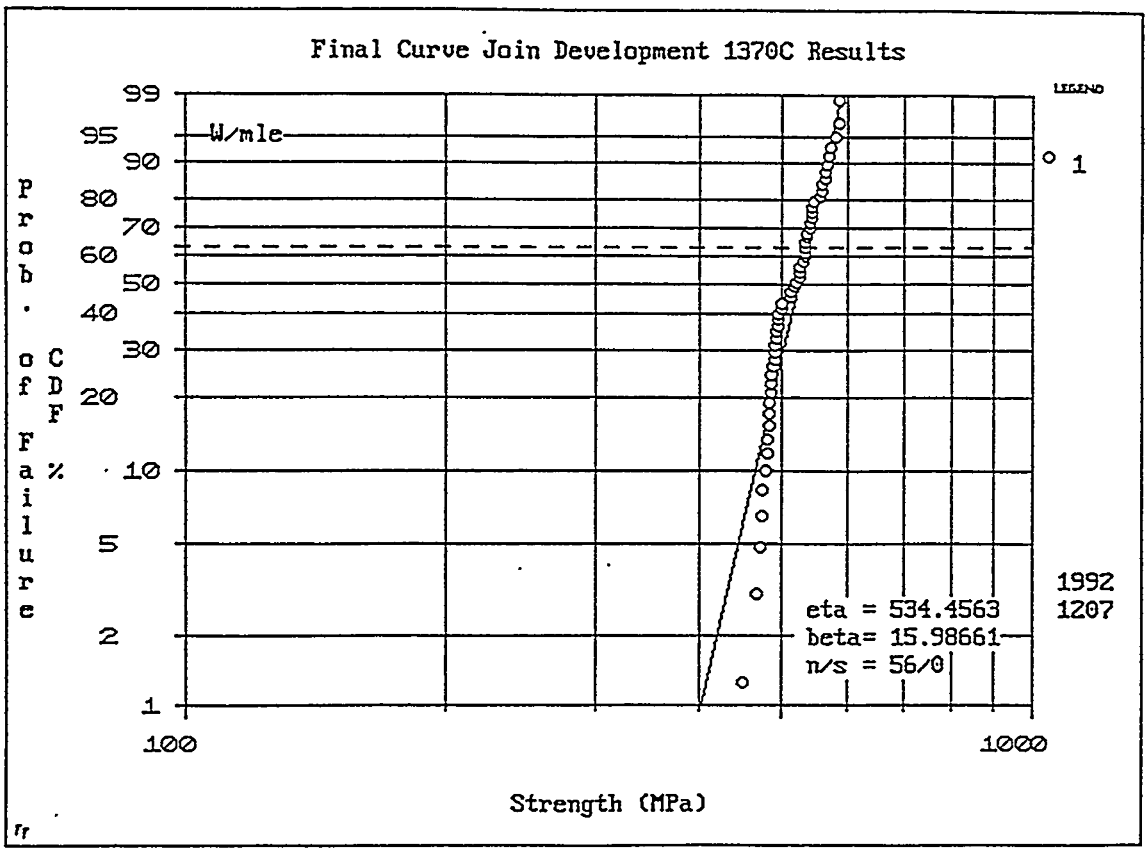

Figure 19: Weibull Probability Plot for 1370° Flexure Strength Evaluation

Table 7: Silicon Nitride Curved Join Development - 1370°C Flexure Strength

1370 Celsius Fast Fracture Data (Task 1.2)							
Disk Number	Interlayer	Specimens Tested	Mean Strength (Mpa)	Std. Dev. (Mpa)	Join Failures	Join Non-closure	Density gms/cc
26	A,D	14	506.8	35	1	0	3.228
26	B,C	16	490.2	74.5	2	1	
28	A,D	15	523.3	32.1	0	0	3.232
28	B,C	14	544	45.5	0	0	

8.2.3 Shear Testing

Two densified silicon nitride joined disks were sliced perpendicular to the axis to make three test specimens 2.50 mm thick by 70 mm diameter from each disk for a total of six specimens. Five specimens were shear tested at 25°C and one at 1370°C. The loading configuration is shown in Figure 6. Two different load/support ring diameter ratios were used. The results are summarized in Table 8.

Table 8: Silicon Nitride Shear Strength

Sample	Temp	R Loading Ring/ R Support	Load (kg)	Biaxial Flexural Stress (MPa)	Ave. Shear Stress (MPa)	Flaw Origin	Join Failure
1	Room	0.802	1684	407.0	55.0	Surface	No
2	Room	0.802	1838	447.4	60.1	Surface	No
3	Room	0.802	1830	444.8	59.8	Surface	No
4	1370C	0.918	3240	329.6	105.9	Unknown	Unknown
5	Room	0.918	2000	203.5	65.4	Surface	No
6	Room	0.918	1853	188.5	60.6	Surface	No

Besides the shear stress that develops in the annulus between load disk and support ring, an additional stress field of importance that develops in this test is the flexural field below the load disk. The average shear stress and maximum flexural stress are given by:

$$\tau=\frac{P}{2\pi ct} \tag{1}$$

$$\sigma=\frac{3P}{2\pi t^2}[(1-v)\frac{a^2-r^2}{2b^2}+(1+v)\ln\frac{a}{r}] \tag{2}$$

where
- a = support radius
- b = specimen radius
- r = loading ring radius
- c = join radius
- t = specimen thickness
- P = applied load

The flexural stress relationship was presented in reference 5.

Load/support ring ratios of 0.802 and 0.918 were used in the tests. These provide shear/flexure stress ratios of 0.14 and 0.32, respectively.

Failure origins in the fine room temperature tests were located on the bottom of the specimens, within the region of uniform biaxial flexure. None of these were associated with the join. Figure 20 shows the fracture pattern which developed in specimen 3. The failure origin for the 1370°C test was not discernable from the fragments of this specimen.

The flexural strength of the room temperature specimens ranged from 189 to 447 MPa. These specimen failed within the uniform flexure region and thus the 60 MPa level shear stress present in the specimens did not composite to these failures. The high temperature specimen failed at flexure and sheer stress levels of 330 and 106 MPa, respectively. The lack of information on the failure origin in this case prevents a determination of the role of the shear stress component in this failure.

8.3 SILICON NITRIDE SHAFT-TO-DISK JOIN (TASK 1.4)

The demonstration of curved join quality similar to planar butt joins developed during Phase I of this contract allowed application of the joining technique to more complex shapes, such as a simulated rotor geometry. Ten curved NCX-5101 joins of a shaft-to-disk configuration were fabricated (Figure 8). Five of the densified joins were machined into four-bladed spin test specimens (Figure 9). The remaining shaft-to-disk samples were used to manufacture tensile specimens to determine tensile strength of the actual spin test specimen join geometry.

8.3.1 Tensile Strength

The tensile specimens were pin-loaded with flat grip sections and cylindrical gauge section with a 0.1" diameter and 1.0" length (Figure 11). Two join interlayers oriented perpendicular to the gauge length were within the gauge of each tensile specimen. The tensile specimens are identified with two numbers: the first number denotes the shaft-to

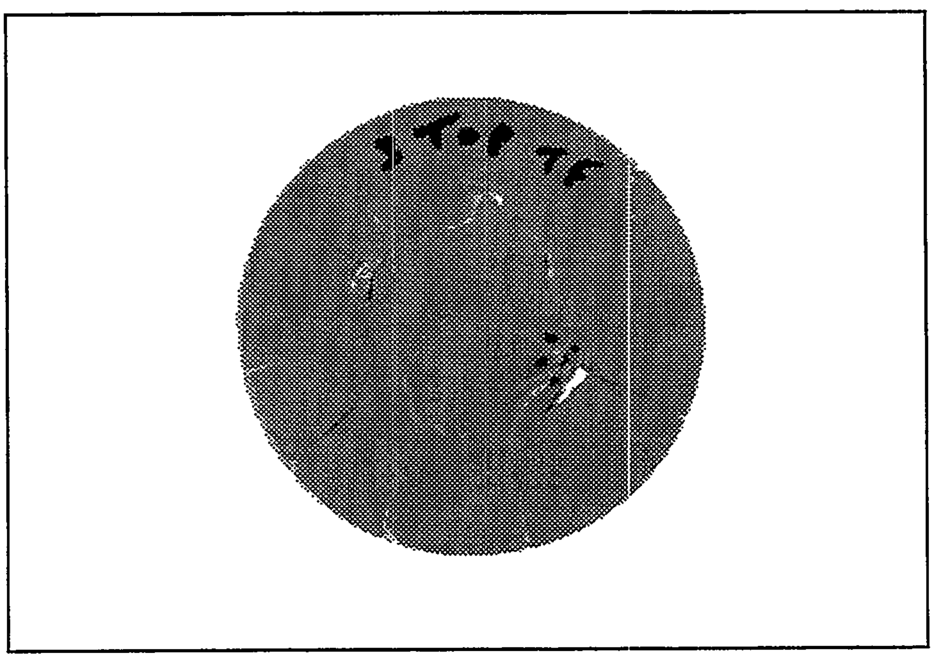

Figure 20: Failed Joined Disk

-disk join from which the specimen was machined and the second number differentiates between specimens from the same parent join (Table 9).

Table 9: Silicon Nitride Shaft-To-Disk Join - Round Gauge Tensile Strength

Room Temperature Fast Fracture Data		
Specimen #	**Failure Stress (MPa)**	**Failure Location**
9 #1	710.25	gauge, non-join
9 #2	660.50	gauge, non-join
10 #1	470.99	gauge, non-join
10 #2	491.06	clevis pin hole
13 #1	662.53	gauge, non-join
17 #1	491.14	gauge, non-join
17 #2	592.39	gauge, non-join
19 #1	359.76	clevis pin hole

Six of eight specimens tested failed from surface origins within the gauge section away from the join interfaces (Figure 21). The remaining two tensile specimens failed at the clevis-pin hole and were not considered in the strength distribution. The mean tensile strength of the six valid tests was 598 MPa. Weibull analysis of this limited data set suggests a characteristic strength of 636 MPa and a Weibull modulus (m) of 8.2 (Figure 22).

Fractography suggests that each of the five spin specimens failed from damage induced by machining in the regions of high curvature near the shaft, but away from the join. An example of surface damage is provided in the SEM micrograph in Figure 23. The failure speeds of the spin tests ranged from 17,000 to 42,530 rpm as is discussed below:

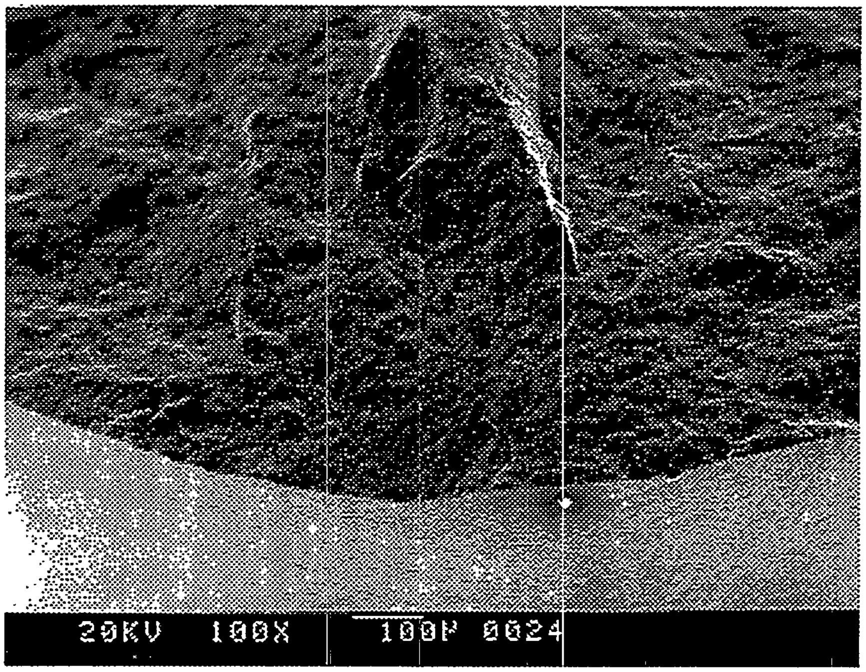

A) 100X

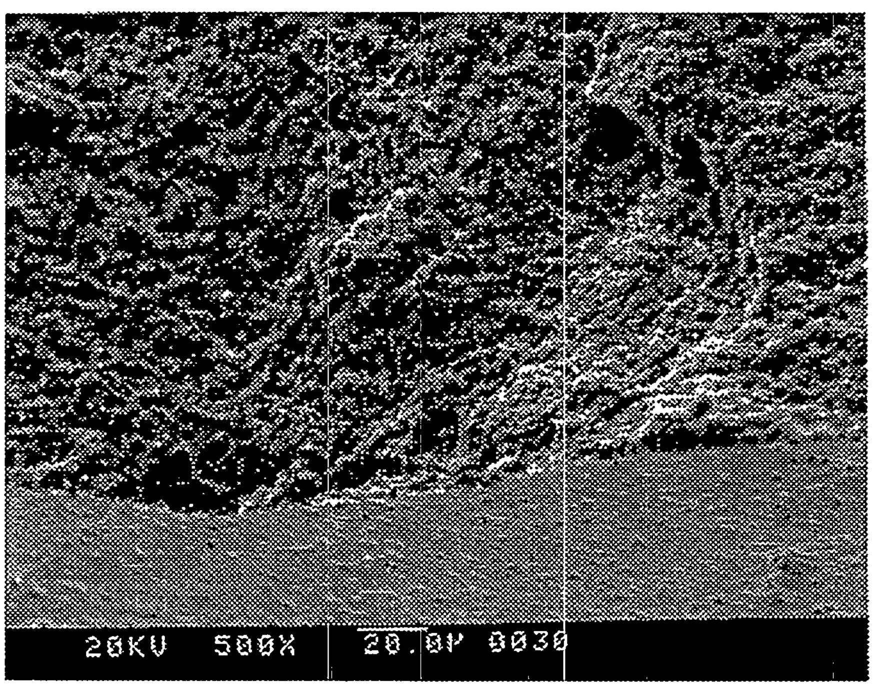

B) 500X

Figure 21: Failure Origin of a Silicon Nitride Round Gauge Tensile Specimen#17-1

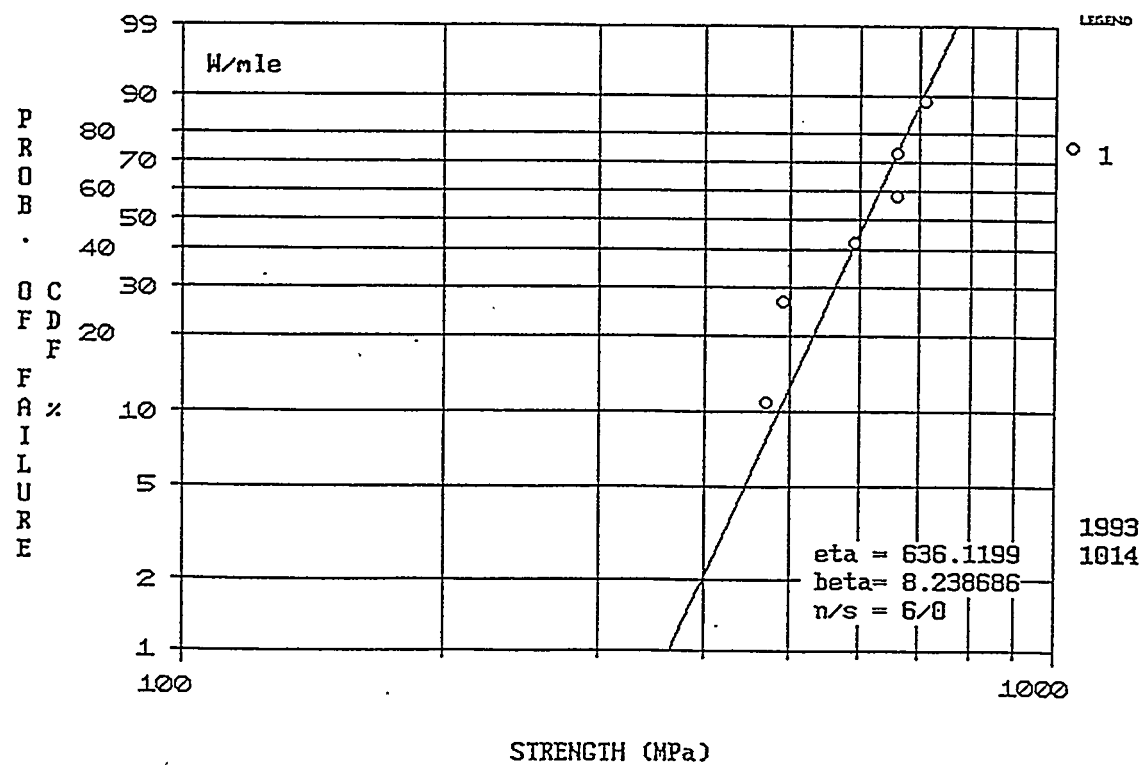

Figure 22: Weibull Probability Plot of the Round Gauge Tensile Specimens

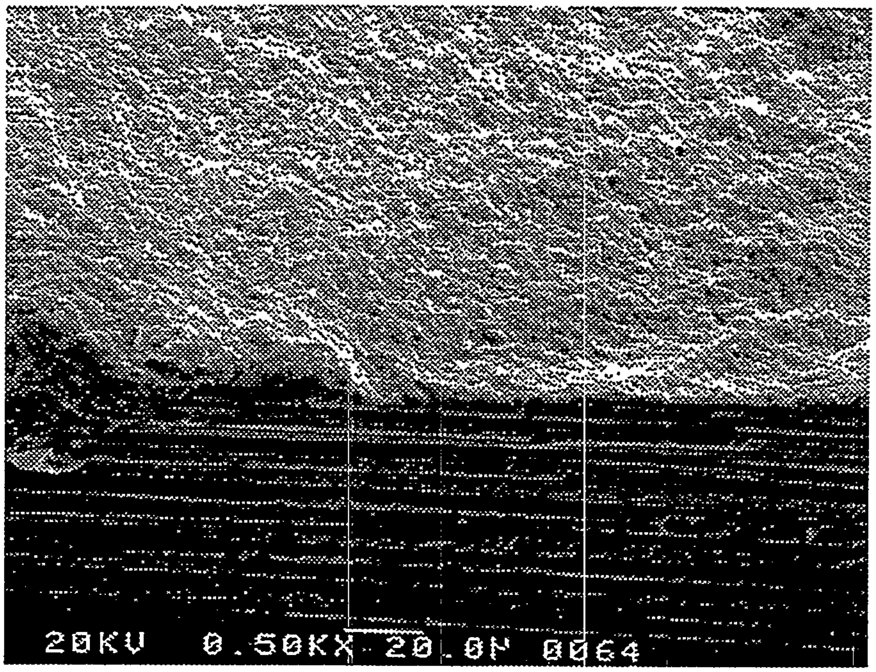

A) 500X

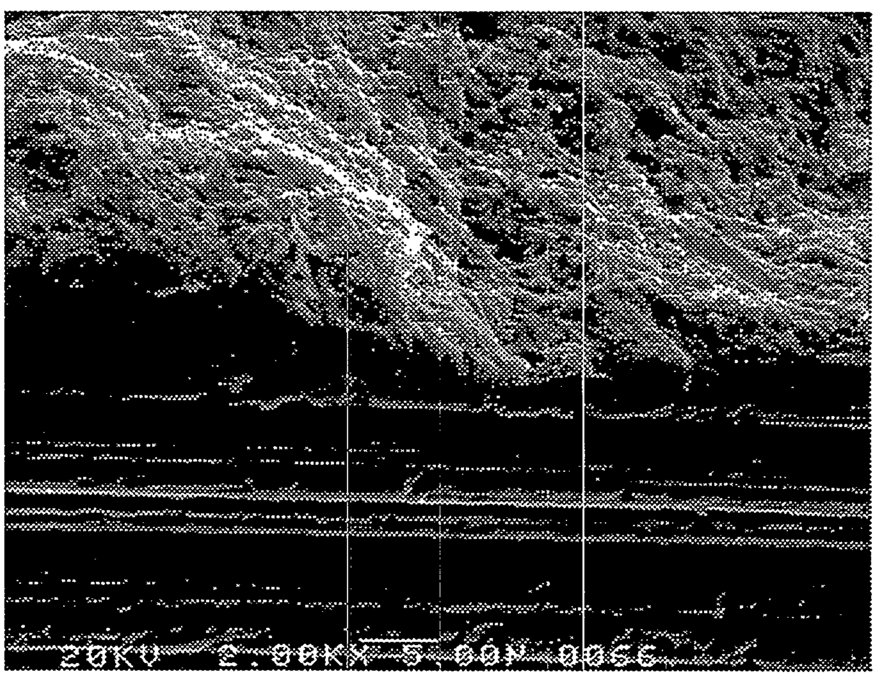

B) 2000X

Figure 23: Failure Origin of a Silicon Nitride Spin Test Specimen #11

8.3.2 Spin Test (Task 1.4B)

Table 10: Silicon Nitride Spin Test Results

Specimen Number	Ang. Velocity at Failure (rpm)	Max Stress at Failure (MPa)	Surface Defect Size, 2a (microns)	
			Fracture Mechanics (Equation 2)	Fractographic Measurement
3	17000	88.0	3941	-
18	32030	312.3	313	246 - 280
11	36820	412.7	179	176 - 210
14	37980	439.1	158	158 - 192
8	42530	550.6	101	88 - 122

8.3.3 Modeling

The spin test specimen was analyzed using a 3D finite element model in ANSYS[6]. Due to symmetry only one quarter of the specimen needed to be modeled. The model consists of 8368, eight node, brick elements concentrated at the root of the blade, as well as 2444, four node, surface elements (to capture surface stress levels), for a total of 10812 elements. The loading was specified to be a constant angular velocity applied to the entire model along the axis of the rod. Contour plots of the maximum principal stress (σ_1) for an angular velocity of 50,000 rpm are shown in Figure 24 overlaying the finite element grid. A principal stress value of 761 MPa develops through the thickness of the blade root a short distance (0.5 - 1.0 mm.) from the join. The join experiences stresses in the 350 to 400 MPa range at this velocity. These results may be scaled by the square of the angular velocity.

Failure origins of the spin specimens were traced to the model-predicted region of highest stress. Fractography showed that all of the test specimens failed due to surface flaws. Based on this, a reliability analysis assuming surface flaws as the critical flaw population was conducted using the CARES[7] reliability analysis post-processor. The Weibull parameters used in this analysis were from data on approximately 150 flexure bars which suggest a Weibull modulus (m) of 16.4 and characteristic strength of 913 MPa. The predicted probability of failure of the spin test specimen is plotted in Figure 25 as a function of angular velocity. Plotted as circles on the graph are the actual data points from our tests. The predicted failure loads overestimate the actuals by 3,000 to 24,000 rpm.

This discrepancy is likely attributable to the difference in the machined surface quality between the spin test specimens and the flexure bars. As a result, there were larger surface defects in the spin test specimens causing them to fail at a lower load. Similar results having overestimated reliability predictions have been reported[8] for spin failure tests of NT154 axisymmetric, monolithic spin specimens. The discrepancy between test data and predictions were attributed to the different machining procedures used for the specimens which provided the strength database and the spin specimens.

The surface defect size can be attained in two ways. The first way

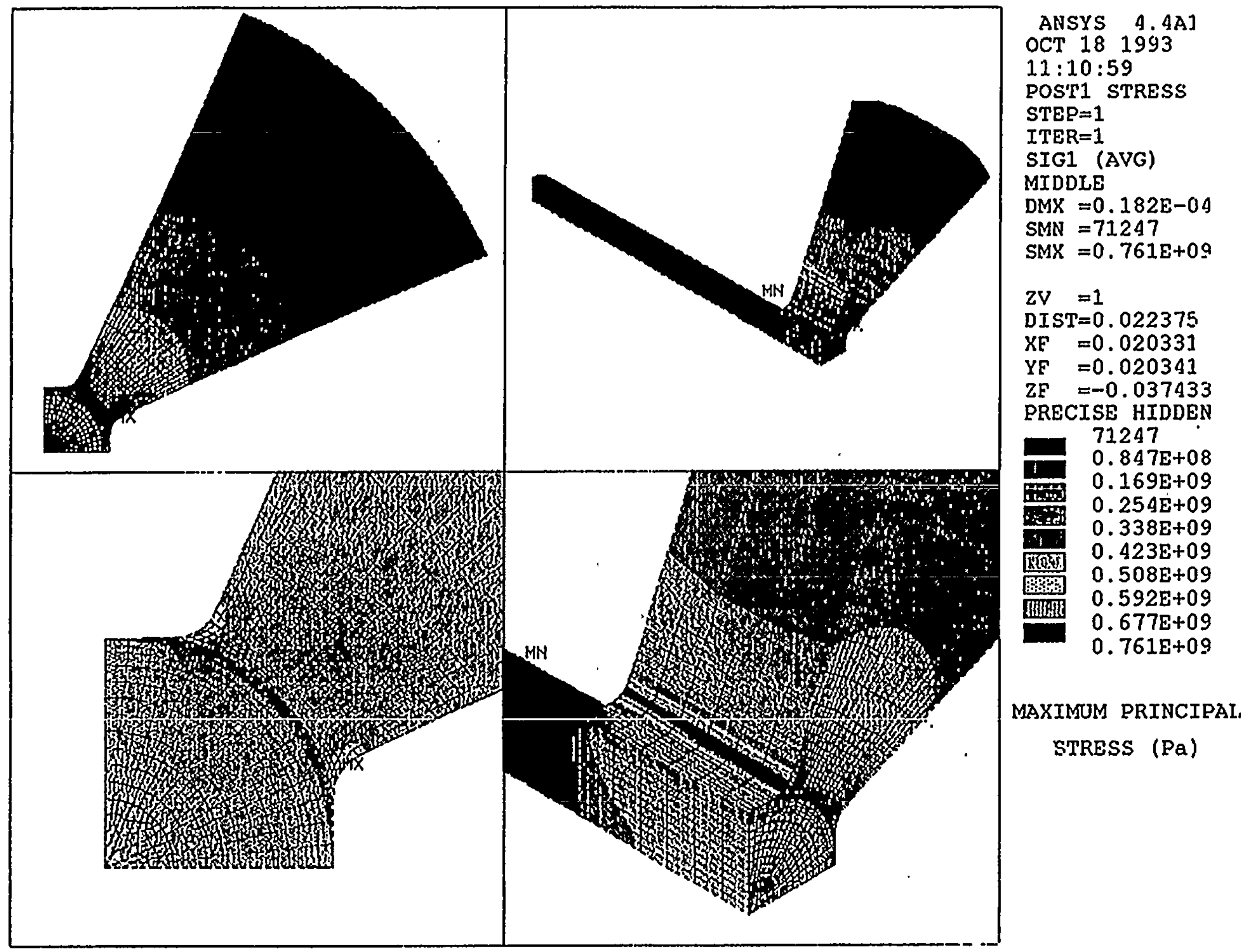

Figure 24: Maximum Principal Stress in the Spin Test Finite Element Model for an Angular Velocity of 50,000 rpm

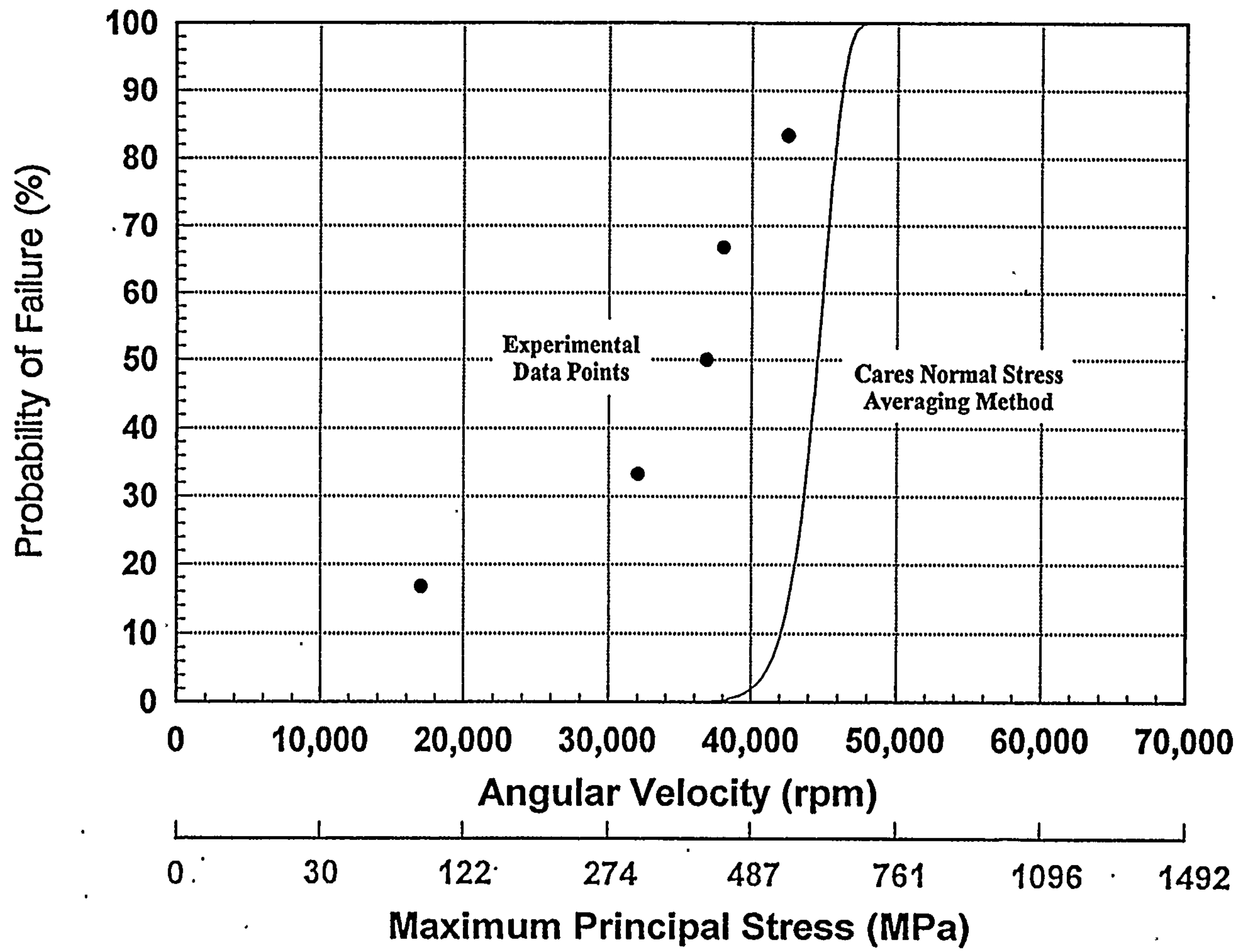

Figure 25: Probability of Failure for Joined Silicon Nitride Spin Test as a Function of Angular Velocity

was to measure the defect from fractographs. A second way was to determine the failure stress of the spin test specimens from the finite element model based on the angular velocity at failure. Using fracture mechanics, this stress can be used with the toughness of the material (K_{IC}=5.5 MPa·m$^{1/2}$) to determine the flaw size. If a semi-circular surface flaw of radius, a, is assumed, the fracture mechanics relationship[9] that can be solved for the size parameter a is:

$$\sigma_{failure}=0.71\frac{K_{IC}}{\sqrt{a}} \tag{3}$$

The surface length of the defect is 2a in this model.

Fractographs of four of the spin specimens are given in Figure 26 and 27. The arrows are pointing to the apparent mirror boundaries. The surface defect (2a) is also noted.

Table 10 compares the inferred fracture mechanics defect size to the measured fractographic defect measurements. Since there is an error associated with the measurement of a defect size, a range of values has been given for the fractographic measurement. The surface defect sizes (2a) calculated from Equation 3 fall either in the range or extremely close to the measured values, except for specimen 3 which failed at an extremely low load as compared with the other specimens. It is not known why it failed at such a low load. The surface defect size needed for failure at this load is in the 3-4 mm range which suggests a major defect was present in this specimen. The agreement for the other four specimens lends credence to the view that machining damage was the failure origin in these cases. The size of the defects (diameter, 2a = 101- 313 μm) exceed that expected from precision grinding, such as is routinely employed for MOR bars. Hence it is concluded that the lower than predicted failure velocities was attributed to the specific grinding procedure used to prepare the bladed spin specimen.

8.4 SILICON CARBIDE - PLANAR BUTT JOIN DEVELOPMENT (TASK 2.1A)

8.4.1 Initial Join Development Trial

Attempts were made to join parent materials of siliconized NT230 to siliconized NT230 and pre-sintered un-siliconized NT230 to pre-sintered un-siliconized NT230. The parent materials were billets of 38 x 51 x 51 mm dimensions with the join plane of 38 x 51 mm dimension. The faces to be joined were ground flat prior to joining. Join interlayers were applied as aqueous dispersions, or slips, of silicon carbide, and other additives, and used to join NT230 silicon carbide billets. Microfocus x-radiography was used to ensure only billets without gross structural defects were to be used for the contract. After joining with slip the aggregate bodies were pre-sintered and siliconized.

Initial screening tests used the same slip interlayer, designated A, for making one join from siliconized NT230 parent materials and one join of unsiliconized NT230 parent materials. There was a silicon enrichment at the join interface with both joining approaches that resulted in a join of much lower strength than the parent materials. Joins made from the initial unsiliconized materials exhibited a join interlayer with such pronounced silicon enrichment and strength degradation that the join interlayer was incapable of withstanding stress

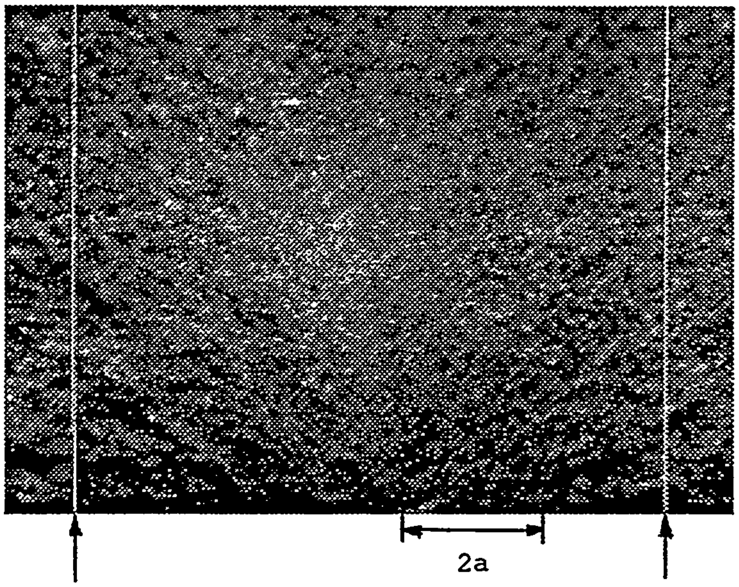

A) Specimen 18,
Blade 4

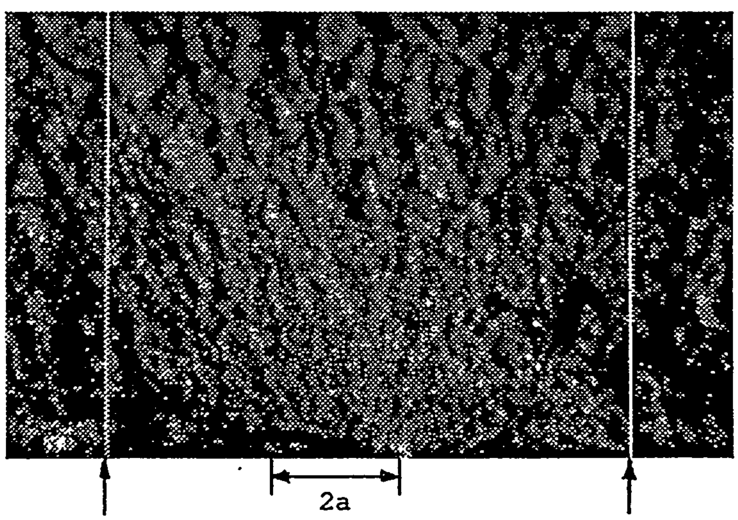

B) Specimen 11,
Blade 2

Figure 26: Fractographs of Silicon Nitride Spin Test Specimens

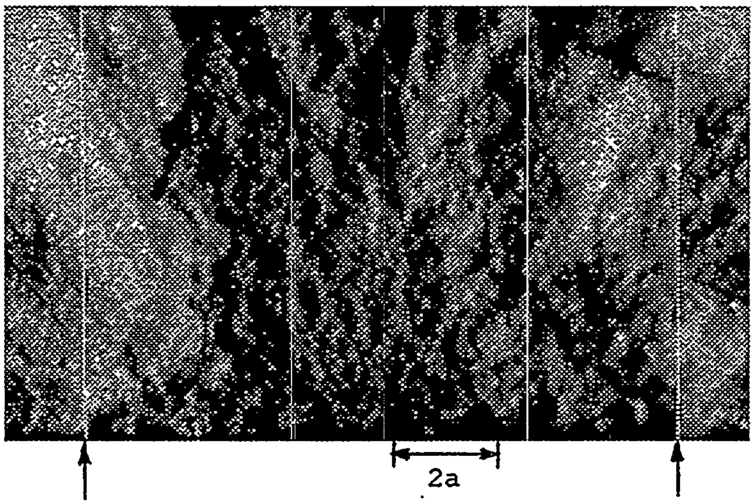

A) Specimen 14,
Blade 1

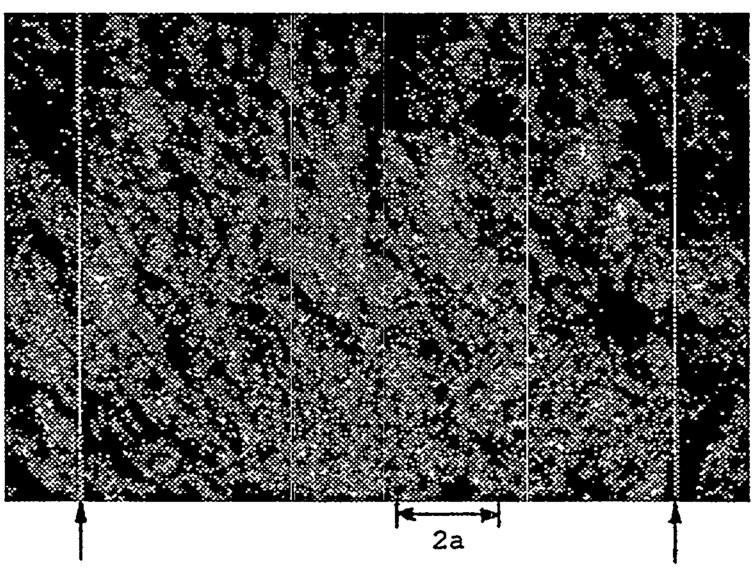

B) Specimen 8,
Blade 2

Figure 27: Fractographs of Silicon Nitride Spin Test Specimens

of grinding causing fracture of the join interlayer. Macrostructure of the join interlayer was comprised of silicon carbide honeycomb cells predominantly filled with silicon (Figure 28). Microstructure inside of cells incompletely filled with silicon exhibited a poorly bonded silicon carbide network at the join interlayer (Figure 29).

Mechanical Evaluation

Mean flexure strength of the joins was 222 MPa with a standard deviation of 41 MPa as compared to a mean flexure strength of the unjoined control body of 232.9 MPa. All failures originated within the join interlayer at sites of porosity and/or silicon enrichment (Figure 30). The strength of 232.9 MPa is low for a typical NT230 body and due to inherent thickness limitations of the siliconization process. Typical average flexure strength for NT230 is 410 MPa.

8.4.2 Final Join Development Trial

Additional silicon carbide joins were made to minimize the excessive silicon enrichment and porosity at the join interlayer. Six interlayer types, designated A through F, were used for joining both siliconized and unsiliconized parent materials. Interlayer A was a replication of the earlier work which resulted in silicon enrichment and porosity of the join interlayer. Interlayers B through F were new compositions. Attempts were made to sinter and siliconize twelve joins, six with siliconized parent materials and six with unsiliconized parent materials. One join made from the siliconized parent materials and five joins of the unsiliconized parent materials separated during presinter, siliconization or grinding of the mechanical test specimens. Flexure specimens were machined from the remainder of the joins to evaluate strength.

Mechanical Evaluation

Room temperature strengths of the joins were not improved with the different join interlayer treatments (Table 11). Failure originated predominantly within the join interlayer at regions of porosity and/or silicon enrichment. The mean join strengths ranged between 101 and 222 MPa as compared to 233 MPa for the mean strength of the unjoined NT230 silicon carbide parent material of similar cross sectional thickness. The NT230 parent material of 38 mm cross -sectional thickness demonstrated significantly lower strength than typical for NT230 of thinner cross-section (410 MPa for 10 mm thick cross-section). Characterization determined the cause of strength dependence upon cross-sectional thickness was due to inhomogeneous silicon infiltration across the join cross-section during the manufacture of the parent material.

Polished sections of the joined interlayers are exhibited in Figures 31 to 36. Joins are identified for ease of discussion by the type of parent material (siliconized=S or unsiliconized=U) and join interlayer (A through F). For example, a join S-D was made with the initially siliconized parent materials and joined with interlayer D. The appearance of the joins vary widely, with S-B exhibiting the most

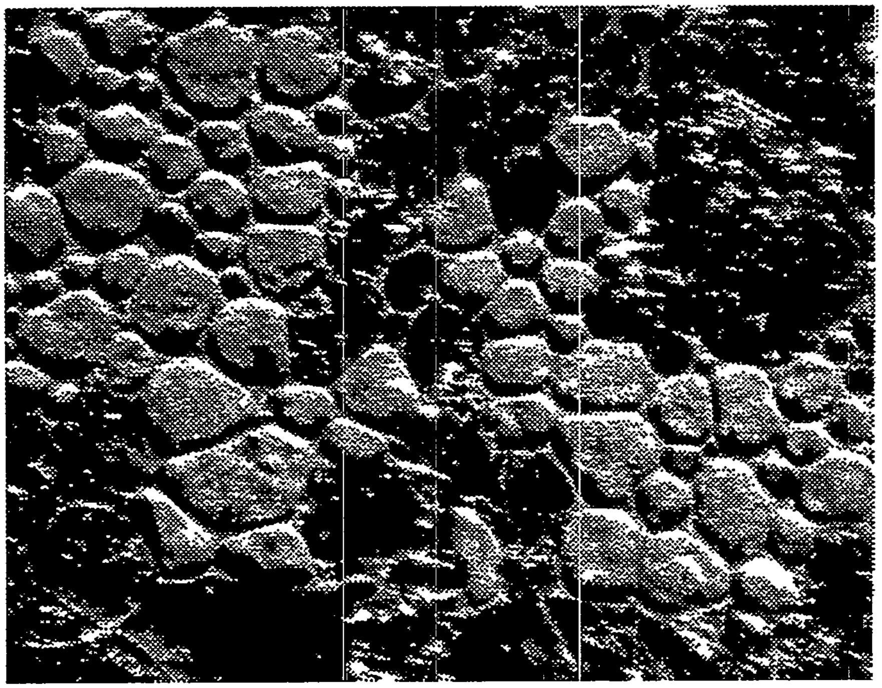

A) 12X

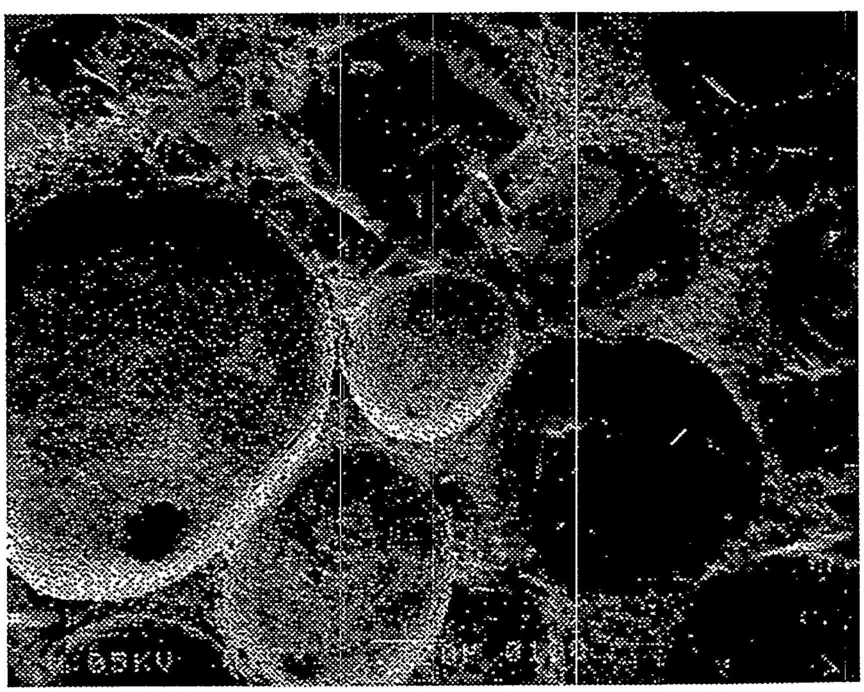

B) 77X

Figure 28: Macrostructure of Join Interlayer for Join Made With Initial Unsiliconized Silicon Carbide Parent Material

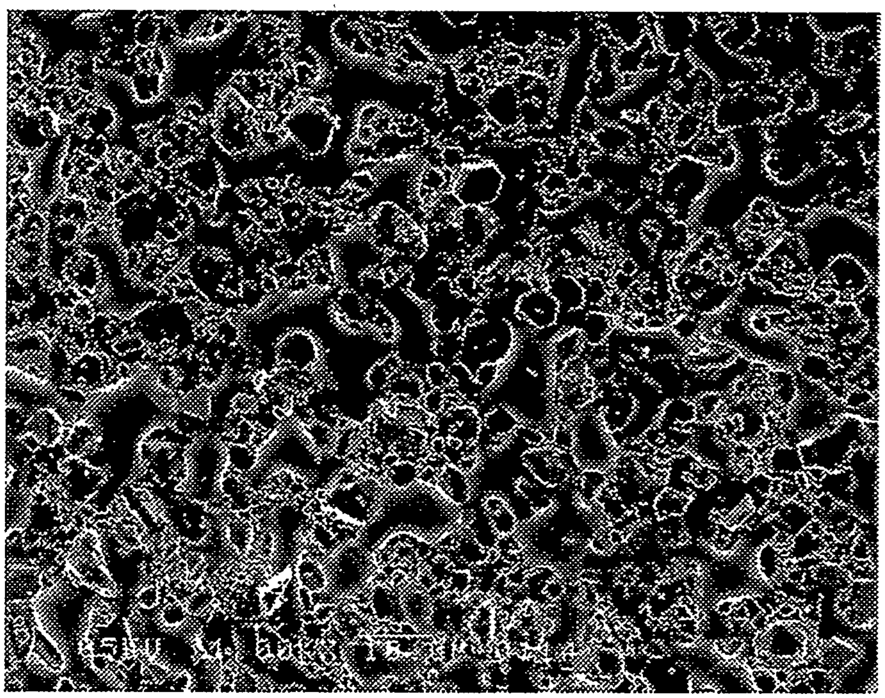

A) 1,000X

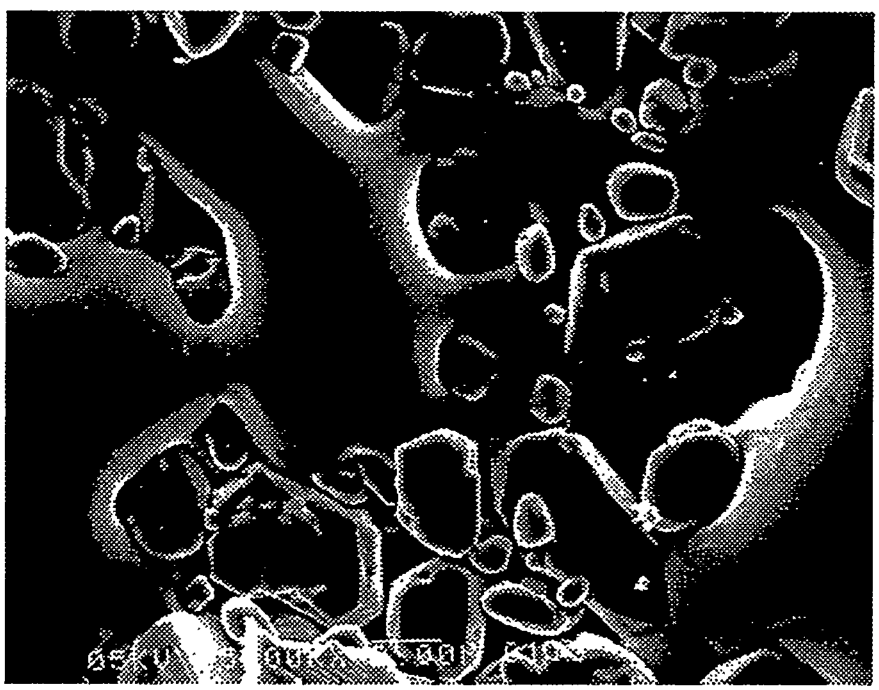

B) 5,000X

Figure 29: Microstructure of Join Interlayer for Join Made With Initial Unsiliconized Silicon Carbide Parent Material

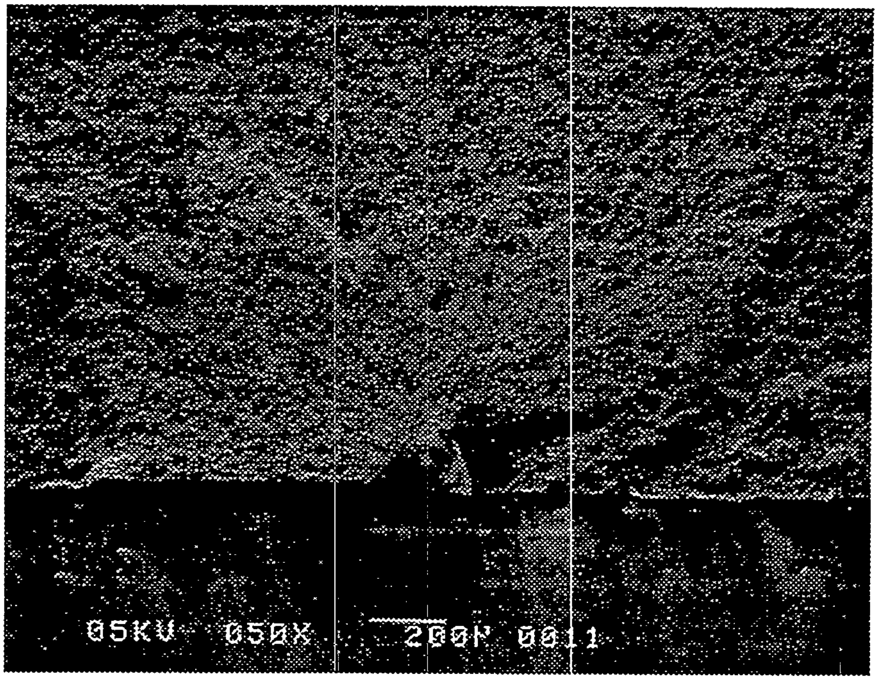

A) 50X

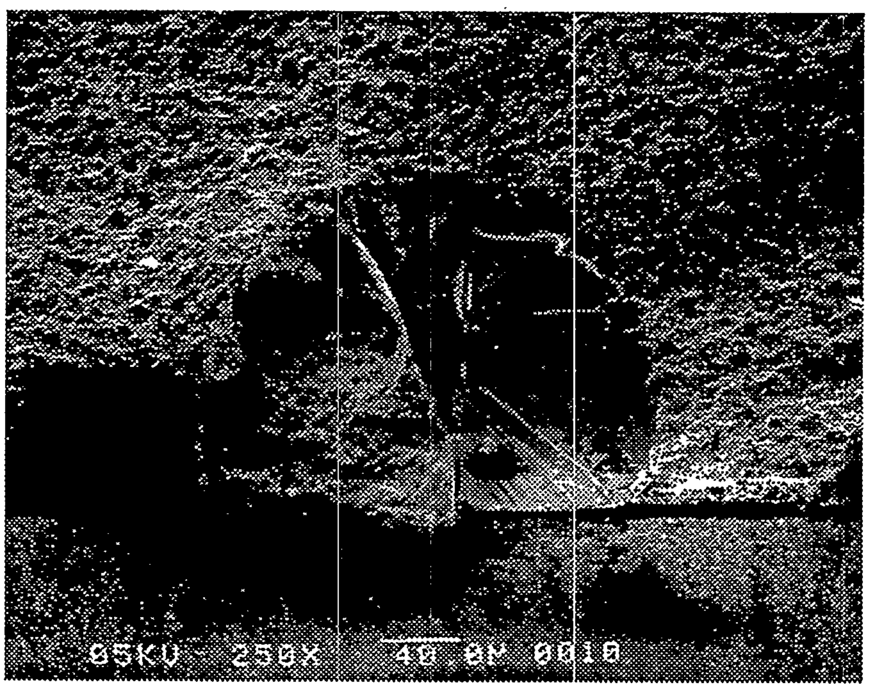

B) 250X

Figure 30: Fracture Origin Within Join Interlayer for Join Made With Initial Siliconized Silicon Carbide

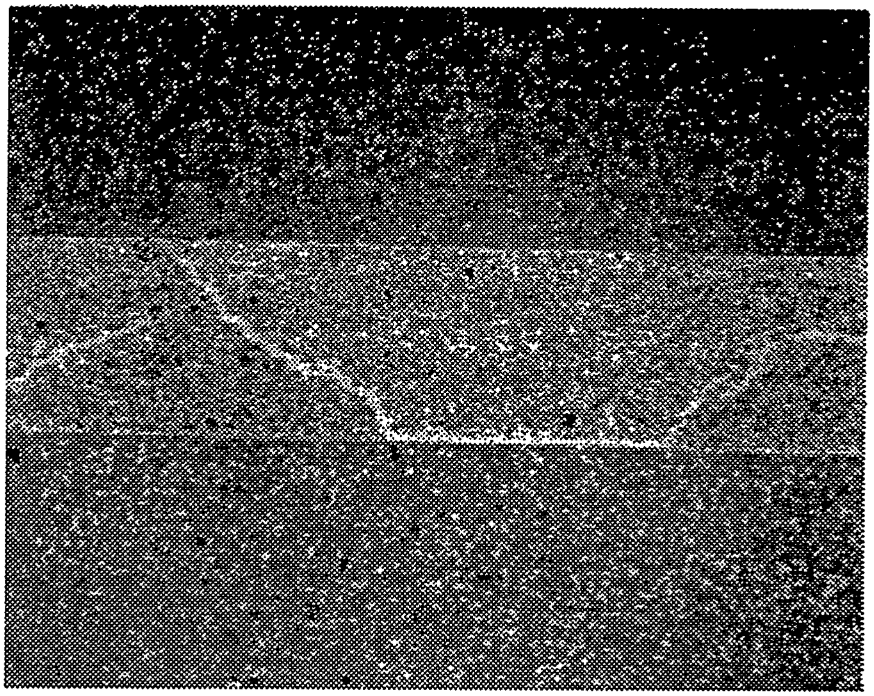

A) 200X

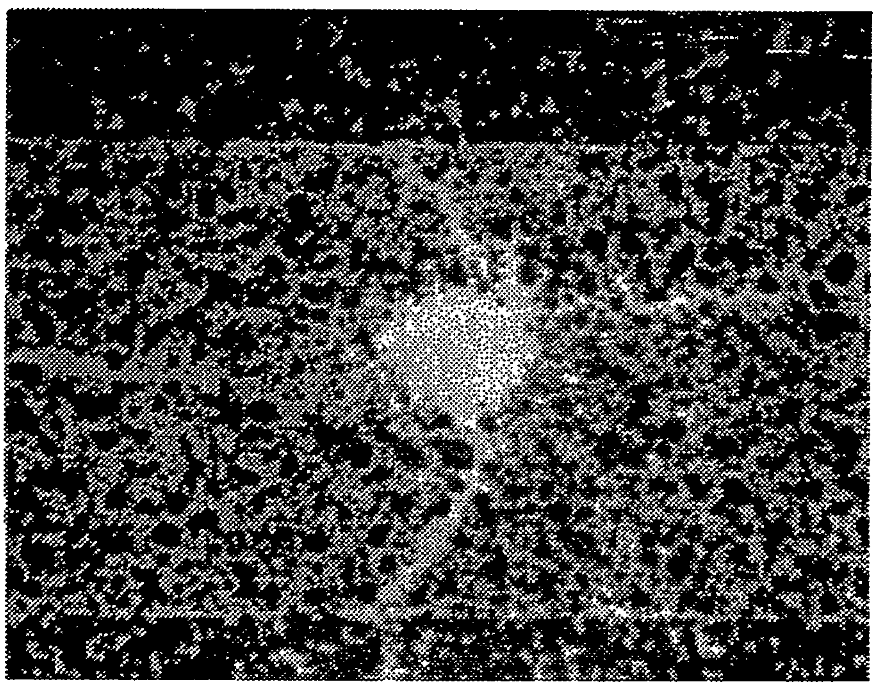

B) 500X

Figure 31: Optical Micrograph of Join Interlayer B Made With Initially Siliconized Parent Material

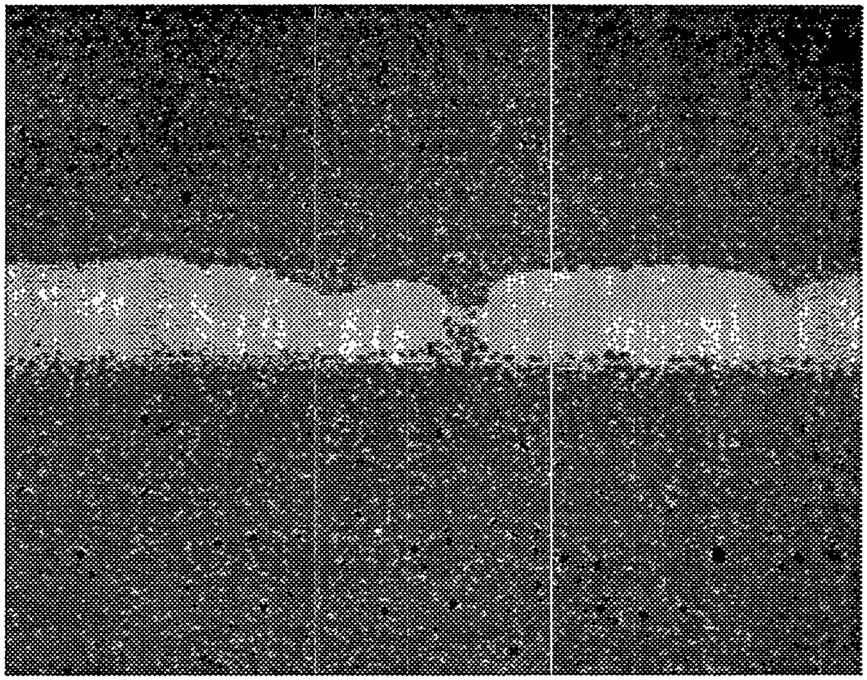

A) 200X

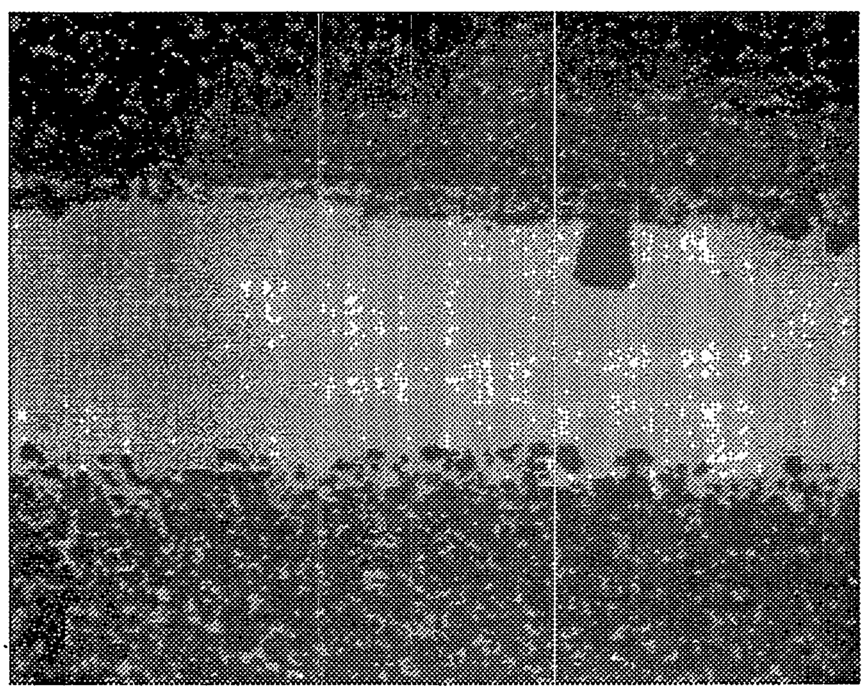

B) 500X

Figure 32: Optical Micrograph of Join Interlayer C Made With Initially Siliconized Parent Material

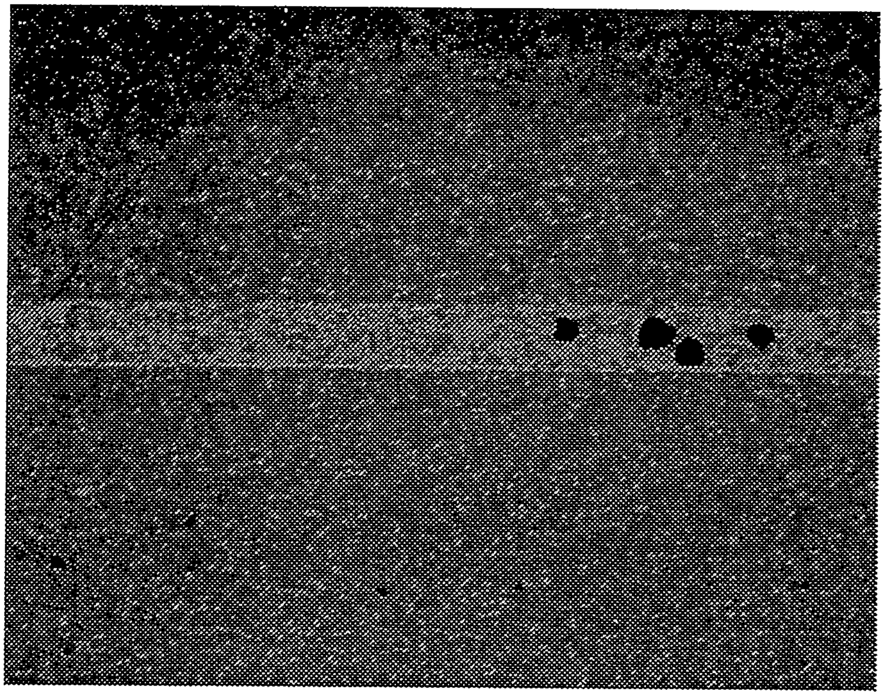

A) 200X

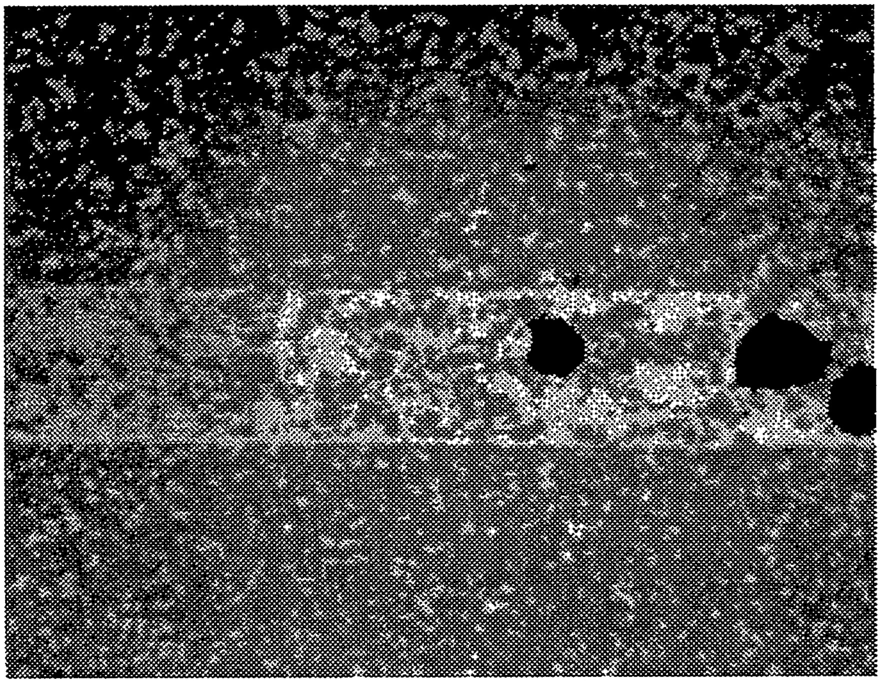

B) 500X

Figure 33: Optical Micrograph of Join Interlayer D Made With Initially Siliconized Parent Material

Parent

Join

Parent

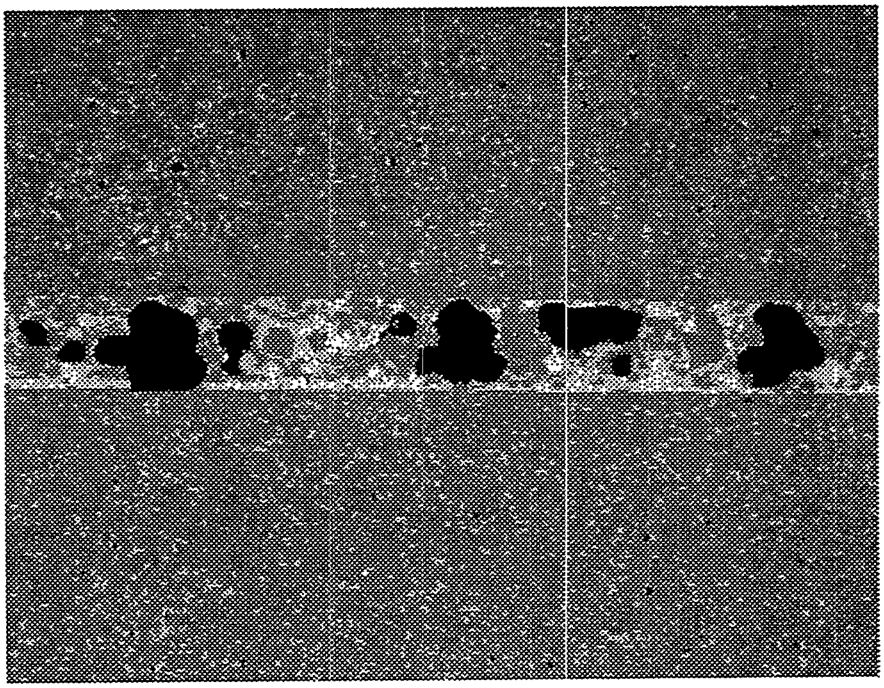

A) 200X

Parent

Join

Parent

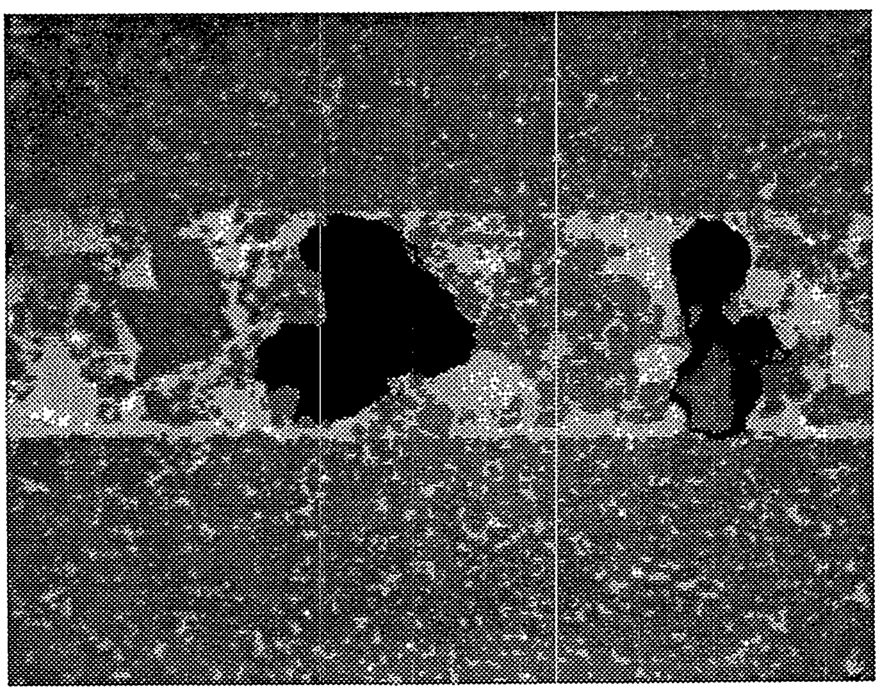

B) 500X

Figure 34: Optical Micrograph of Join Interlayer E Made With Initially Siliconized Parent Material

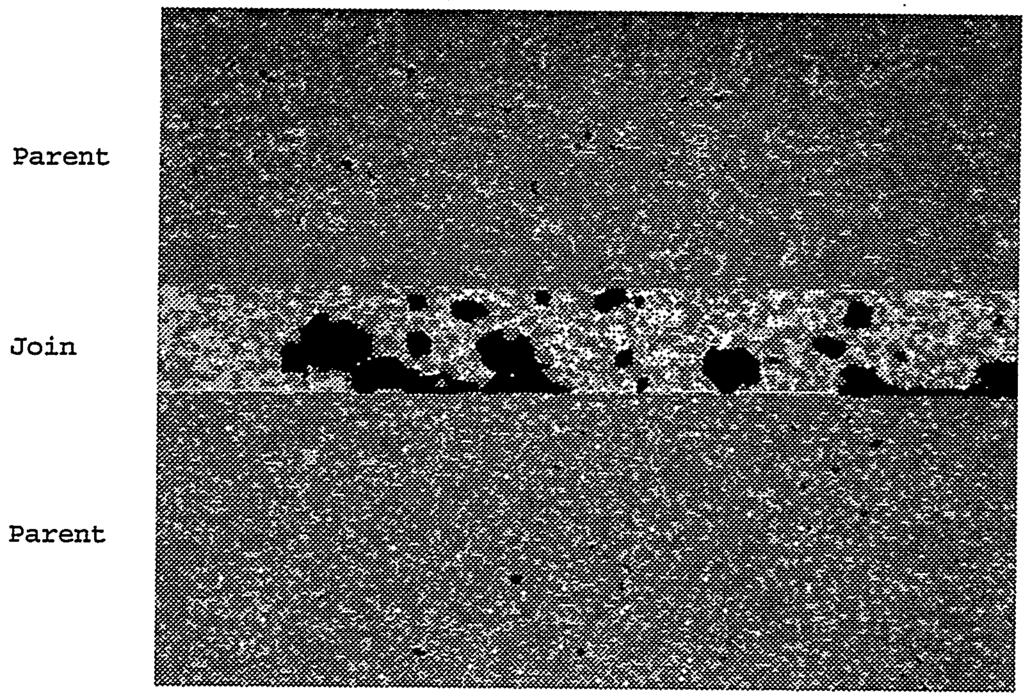

A) 200X

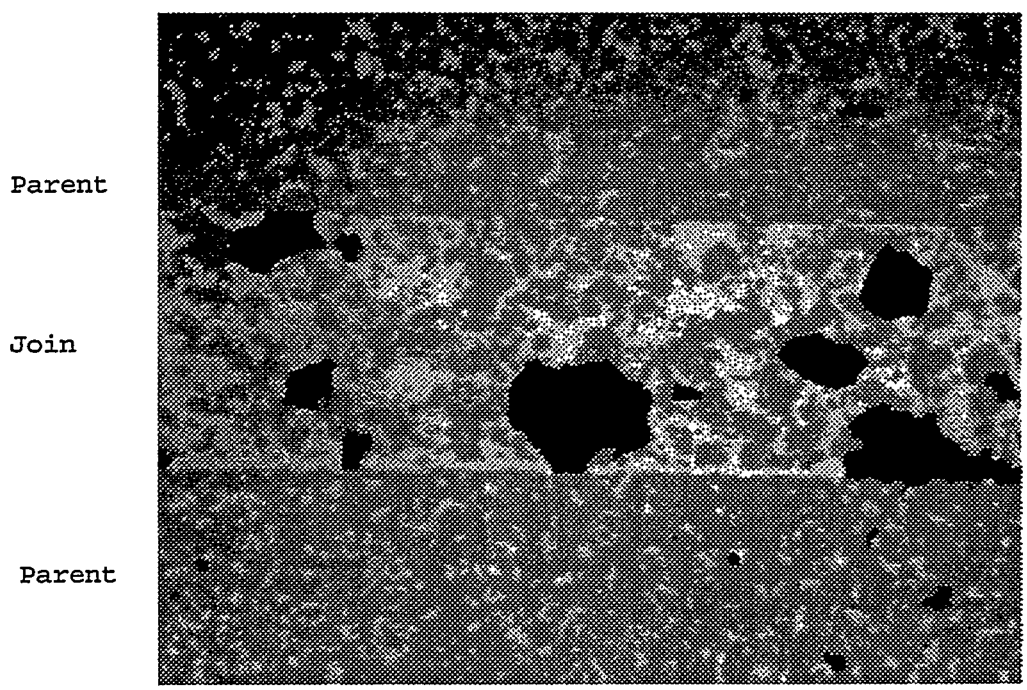

B) 500X

Figure 35: Optical Micrograph of Join Interlayer F Made With Initially Siliconized Parent Material

Parent

Join

Parent

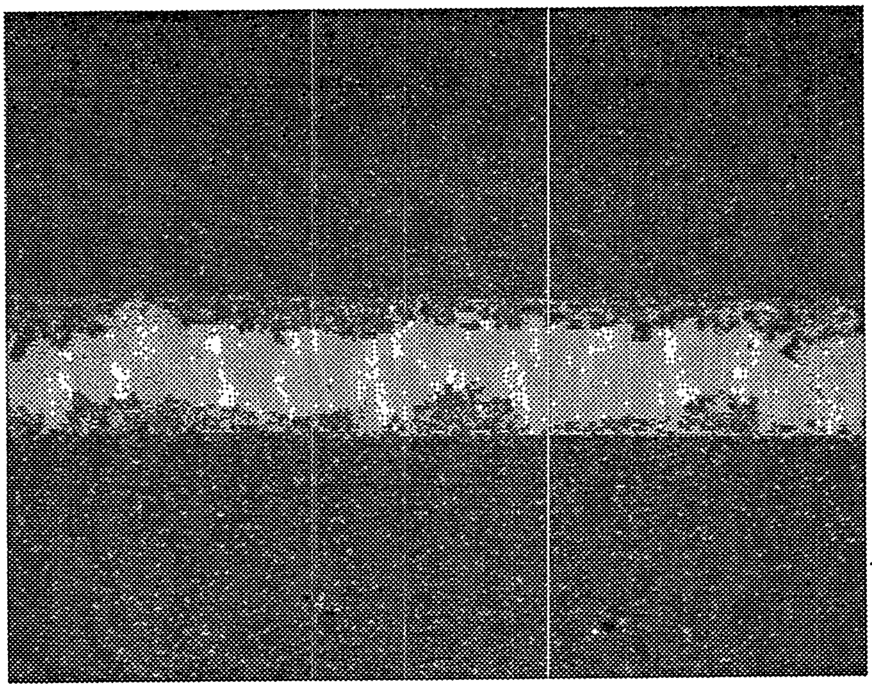

A) 200X

Parent

Join

Parent

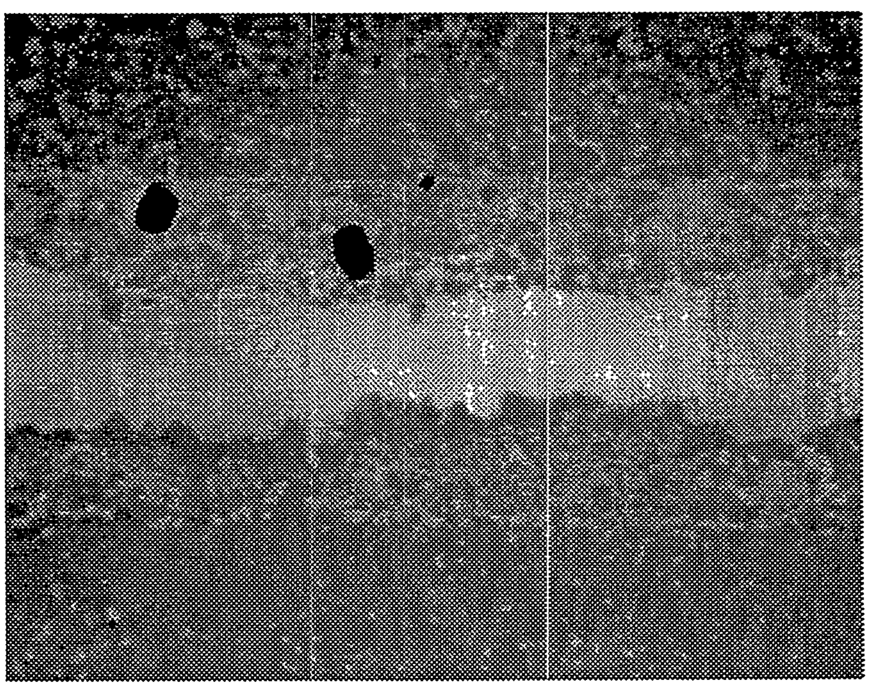

B) 500X

Figure 36: Optical Micrograph of Join Interlayer D Made With Initially Unsiliconized Parent Material

Table 11: Silicon Carbide Join Summary - Flexure Strength at 22°C

Billet	Interlayer	Flexure Strength (MPa)	Std. Dev. (MPa)	Number Tested	Number of Failed Joins
Siliconized	A	221.8	40.5	10	10
Siliconized	B	101.11	39.6	14	14
Siliconized	C	141.76	49.7	14	12
Siliconized	D	171.06	39.2	14	14
Siliconized	E	122.87	33.7	15	15
Siliconized	F	127.02	41.0	15	15
Unsiliconized	D	179.53	51.2	15	12
Unjoined Control 38mm Thickness		232.9	70.5	27	

uniform microstructure and the lowest silicon content (Figure 31). The join S-C and U-D demonstrated extreme silicon enrichment (lighter phase) in the center of the join interlayer with segregation of the silicon carbide (darker phase) at the edges of the interlayer adjacent to the parent materials (Figures 32 and 36). Although the joins S-B, S-D and S-F exhibit a more homogeneous distribution of silicon carbide and silicon, all of the joins lack a contiguous network of silicon carbide that extends into the parent material. All of the join methods resulted in join interlayers that were discrete relative to the parent materials and of higher silicon concentration. The distinct interface between the join interlayer and parent material consisted largely of silicon within the join and silicon carbide within the parent material with an absence of interpenetration across the interface. In addition, voids within the join interlayer are strength limiting and undesirable (Figures 33, 34 and 35).

Additional silicon carbide joining development is required to improve silicon carbide join quality.

9 SILICON NITRIDE TENSILE CREEP EVALUATION (TASK 1.1)

9.1 TENSILE CREEP RESULTS

The objective of this task was to evaluate the creep characteristics of parent (unjoined) and joined silicon nitride material when isothermally loaded in uniaxial tension at temperatures in the 1275-1425°C range. A summary of the results of the tests for the creep of both joined and parent material (control) specimens is given in Table 12. The table gives the stress, temperature and test time (to failure or suspension) for each specimen tested. The minimum creep rate and total creep strain reported in the table are for the entire gauge section of the specimen (D1,4). If the specimen did not exhibit a secondary creep regime, a minimum creep rate was not calculated and "primary" is entered in its place. Specimen 17-9 was ramped from a stress of 120 MPa to 150 MPa after 100 hours. The specimen had not reached the secondary region at 120 MPa and failed only five hours after the ramp. Consequently, no minimum creep rate was obtained for that specimen at either load.

The end result of each test is listed in the status column of Table 12. For the most part, the test was either suspended or the specimen failed. There were a few instances where the specimen was retested under different conditions which is noted in the status column. The comment for specimen 2-2, Failed (Torque), represents a premature failure of the specimen due to an accidental applied torque. Only one of the specimens, 47-5, had a failure at the pin hole, which is mentioned in the table. These two specimens are not included as failed specimens in later models. The three main locations of failure for the specimens tested were: (1) at the join, (2) at the transition region stress concentration (described in section 7.1.1) and (3) in the gauge section away from the join.

The classical characterization of creep deformation involves three regimes identified as primary, secondary and tertiary creep. Primary creep occurs at the beginning of the high temperature loading where strain rate rapidly decreases to a near constant value which is maintained during the secondary creep regime. The tertiary creep regime is identified by an inflection point in the creep curve where the strain rate increases above the secondary creep level. The strain rate continuously increases during this regime which is terminated by rupture.[10]

The creep test curves display a significant primary creep regime. However, none of the creep data, for tests as long as 1,692 hours, exhibit tertiary behavior when using the classical creep interpretation. An approximation to the steady state creep rate was established for those specimens which clearly deformed beyond the primary creep regime. The procedure taken here was to identify the nearly linear portion of the creep versus time curve, for the entire gauge section (D1,4), just prior to failure or test termination. This quasi-linear region was fit with a straight line and the slope of that line was used as the minimum or quasi-steady state creep rate.

Strain variations were observed along the gauge length within a given specimen. The strain variation within specimens was greatest between segments D1,2 and D3,4 which contained only the parent material without the join interlayer. The percent difference of strain at test termination between opposing halves of the parent material typically ranged between 5% to 57%. Specimen to specimen variability was also observed in tests conducted under identical conditions.

The data acquisition method was reviewed to ensure apparent strain variation was not an artifact induced by systematic error. No detectable temperature gradient was measured in the furnace hot zone at the creep gauge section when monitored with thermocouples. The high and low strain measurements for creep specimens were randomly oriented at the upper and

Table 12: Silicon Nitride Creep Test Summary

Specimen Number	Specimen Type	Stress (MPa)	Temp (C)	Minimum Creep Rate (1/hours)	Test Time (hours)	Total Creep	Status	Failure Location
30-3	Joined	100	1395	Primary	7	0.0029	Failed	Join
19-2	Joined	100	1422	1.775E-05	476	0.0124	Suspended	
19-4	Joined	100	1422	1.829E-05	444	0.0137	Suspended	
46-2	Control	100	1425	2.555E-05	486	0.0173	Failed	Transition
20-9	Joined	120	1327	Primary	448	0.0014	Retested as 20-9a	
30-5	Joined	120	1350	3.045E-06	425	0.0033	Retested as 30-5a	
17-9	Joined	120,150	1388	Primary	105	0.0038	Failed	Gauge
19-7	Joined	120	1392	8.263E-06	669	0.0080	Suspended	
17-8	Joined	120	1395	1.132E-05	601	0.0113	Failed	Transition
19-1	Joined	120	1395	8.897E-06	475	0.0075	Suspended	
46-1	Control	120	1397	1.097E-05	504	0.0076	Suspended	
20-2	Joined	120	1418	2.187E-05	448	0.0119	Suspended	
47-2	Control	120	1425	Primary	139	0.0103	Suspended	
47-3	Control	120	1427	2.615E-05	407	0.0151	Failed	Transition
20-1	Joined	120	1427	2.434E-05	202	0.0076	Failed	Join
20-3	Joined	120	1427	2.012E-05	384	0.0112	Failed	Transition
30-4	Joined	140	1422	Primary	3	0.0032	Failed	Join
20-9a	Joined	140	1300	6.603E-07	680	0.0004	Continuation of 20-9	
28C	Joined	141	1370	1.236E-05	170	0.0055	Suspended	
36B	Joined	145	1370	1.797E-05	134	0.0046	Suspended	
22E	Joined	146	1370	1.931E-05	144	0.0034	Suspended	
47-5	Control	150	1325	3.036E-06	311	0.0021	Failed at pin hole	
1-1	Joined	150	1350	1.403E-05	206	0.0044	Failed	Transition
17-1	Joined	150	1370	4.030E-05	93	0.0043	Failed	Join
17-4	Joined	150	1370	Primary	24	0.0039	Failed	Gauge
22B	Joined	150	1370	2.097E-05	149	0.0047	Suspended	
47-1	Control	150	1388	5.442E-05	72	0.0048	Suspended	
46-3	Control	150	1392	4.364E-05	141	0.0102	Failed	Gauge
1-5	Joined	175	1300	2.889E-06	363	0.0018	Suspended	
20-7	Joined	175	1318	2.967E-06	819	0.0060	Suspended	
30-2	Joined	175	1322	Primary	130	0.0036	Failed	Transition
20-8	Joined	175	1327	1.272E-06	1100	0.0032	Suspended	
30-6	Joined	175	1350	1.769E-05	223	0.0059	Failed	Transition
30-5a	Joined	175	1350	3.620E-06	687	0.0056	Continuation of 30-5	
33E	Joined	190	1300	7.856E-06	126	0.0025	Suspended	
2-1	Joined	200	1300	5.090E-06	350	0.0032	Retested as 2-1a	
2-2	Joined	200	1300	4.151E-06	110	0.0018	Failed (Torque)	
2-3	Joined	200	1300	3.906E-06	753	0.0048	Suspended	
2-1a	Joined	200	1325	1.444E-05	50	0.0011	2-1 Continued	Transition
17-5	Joined	200	1325	1.195E-05	233	0.0046	Failed	Transition
1-2	Joined	200	1350	1.357E-04	8	0.0017	Failed	Transition
1-3	Joined	200	1350	6.902E-05	26	0.0030	Failed	Transition
34B	Joined	210	1300	1.026E-05	159	0.0034	Failed	Gauge
19-9	Joined	225	1268	1.650E-06	506	0.0027	Failed	Transition
19-8	Joined	225	1277	1.091E-06	1692	0.0029	Suspended	
17-6	Joined	225	1318	4.927E-05	54	0.0093	Failed	Transition
20-5	Joined	225	1318	4.105E-05	42	0.0019	Suspended	
47-4	Control	225	1322	3.205E-05	70	0.0039	Failed	Gauge
30-1	Joined	225	1352	Primary	< 1	0.0008	Failed	Gauge
20-4	Joined	250	1272	Primary	8	0.0004	Failed	Transition
20-6	Joined	250	1272	2.253E-06	936	0.0043	Suspended	
19-6	Joined	250	1275	2.689E-06	890	0.0049	Failed	Join
2-5	Joined	250	1285	4.866E-06	447	0.0040	Failed	Gauge
2-4	Joined	250	1300	6.428E-05	18	0.0018	Failed	Gauge

lower ends of the creep specimen. The strain of the center segment (D2,3) and the overall gauge length (D1, 4) represented the creep of the join interlayer and the entire aggregate joined body, respectively, and correlated well with the weighted average of the measured creep segments (Figure 37) for all specimens. These findings confirm the measured strain variation to be an actual behavior difference and not an artifact from data acquisition.

Results indicate that creep strain variability also exists within the NCX-5101 unjoined (control) specimens (Figure 38). This suggests that creep strain variability is inherent in the silicon nitride. There was no apparent evidence that the joining process contributed to the creep strain variability observed in the joined specimens.

Fourteen of the 27 specimens which ruptured did so at the transition stress concentrator. Only five of the 23 joined creep specimens that failed did so at the join (Table 12). Several failed specimens were sectioned and analyzed with SEM. Analysis of micrographs showed the primary creep mechanism to be cavitation at two grain junctions (Figure 39).

9.2 MODELING OF CREEP

9.2.1 Steady State Creep Rate Model

Successful mechanical design methodology can be expected to include prediction of creep deformation which accumulates over the lifetime of high performance ceramic heat engine components. Designs which fully utilize the potential of high temperature ceramics will involve critical structural locations of components experiencing fully developed secondary creep over the majority of the component's life. This requires an analytical approach to generalize the experimental findings on the stress and temperature dependence of the steady state creep rate.

The literature documents an extensive history of representing the stress dependence of the strain rate by a power law form both for metals[11] and ceramics[12]. This relationship is referred to as Norton's law, following the original publication by F.H. Norton[13] on the creep of steel. The temperature dependence of strain rate has been typically represented by an Arrhenius form to yield the following expression for the steady state strain rate $\dot{\varepsilon}_s$:

$$\dot{\varepsilon}_s = A\sigma^n e^{-Q/RT} \qquad (4)$$

Here A and n are material constants, σ is the applied stress, Q is the apparent activation energy for creep, R is the universal gas constant, and T is the absolute temperature. In order to fit the data shown in Table 12 to Equation 4 first consider the natural logarithm of Equation 4:

$$\ln\dot{\varepsilon}_s = \ln A + n\ln\sigma - \frac{Q}{RT} \qquad (5)$$

The values of Q, n, and A can be determined from plotting $\ln(\dot{\varepsilon}_s)$ against various parameters. The value of Q was determined from plotting $\ln(\dot{\varepsilon}_s)$ versus 1/T at constant stress (Figure 40). The value of Q is the negative of the slope of such a curve multiplied by the universal gas constant (R). In Figure 40 we see that the calculated value of the apparent activation energy, Q, varies with the value of the applied stress. There is an approximately linear increase in Q with stress. This trend has also been observed for the creep of sintered silicon

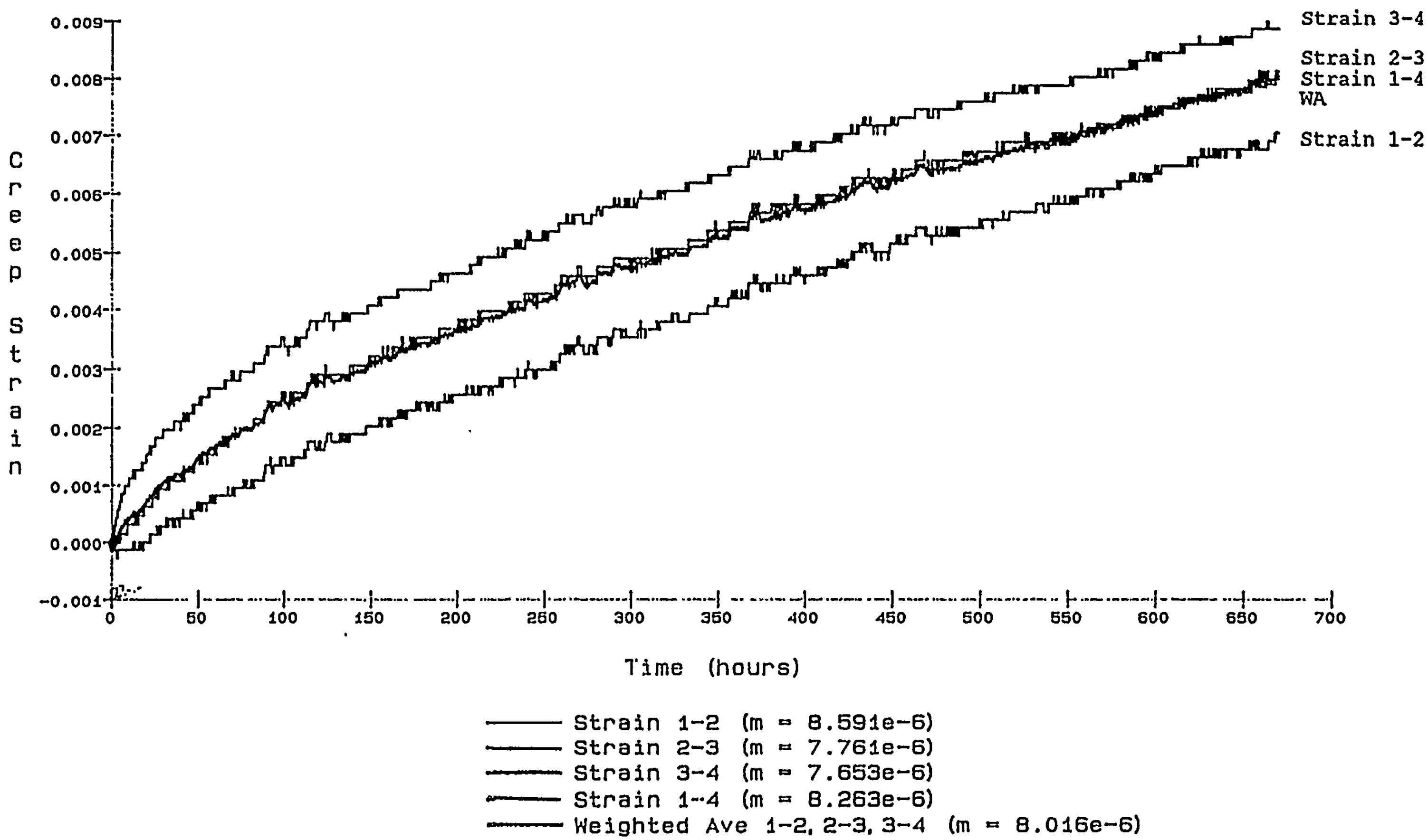

Figure 37: Creep Strain as a Function of Time for Silicon Nitride Butt Join #19-7 at 1392°C and 120 MPa. Test Suspended After 669 Hours.

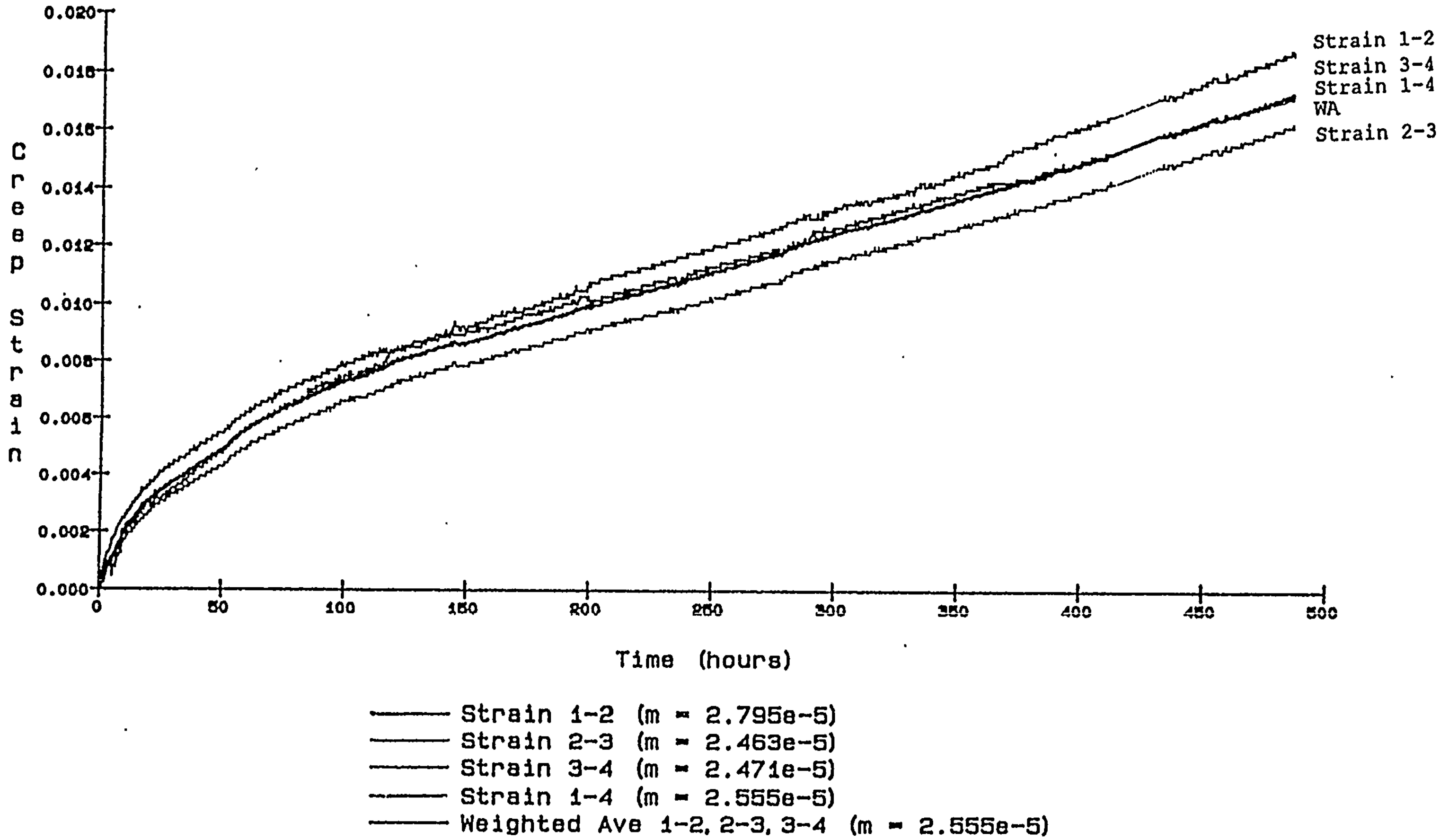

Figure 38: **Creep Strain as a Function of Time for Silicon Nitride Unjoined Control #46-2 at 1425°C and 100 MPa. Specimen Failed at 486 Hours.**

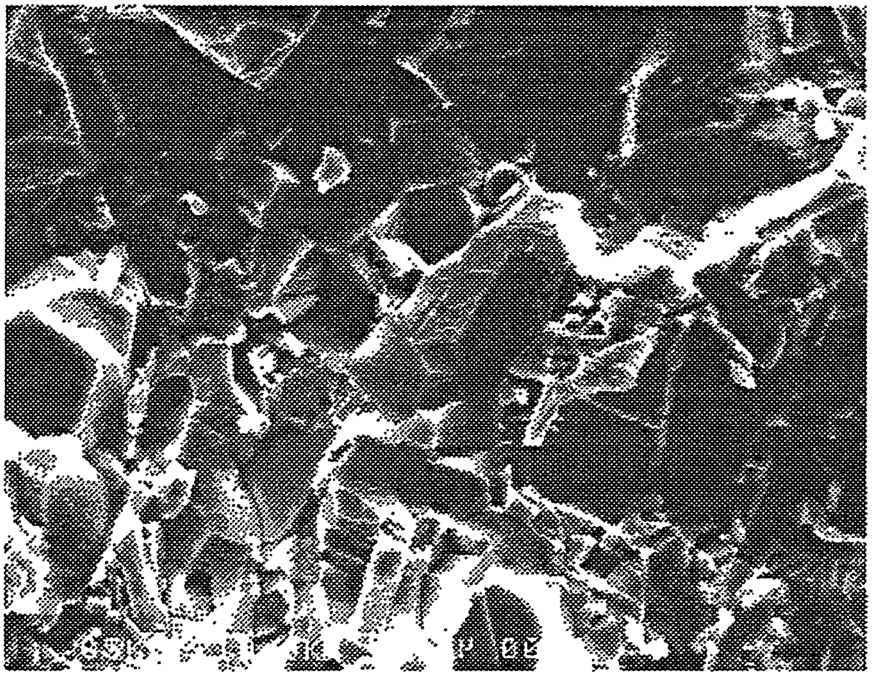

A) 10,000X

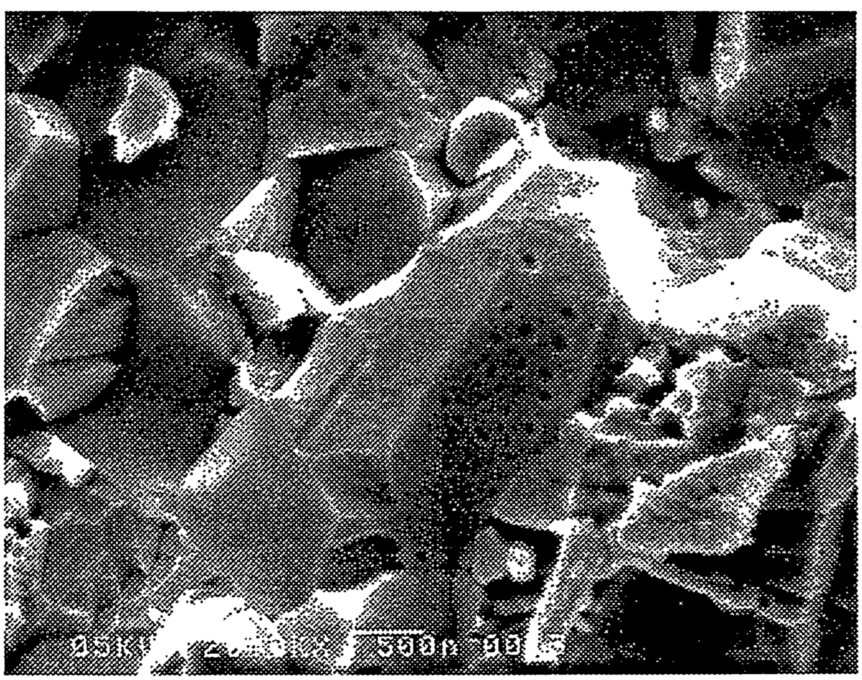

B) 20,000X

Figure 39: NCX-5101 Silicon Nitride Joined Tensile Specimen After Creep Testing Exhibiting Cavitation

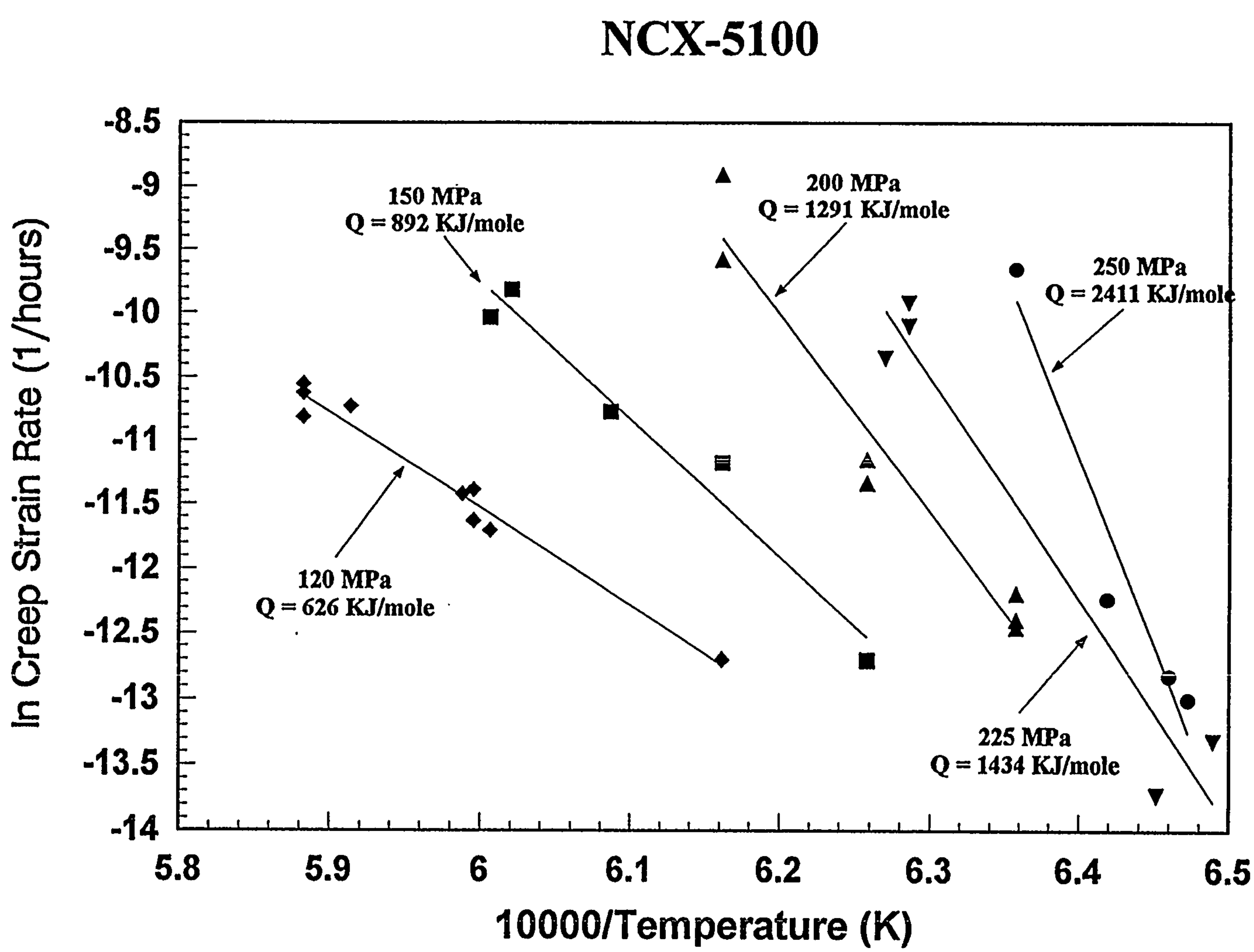

Figure 40: Determination of the Activation Energy (Q) as a Function of Stress

nitride[12]. The range of measured values in Q going from 626 KJ/mole to 1434 KJ/mole is consistent with other values from the literature[14, 15]. The value for Q=2411 KJ/mole shown for 250 MPa is not considered to be real since it is strongly influenced by a data point which appears to be an outlier. This phenomenon of increasing Q with stress needs further investigation. There is evidence from the literature of the creep of metals for Q to decrease with stress but not to increase. There has been data generated on NCX-5101 class materials that demonstrates that grain boundary devitrification occurs with thermal aging[16]. It is possible that this phenomenon which translates into improved creep resistance is promoted by stress thus explaining the observed increasing Q with stress. Additional evaluation of this phenomenon was beyond the scope of this study.

The value of n was determined from the slope of a $\ln(\dot{\varepsilon}_s)$ versus $\ln(\sigma)$ plot at constant temperature (Figure 41). The values of n showed some variation but were centered around a value of 7 for all of the temperatures except for the results at 1420°C. This possibly suggests a change of mechanism at this temperature.

In order to apply Equation 4 in a finite element analysis to model creep deformation in notched creep specimens which were tested, unique representative values of A, Q and n were sought. An iterative procedure was used, starting with the average value n=7.52 obtained by excluding the 1420°C data in Figure 41. Rearranging Equation 5 as:

$$\ln(\dot{\varepsilon}_s \sigma^{-n}) = \ln A - \frac{Q}{RT} \tag{6}$$

provides a way to obtain values of A and Q which correspond to the average value of n. The value of -Q/R is the slope of the line fit to $\ln(\dot{\varepsilon}_s \sigma^{-n})$ versus 1/Temperature and ln A is the intercept of this line. Likewise, an improved estimate for n can be deduced from data plotted to the form:

$$\ln(\dot{\varepsilon}_s e^{Q/RT}) = \ln A + n \ln\sigma \tag{7}$$

This value for n can then be used to determine a new value of Q using the procedure corresponding to Equation 6. This procedure can then be repeated as many times as necessary to give converged values for n, Q (and A). In practice it took only one iteration to converge to the values of n=7.53, Q=1138 KJ/mole, and A=8.28×10^{-31} $Pa^{-7.53}$/hour from Figures 42 and 43. These values were calculated excluding data at 1420°C which gave a low n value, excluding 250 MPa data which gave a high Q value and excluding 175 MPa data because of the excessively high scatter in that data. These are the values for the material parameters that were used to characterize the range of creep experiments. A calculation for these material parameters was also done based on all the data. The average value of n=7.52 was again used to start the iterative procedure. After 15 iterations, values of Q=1158 KJ/mole and n=7.20 were obtained, which are very similar to the previous results.

In order to evaluate how well the first set of constants represents the database as a whole, a three dimensional plot is given in Figure 44. In this plot a surface is drawn which represents the creep strain rate given by Equation 4 using the constants determined above. In addition to this surface given by the model, the individual data points are also plotted. There is a 68% average difference between the model predictions and the experimental points. This fit is good considering that only three material constants are used to correlate dozens of experiments.

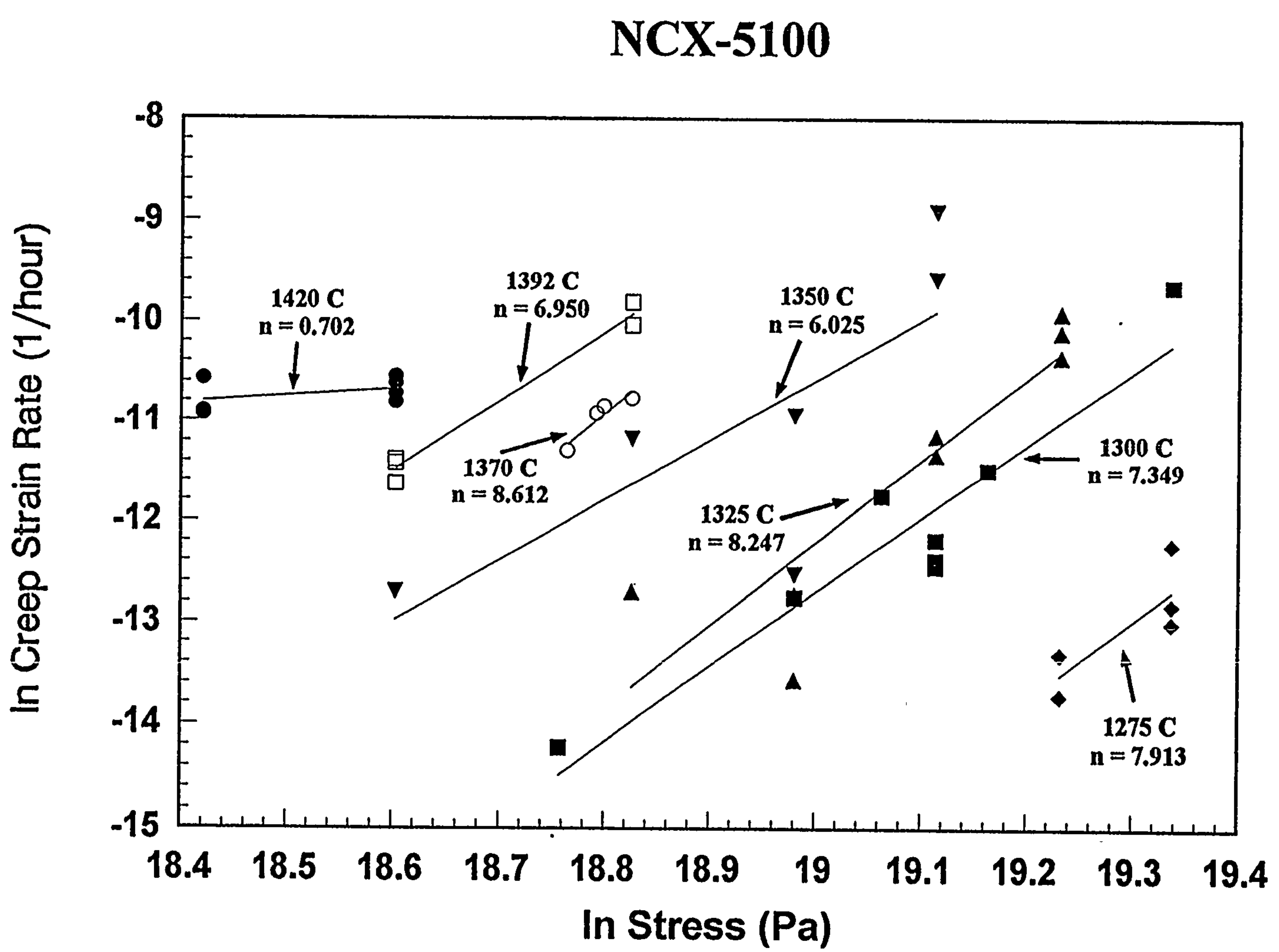

Figure 41: Determination of the Stress Exponent (n) as a Function of Temperature

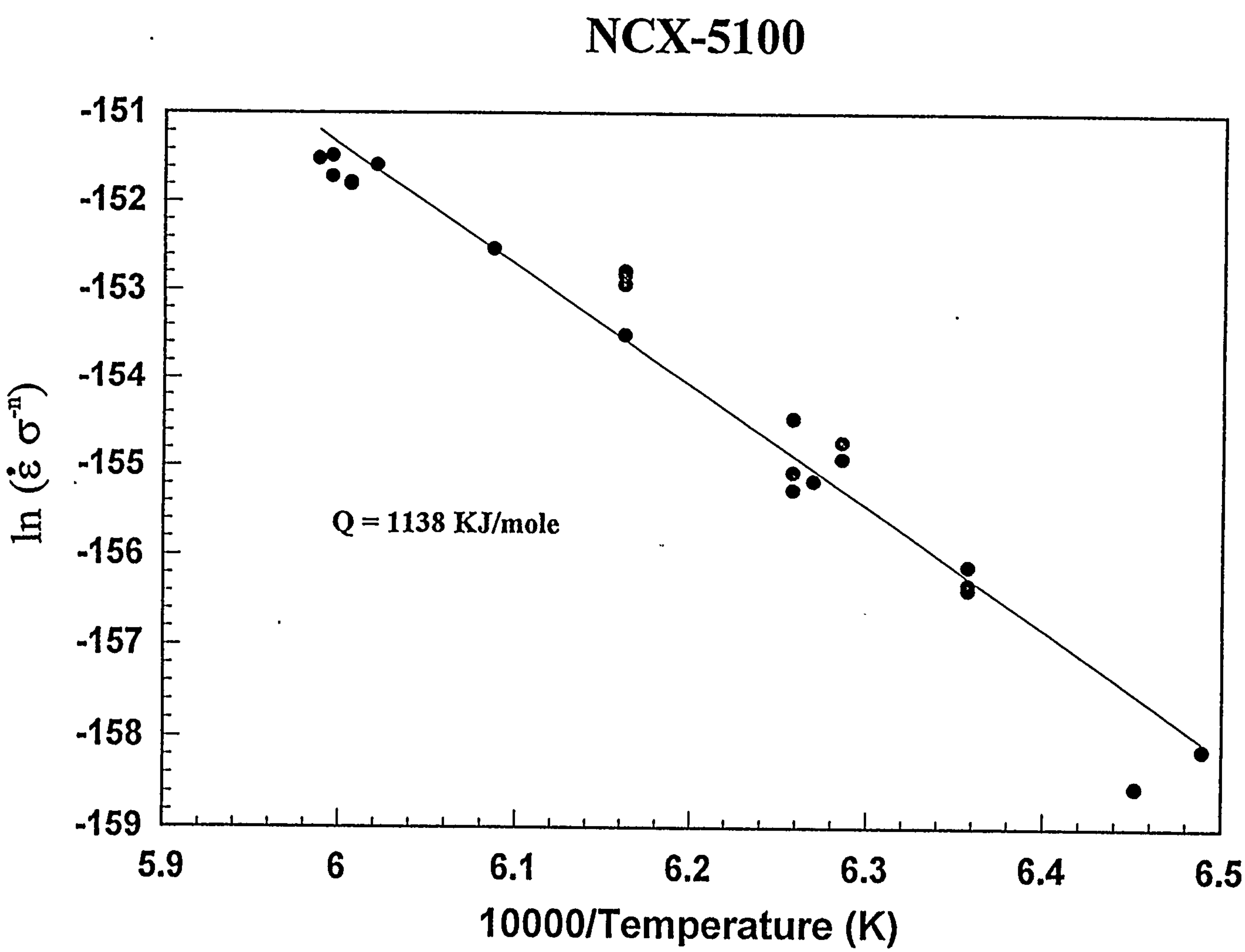

Figure 42: Determination of a Single Activation Energy (Q)

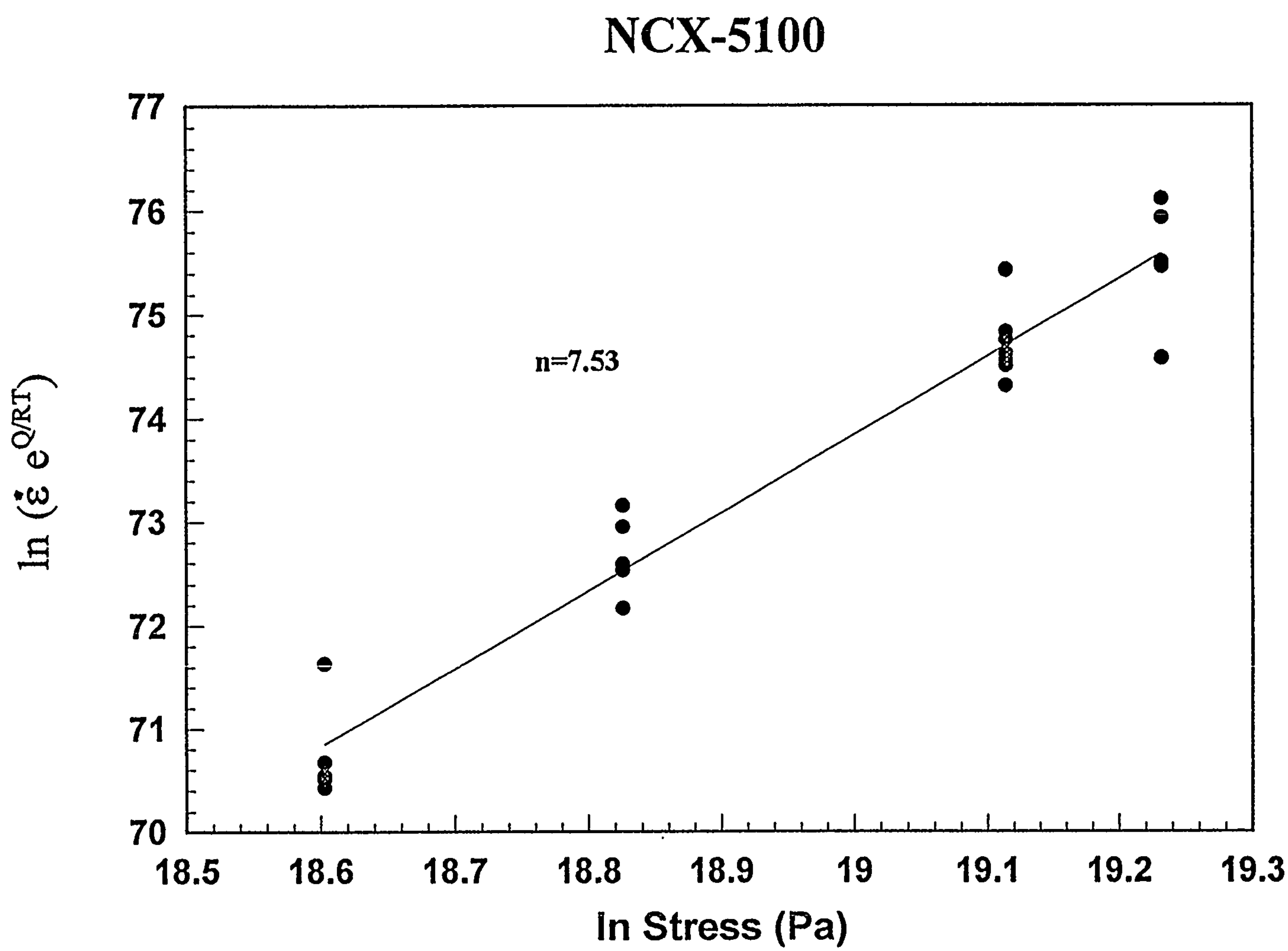

Figure 43: Determination of a Single Stress Exponent (n)

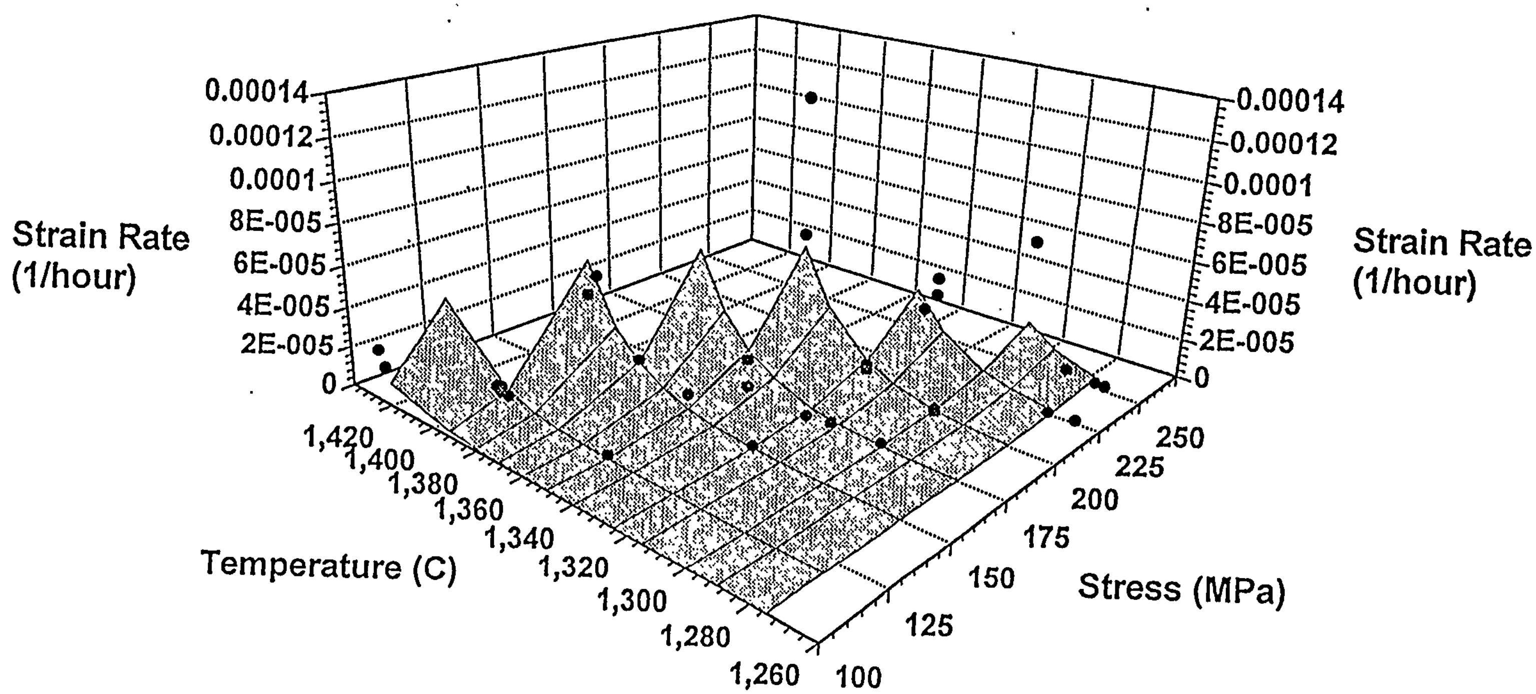

Figure 44: Creep Strain Rate Prediction Versus Experimental Results

9.2.2 Failure Modeling

The time to failure for each of the specimens which ruptured is given in Table 12. Twenty-nine of the 51 specimens were tested until failure. Of the 29, seven failed in the primary regime, two were premature failures (pin hole failure and accidental applied torque to specimen), and one (2-1) was tested at two different stresses. This leaves 19 valid data points for failure modeling. The time to failure of these specimens is plotted in Figure 45 versus minimum creep rate. The trend of the data suggests agreement with the Monkman-Grant[17] relationship:

$$\dot{\varepsilon}_s^{\beta} t_f = C \tag{8}$$

where t_f is the time to failure and the Monkman-Grant parameters β and C are 1.43 and $2.95\text{x}10^{-5}$ $\text{hr}^{-0.43}$ when the 19 data points are included in a linear regression. It is important to note that 11 of the 19 ruptured specimens included in Figure 45 failed at the section where the transition region blends into the straight gauge length. This section is beyond the range of the creep measurement flags so that the $\dot{\varepsilon}_s$ values for these specimens, although accurate for the gauge section, are not consistent with the rupture time data.

Data for the eight gauge/join failures are plotted separately in Figure 46 and provide values of 1.17 for β and $4.11\text{x}10^{-4}$ $\text{hr}^{-0.17}$ for C. The Monkman-Grant approach is motivated by the theory that rupture occurs at a critical value of accumulated creep strain (ie. β=1). On this basis, the β value of 1.17 is considered more accurate than the β value of 1.43 calculated previously for all ruptured specimens used in Figure 45.

9.2.3 Prediction of Creep Failure of Notched Tensile Specimens

The development of material models are useful only insofar as the model can be used to predict the performance of structural components. The finite element method is the most popular and, arguably, the most flexible numerical method for application of advanced material laws to actual components. An investigation to use these models in the prediction of the response of complex members has been pursued in conjunction with the development of material models to describe the joins and parent material.

The results being reported here involve incorporating the Norton's law modeling into a finite element code and demonstrating how it can be used to predict the mechanical response of a structure.

The commercially available finite element code ANSYS[6] has been used in this work. Since the strain rates evolve with time and temperature the solution must be tracked in an incremental manner. The one-dimensional Norton's law can be generalized to represent multiaxial deformation as follows:

$$\dot{\varepsilon}_{ij}^{cr} = A\sigma_e^n e^{-Q/RT} \frac{3}{2} \frac{\sigma'_{ij}}{\sigma_e}, \tag{9}$$

where σ'_{ij} is the stress deviator tensor, and σ_e is the equivalent stress (σ_e = $(3/2\ \sigma'_{ij}\bullet\ \sigma'_{ij})1/2$). The total strain rate is given as the sum of the elastic strain rate and the creep strain rate as given above.

Several criteria were used to select a component to apply the finite element method. The component was required to have: (1) a nonuniform stress and strain distribution, primarily tensile loading

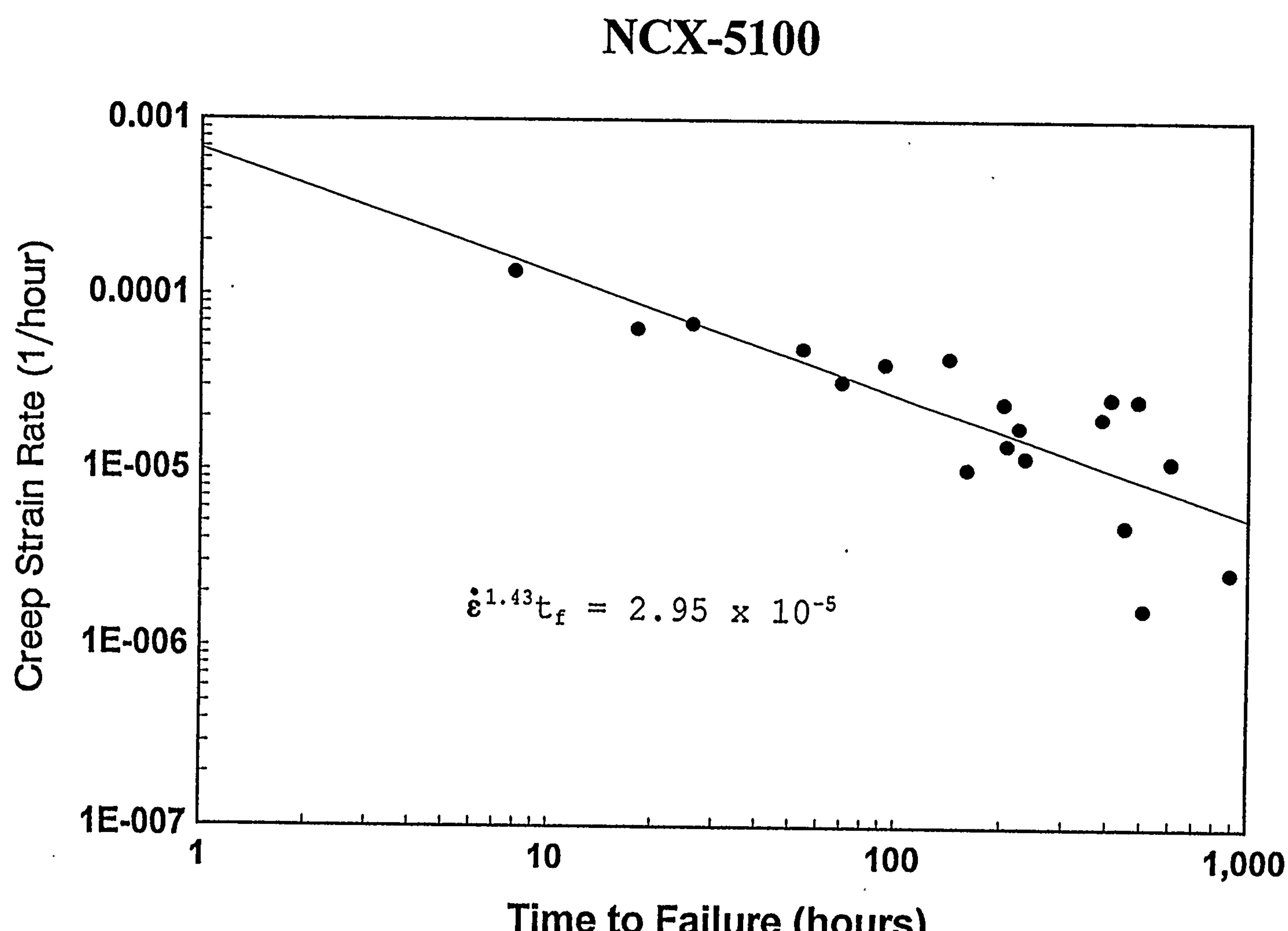

Figure 45: Monkman-Grant Relationship for All Failures

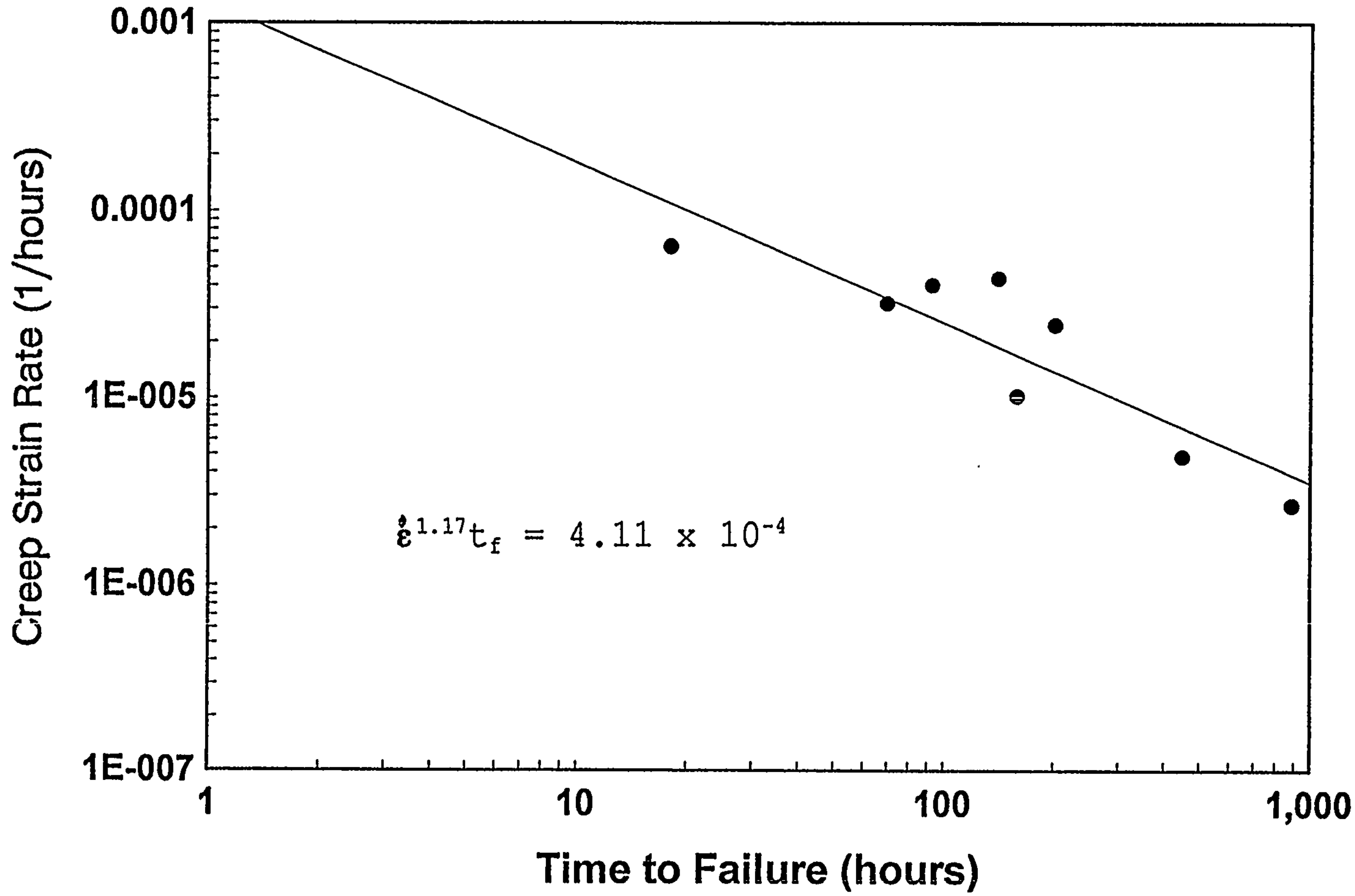

Figure 46: Monkman-Grant Relationship for Join or Gauge Failures

since the material constants were determined from tensile loading; (2) a fairly simple geometry; and (3) amenability to being tested experimentally. Guided by the above considerations, a notched, cylindrical tensile member was selected (Figure 47). The specimen has a semicircular notch at the center of the gauge section. The finite element mesh used in the analysis is represented in Figure 48. The figure shows one-half of an azimuthal section with the center line and notch apparent. An expanded view of the notch root mesh is given in the bottom view of the figure. The geometry was meshed with several different refinements to ensure that sufficient elements were used. The mesh shown in Figure 48 has 848, eight node, axisymmetric elements. A mesh convergence study using a mesh having 3984 elements verifies the results obtained with the coarser mesh. The model is loaded by applying a far field tensile stress to the top of the specimen and setting the temperature to 1370°C everywhere in the mesh. The far field stress corresponds to the loads from the experiments. This simulation was conducted assuming isothermal conditions, but that is not a necessary requirement. The load was applied, then the specimen was allowed to creep for up to 150 hours in 600 equal time increments to capture the nonlinear creep behavior. This was a much finer time division than required by the convergence criterion specified in ANSYS.

Experimental and Model Results

Three dogbone specimens with notched cylindrical gauge sections (Figure 47) were tested in creep at three different stress levels as described in Table 13. The specimen length is 3.5". The minimum and maximum diameters are 0.100" and 0.125" respectively. The experiments were carried out according to the procedures described in the Tensile Creep Test Methodology of section 7.1 in this report.

Table 13: Silicon Nitride Notched Tensile Creep Summary

Specimen Number	Test Temperature (C)	Reduced Section Average Stress (MPa)	Failure Time (Hours)
1	1370	120	44
2	1370	135	39
3	1370	150	3.5

The results for an analysis which applies a far field tensile load such that the average stress across the notched section is 120 MPa (specimen #1), are presented for two different times. Immediately upon loading, the elastic solution gives the maximum stress in the root of the notch as 260 MPa. In Figure 49 the vertical normal stress, σ_{yy}, is plotted at 10 hours and 100 hours of deformation. Note that at short times the vertical normal stress has its maximum at the notch root as would be expected from linear elastic analysis. As the creep deformation continues the creep strain builds up at the notch root and redistributes the stress more evenly across the section. It is shown that the stress is more uniform as the creep strain increases. The accumulated creep strain at 100 hours has its maximum at the notch root, as shown in Figure 50.

The failure was predicted for these experiments by obtaining the maximum vertical normal stress at the notch root during deformation as

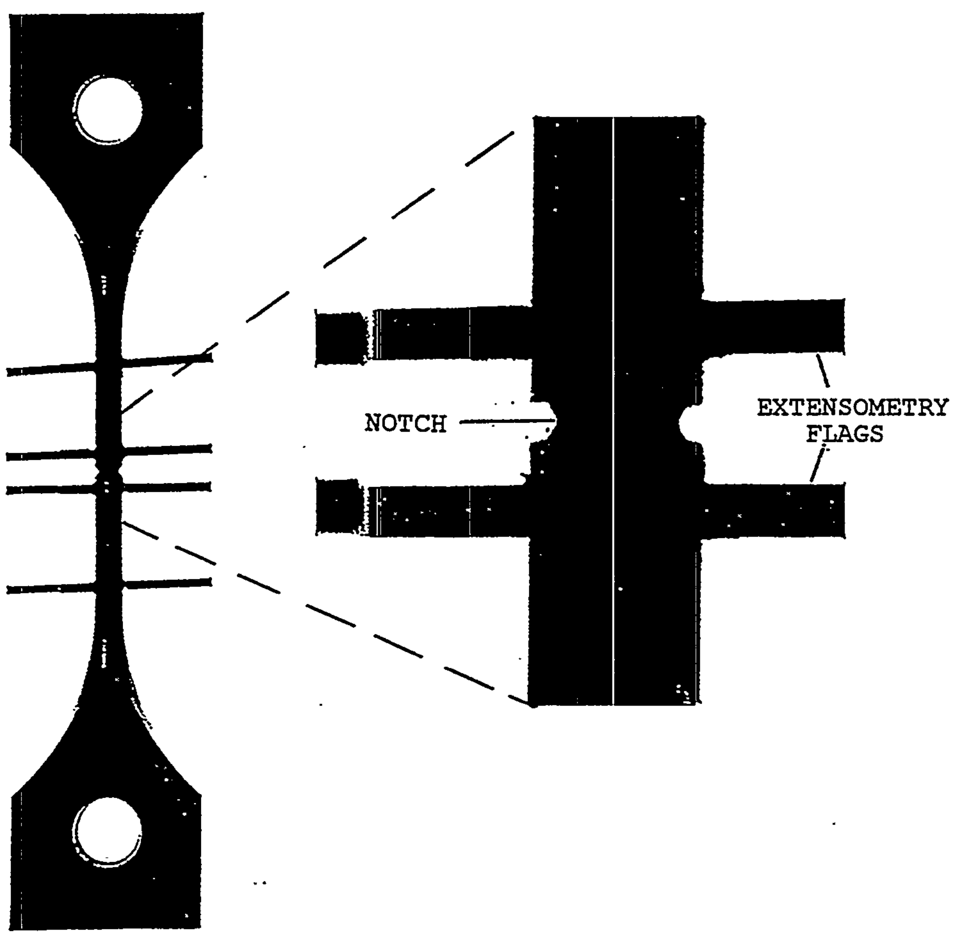

Figure 47: Pinloaded, Notched Cylindrical Gauge Section Tensile Creep Specimen With Extensometry Flags

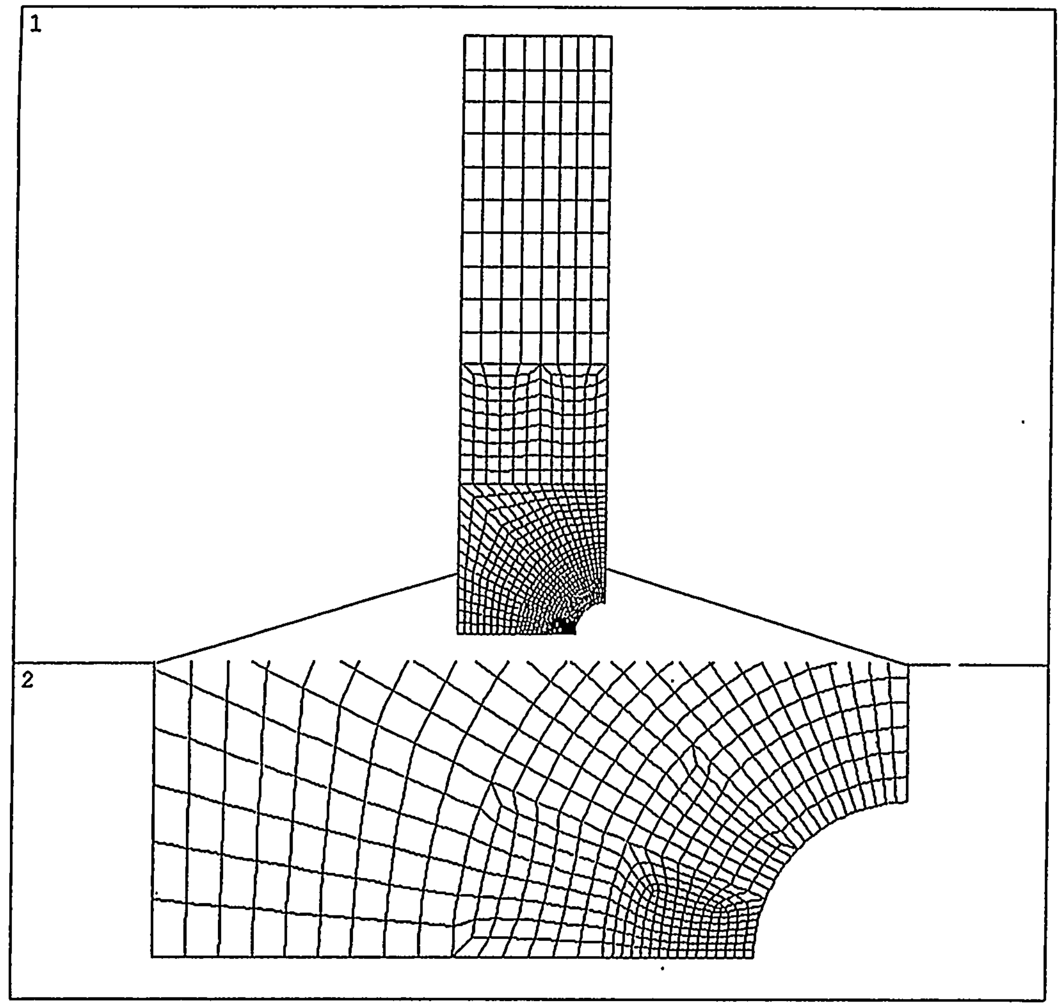

Figure 48: Notched Cylindrical Tensile Creep Specimen Finite Element Mesh

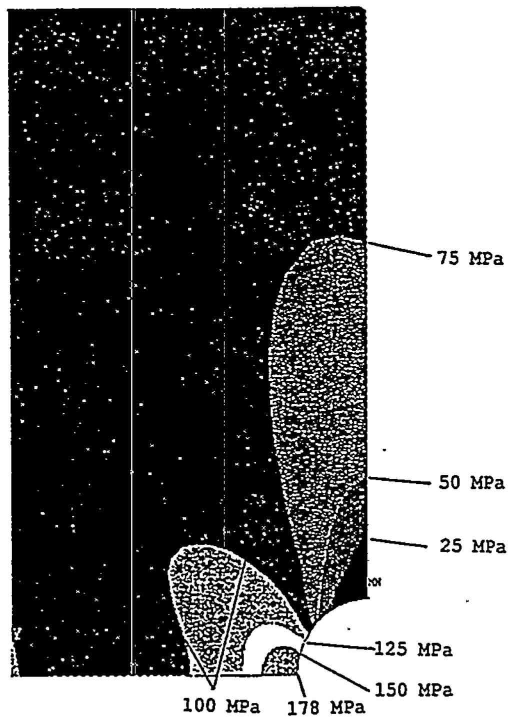

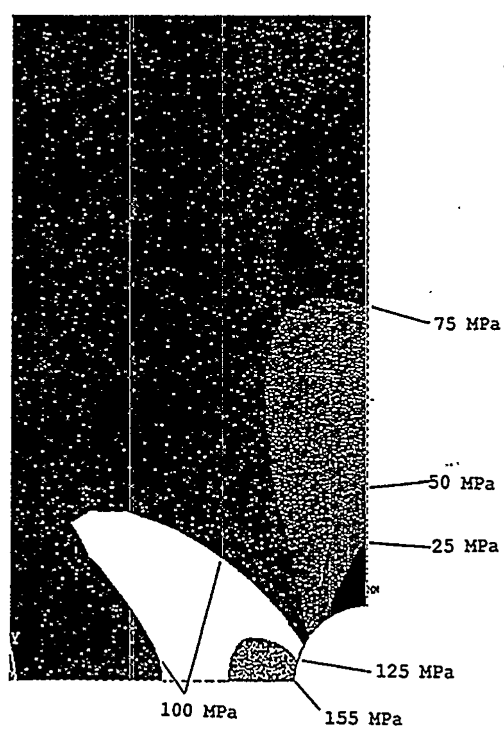

Figure 49: Distribution of Stress Component σ_{yy} Under 120 MPa Reduced Section Applied Stress at 1370°C

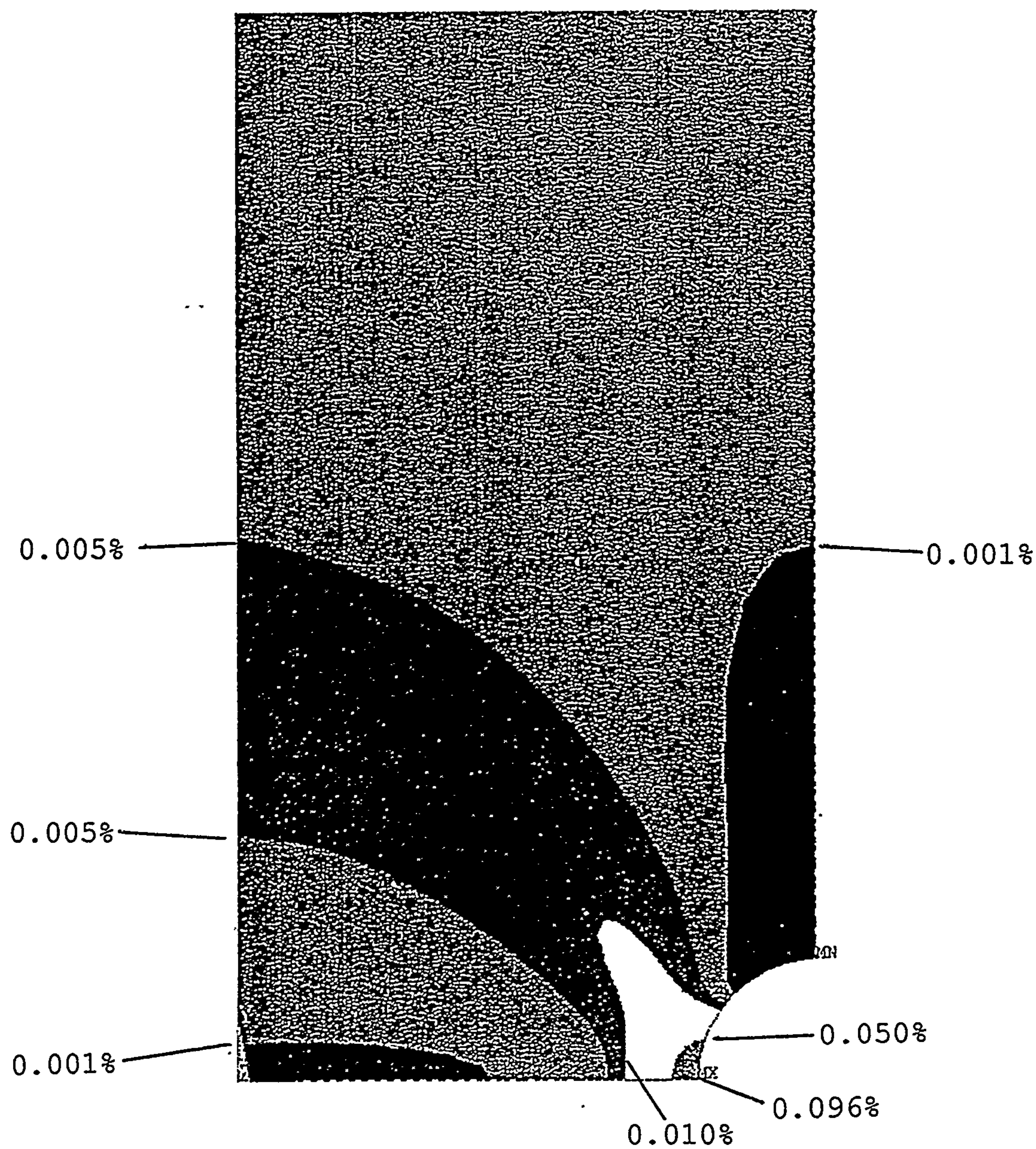

Figure 50: Distribution of Creep Strain ε_{yy} in Notched Specimen After 100 Hours Under 120 MPa Reduced Section Applied Stress at 1370°C

a function of time from the finite element analysis. The corresponding creep strain rate (from Norton's equation) was then used to investigate whether the Monkman-Grant relationship, obtained from conventional creep measurement of silicon nitride butt joins (Section 9.1, was satisfied. The time variation of the notch root creep strain rate is plotted along with the Monkman-Grant curve, determined earlier in Section 9.2.2 based on gauge/join failures in the flat creep tensile specimens, in Figure 51 for the three specimens tested. Failure times for each of the three specimens are marked on their respective deformation paths. Notice that the failures of the notched tensile bars are predicted reasonably well using the Monkman-Grant relationship and are within the scatter of the original data points (Figure 46).

Considering the fact that Norton's law and thus the constitutive equation used in this analysis neglects primary creep, the agreement of the predictions with the test results are very good.

9.2.4 Internal Variable Model

Having the minimum creep rate characterized is not sufficient as input for predicting the creep of structural components. The entire creep curve should be represented. The following approach was evaluated as an effective way to extend the minimum creep rate model (Equation 4) to the primary regime as well.

If we start with the assumption that the effect of stress and temperature on the minimum creep rate is representative of their effects on the entire creep curve then we can use an internal variable model which involves the dimensionless variable, s, and a material parameter, h. The change in structure will be represented by s, while h, is a measure of how quickly the material hardens. During creep, s evolves from its initial to final values. Here we will assume that we can normalize s such that its final value is unity. As s goes from s_o to 1 the creep rate will continuously decrease from its initial value until it reaches the temperature and stress dependent minimum value. This can be represented by the equations below.

$$\dot{\varepsilon}_{cr}=\frac{A_s}{s}\sigma^{n_s}e^{-Q_s/RT} \tag{10}$$

$$\dot{s}=h(1-s)\,\dot{\varepsilon}_{cr}. \tag{11}$$

Equations 10 and 11 represent a system of two, coupled first order differential equations that can be solved for $\varepsilon(t)$ to compare with experiments. The approach of using internal state variables is also being considered by Ding et. al.[14] for Si_3N_4 and has been used extensively in metals[18] to capture nonlinear material behavior.

In order to evaluate this new model, the creep tests were used of nine NCX-5101 joins that were tested until failure. The minimum creep rate parameters A_s, n_s and Q_s were determined from a least squares fit of the experimentally measured minimum creep rates. Using these values, the creep curves that were used in determining the parameters were simulated using Equations 10 and 11. The results are shown in Figure 52. The solid curves represent the experimental data and the dashed curves are the model predictions.

The results in Figure 52 show good agreement with the experiment. The shape and total strain are predicted reasonably well. In testing it

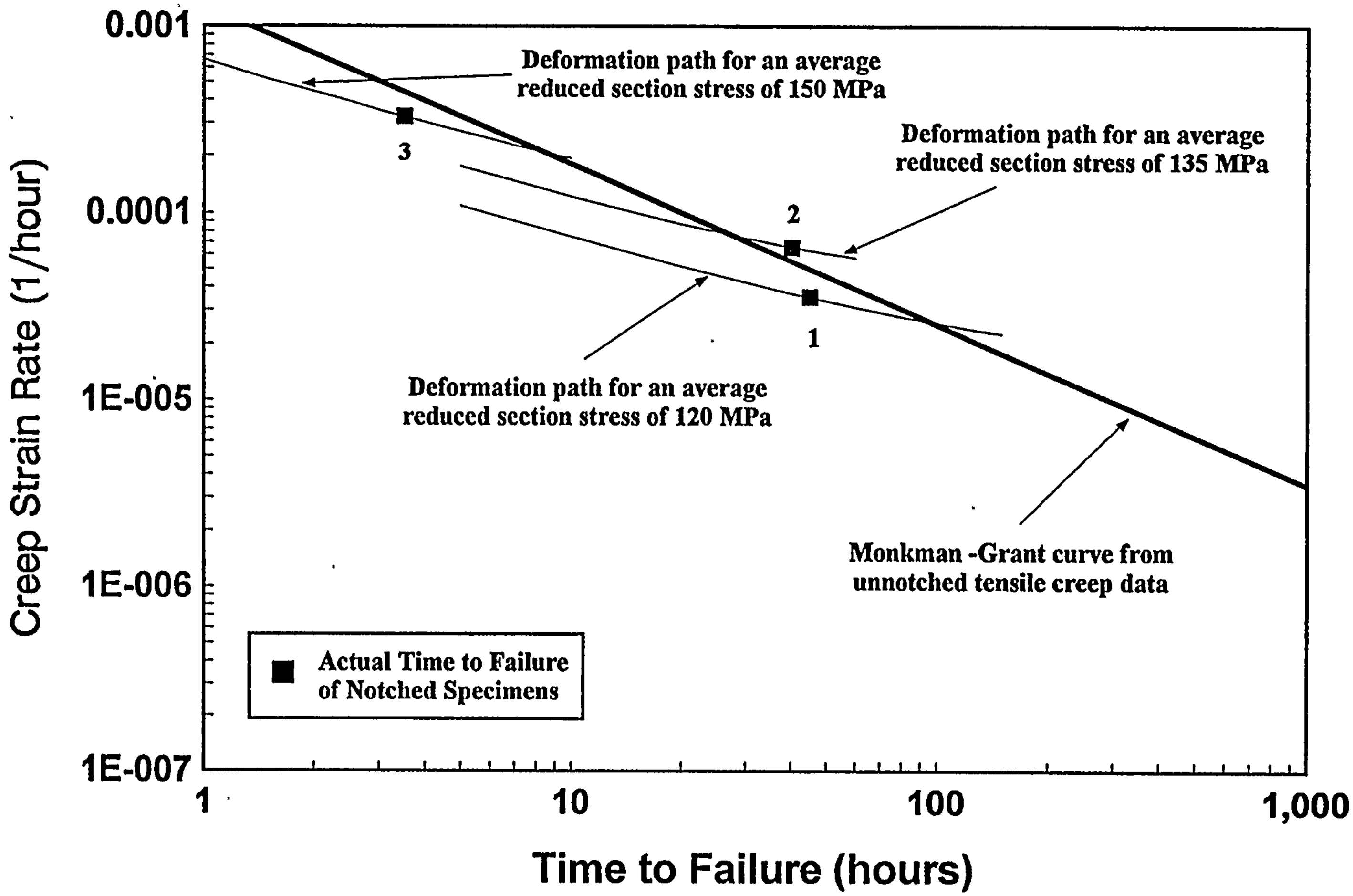

Figure 51: Failure Prediction of Cylindrical Gauge Notched Specimen Using the Monkman-Grant Relationship

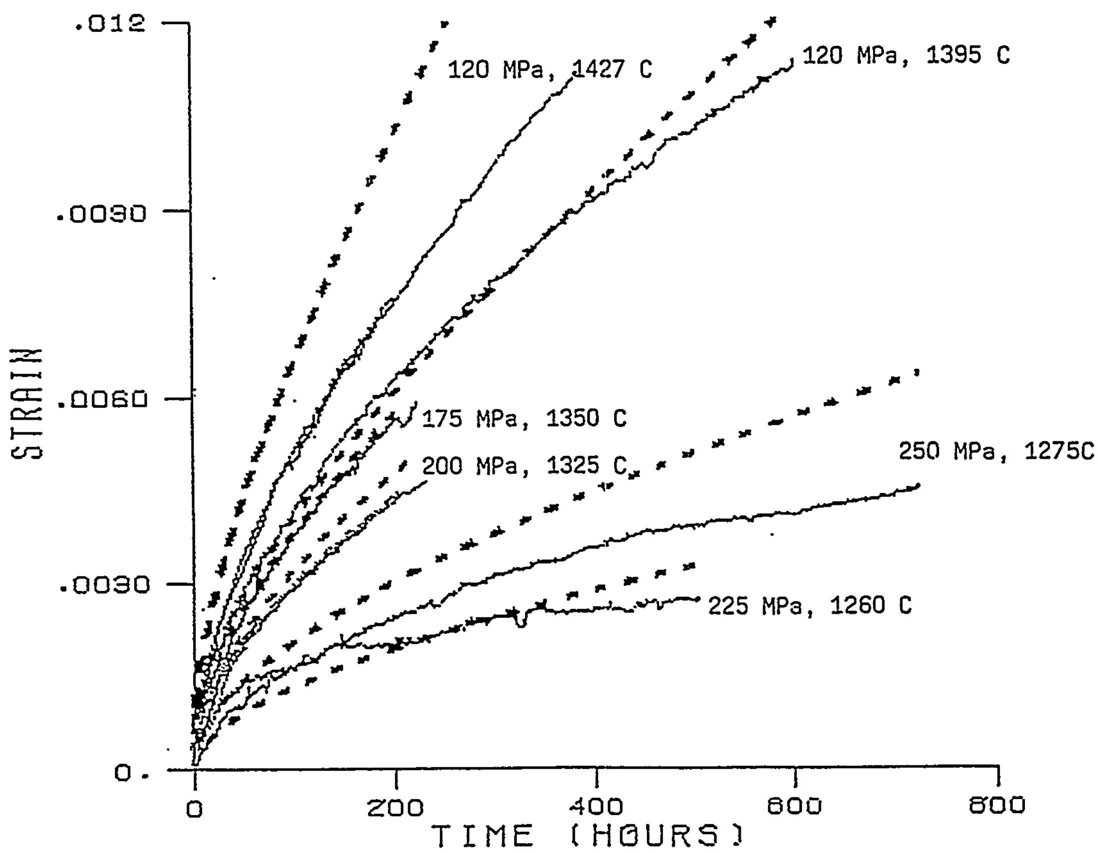

Figure 52: Comparison of Internal Variable Creep Model With Experiment for NCX-5101 Joined Specimens. Solid Curve is Experiment, Dashed Curve is Model.

was noticed that there is significant scatter in the measured creep response curves even for identical testing conditions. The model would not be able to capture this kind of experimental variability.

9.2.5 Theta Projection Method

The approach of using Norton's equation to model the quasi-steady state creep has received the most attention in the literature but is by no means the only creep model available. An attempt has been made by Evans and Wilshire[19, 20] to develop equations which adequately describe the shape of typical creep curves and also quantify how such curves depend upon stress and temperature. The time dependent creep strain can be described as a function of various shape terms, θ_i, which reproduce the creep curve at a specific stress and temperature:

$$\varepsilon_{cr}=\varepsilon_{cr}(t,\theta_1,\theta_2,\ldots,\theta_n) \qquad (12)$$

Different forms of Equation 12 have been used in the literature. The form which is used here can be understood as the sum of two terms. One term represents the decaying primary component and the other the accelerating tertiary component of creep strain, as follows:

$$\varepsilon_{cr}=\theta_1(1-e^{-\theta_2 t})+\theta_3(e^{\theta_4 t}-1) \qquad (13)$$

Here θ_1 and θ_3 are strain like components representing the magnitude of primary and tertiary creep. The θ_2 and θ_4 are parameters describing the rate of the controlling processes. The form of Equation 13 describes the shape of a creep curve for ductile metals quite well, but might not be expected to work as well for ceramics that lack a pronounced tertiary region. One goal here is to investigate that correspondence. Maximum likelihood fits were used to calculate the θ_i's for each experimental creep curve which had the units of hours for time. Interpolation between testing conditions is provided by representing the dependence of each θ_i on temperature and stress analytically:

$$\theta_i=\theta_i(T,\sigma) \qquad (14)$$

The curve fit that was used is a simple exponential factor expansion in stress and temperature:

$$\ln\theta_i=A_i+B_i\sigma+C_iT+D_i\sigma T \qquad (15)$$

for each θ_i, i=1,...,4. This curve fit reduces the experimental data base to a total of 16 constants. Evans et. al.[22] applied this "theta projection" method to different pressureless sintered silicon nitride ceramics produced using MgO, CeO_2, Y_2O_3 additives. The method showed reasonable temperature interpolation capabilities for design calculations involving continuously varying stress and temperature conditions.

The θ_i's have been determined for each specimen using Equation 13. These values are used to determine the constants of Equation 15 and are listed in Table 14. Units of MPa for stress and degrees Kelvin for temperature were used when calculating these coefficients.

Table 14: Theta Projection Coefficients

	A	B	C	D
θ1	-20.406	0.102	9.523E-03	-6.733E-05
θ2	43.095	-0.468	-3.034E-02	3.017E-04
θ3	-14.222	0.156	9.776E-03	-9.893E-05
θ4	-10.022	-0.340	-4.534E-03	2.319E-04

A comparison of the fit with an experimental creep curve at 1395°C and 120 MPa is shown in Figure 53. The primary creep portion of the experimental curve is matched very well by the model. However, the model can be seen to diverge from the experimental curve to represent a tertiary component which is anticipated in the second term of equation 13. The divergence occurs at the inflection point corresponding to the minimum strain rate given by:

$$\frac{d\varepsilon}{dt}=\theta_1\theta_2 e^{-\theta_2 t_m}+\theta_3\theta_4 e^{\theta_4 t_m} \tag{16}$$

where t_m is the time when the minimum creep rate occurs:

$$t_m=\frac{1}{\theta_2+\theta_4}\ln\frac{\theta_1\theta_2^2}{\theta_3\theta_4^2} \tag{17}$$

This inflection point occurs at 367 hours for the conditions of 1395°C at 120 MPa depicted in Figure 54.

In view of the fact that tertiary creep was not observed in this test program, the four parameter form of equation 13 is not useful in representing response beyond the primary creep region. While it adequately models the primary creep region, our main interest has been in characterizing the secondary creep region. This is the focus of the Norton law modeling discussed in section 9.2.1. In that approach, the emphasis is on developing a mechanistic understanding of the creep process specifically during the secondary creep regime where most engineering components operate for the majority of their design life.

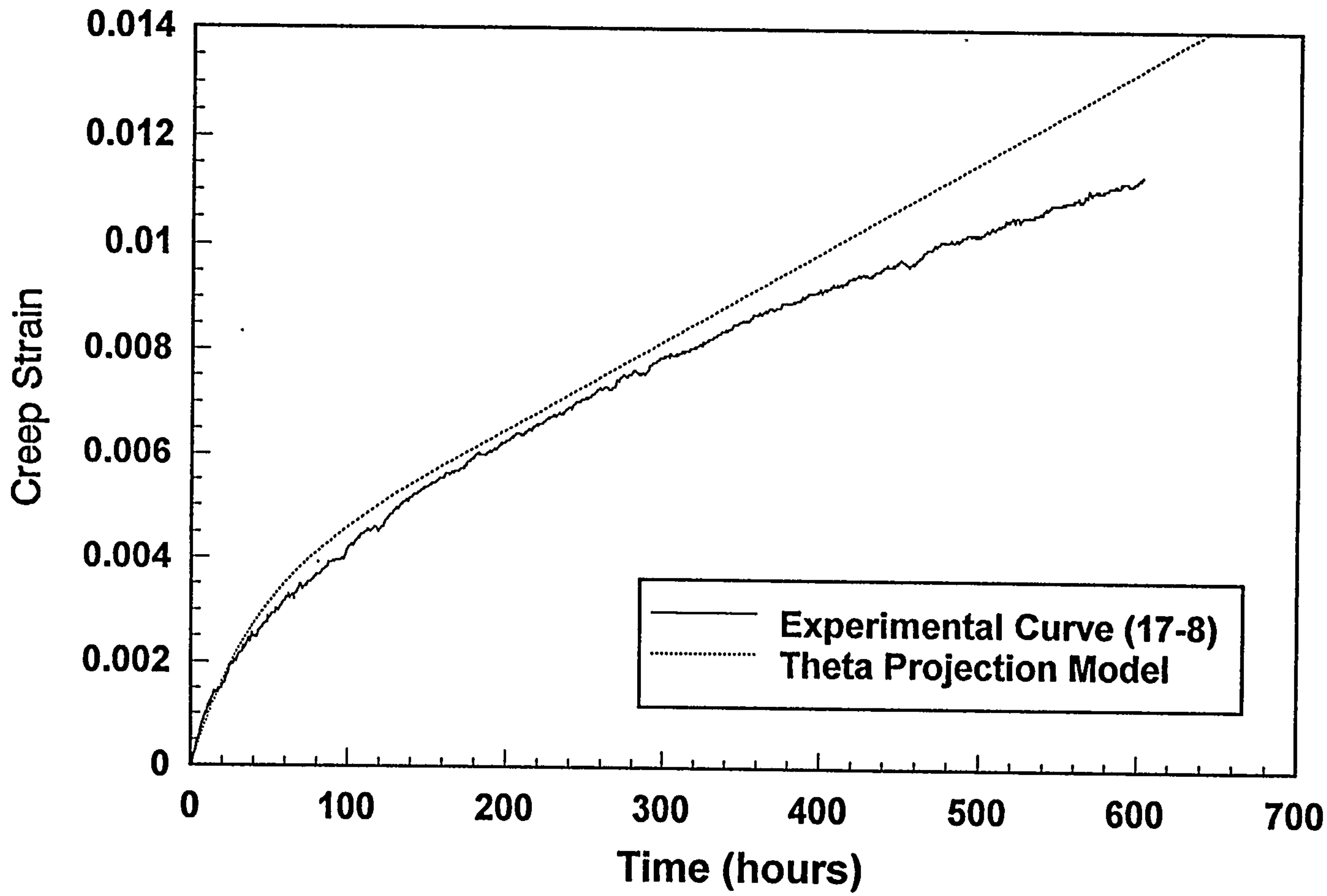

Figure 53: Theta Projection Versus Experimental Creep Curves at 1395°C and 120 MPa

10 CONCLUSIONS

The following conclusions may be drawn from the work performed under the Joining, Phase II contract.

Heat engine quality silicon nitride curved joins have been developed with similar properties to the planar butt joins developed under Joining, Phase I.

Green strength of the joining method was improved to minimize the handling rejections experienced before to hot isostatic pressing. Curved silicon nitride joins demonstrated a 5.5-fold improvement of pre-sintered green strength compared with methods used for Phase I of the contract.

Curved silicon nitride joins of 1.27 cm^2 area were developed with consistent, homogeneous properties across the join interlayer. There was no statistical difference between the 22°C and 1370°C flexure strength populations as a function of location within curved silicon nitride joins. The combined average 22°C flexure strength for curved silicon nitride joins was 886.3 MPa with a weibull modulus of 16.4 as determined by 156 flexure specimens from five curved join disks. The combined average 1370°C flexure strength for curved silicon nitride joins was 516 MPa with a weibull modulus of 16.0 as determined by 59 flexure specimens from five curved join disks. Only 1.2% of the 22°C flexure failures and 5.1% of the 1370°C flexure failures originated within the join interlayer. The excellent join integrity, characterized by the high strength of the join interlayer, prevented failure within the interlayer during shear tests of densified joins.

The demonstration of curved join quality similar to planar butt joins allowed application of the joining technique to more complex shapes, such as a simple rotor geometry. Shaft to disk joins made by the procedure developed for curved joins were ground to obtain spin test specimens.

Tensile strength of curved silicon nitride joins averaged 636 MPa with an estimated Weibull modulus of 8.2 with no failure originating from the join interlayer. The spin test specimens failed at angular velocities ranging between 17,000 and 42,530 revolutions per minute corresponding to a maximum principal stress from finite element analysis between 88.0 and 550.6 MPa. The angular velocity and stress at failure were less than predicted by the models developed within this contract due to failure origination at grinding damage. The size of surface flaws, determined by fractography, were consistent with the flaw size calculated from the Griffith relationship for brittle failure of solids. This result emphasizes the need for development of improved machining techniques for complex shaped structural ceramic components.

Tensile creep tests of the silicon nitride planar butt joins demonstrated behavior that was similar to the parent unjoined material. Creep was evaluated between temperature of 1250°C to 1420°C and stress between 100 and 250 MPa. Creep curves displayed a well defined primary creep regime with a gradual transition into secondary creep. None of the creep tests exhibited tertiary creep even though the duration of some tests were up to 1,692 hours. The largest variation of creep strain at test termination was observed within specimens as opposed to among specimens. The percent difference of total strain at test termination between opposing halves of the parent material typically ranged from 5% to 57%. This was attributed to inherent variable behavior of the ceramic parent material. Five of the 29 failures during tensile creep tests, originated within the join interlayer. Failed specimens exhibited cavitation at bi-grain junctions and wedge cracking at triple grain junctions. The creep data was incorporated into three models to develop a predictive tool that could be utilized for specimens of different geometry.

The widely accepted Norton's (or Arrhenius) equation approach was initially considered to model creep behavior. Values of activation energy (Q), stress exponent (n) and material constant (A) were determined for the creep experiments. An iterative procedure was used to determine a single estimate of these parameters for the entire creep matrix from which a good correlation of predicted and actual creep strain rate was obtained.

The above model used the minimum creep rate for a given experiment since this represented the creep rate at failure or test suspension within the secondary creep regime. Although this simplified the first attempt to model creep behavior, a more thorough treatment was later used where the entire creep curve, including the primary creep regime, was input in the model. The resultant internal variable model expressed the creep behavior by a system of two, coupled first order differential equations. Validation of the approach was obtained through comparison with the actual creep behavior of nine specimens that were tested to failure.

A less widely accepted, but interesting alternative to the Arrhenius equation approach, was considered to model the creep behavior. The theta projection method described time dependent creep strain with a series of shape terms to reproduce the creep strain curve at a specific stress and temperature. One term of the equation represented the decaying primary component and another an accelerating tertiary component of creep strain. The theta projection method deviated from classical creep modeling by defining the secondary creep regime mathematically as the resultant contribution of the tertiary and primary creep. Alternatively, the theta projection method provided a way not only to represent the experimental creep curves, but to interpolate to other testing conditions as well. However, the method did not satisfactorily fit all of the experimental data. The highly variable behavior within the primary creep regime experienced from specimen to specimen strongly contributed to an unacceptable error for predicted creep strain values. Additionally, the dependence of the theta projection model upon tertiary creep, which was not observed, invalidated use of this approach.

Creep failure modeling was facilitated by a correlation of creep strain rate with time to failure which allowed application of a Monkman-Grant relationship. It was unnecessary to plot separate curves for each temperature since a good correlation of all the experimental data was obtained with a single curve.

The development of material models, above, was useful only if the model could predict the performance of structural components. The refined models developed above were used to predict the behavior of a notched tensile specimen that served to simulate behavior of an actual component. Reasonable prediction of the time of failure for three specimens tested under different loads was an encouraging demonstration of the value of the use of ANSYS finite element code in conjunction with the Norton's law model.

NT230 silicon carbide joining of planar butt joins resulted with join quality affected by pronounced silicon enrichment and porosity. Additional trials used a total of six interlayer types consisting of various mixtures of silicon carbide and other additives applied to both siliconized and unsiliconized parent materials. Quality of the silicon carbide joins evaluated by room temperature flexure strength tests of specimens ground from the joined bodies showed all flexure specimens failed at the join interlayer. Join strength was lower than the strength of unjoined NT230 of similar cross sectional thickness, with average strengths of 152 MPa and 233 MPa respectively. Although, the joins were structurally sound and exhibited a improved, more homogeneous distribution of silicon carbide and silicon, all of the joins lacked a contiguous network of silicon carbide that extended into the parent material. All of the join methods resulted in join interlayers that were discrete relative to the parent materials and of higher silicon concentration. The distinct interface between the join interlayer and parent material consisted primarily of silicon within the join and silicon carbide within the parent material with an absence of interpenetration across the interface. In addition, voids within the join interlayer were strength limiting.

The silicon carbide join quality was deemed unsatisfactory for more demanding structural applications and, therefore, the decision was made not to proceed to more complex, curved geometries. The silicon carbide joining methods covered within this contract, although not entirely successful, have emphasized the need to focus future efforts upon ways to obtain a homogeneous, well sintered parent/join interface prior to siliconization. Improved definition of the silicon carbide joining problem obtained by efforts during this contract have provided avenues for future work that should successfully obtain heat engine quality joins.

11 ACKNOWLEDGEMENTS

The authors gratefully acknowledge the support of the Ceramic Technology Project, DOE Office of Transportation Technologies. We give special thanks for the guidance given by Mike Santella, Program Manager of Joining, at ORNL.

The authors wish to acknowledge the contributions of the following individuals for their steadfast support during this effort: D. Collette, R. D. Creehan, G. E. Lambert, M. J. Mangaudis, R. T. Rawson, T. M. Trostel, F. J. Wu, L. A. Broderick.

Special recognition is given to L. D. Ton for the manufacture of all joins, coordination of: furnacing, grinding and countless other tasks within the project.

Thanks to D. M. Tracey and R. H. Licht for editorial assistance.

The patience and perseverance of J. G. Gillam with secretarial efforts was invaluable.

The contribution of Norton Advanced Ceramics Division to the manufacture of parent materials is greatly appreciated.

12 REFERENCES

1. M. R. Foley, G. A. Rossi, G. J. Sundberg, J. A. Wade, F. J. Wu, *Analytical and Experimental Evaluation of Joining Silicon Carbide to Silicon Carbide and Silicon Nitride For Advanced Heat Engine Applications, Final Report, Subcontract 86X-SB045C,* Norton Company, September 30, 1991, **44**.

2. M. G. Jenkins, M. K. Ferber, et. al., *Study and Analysis of the Stress State in a Ceramic, Button-Head, Tensile Specimen*, ORNL TM-11767, September 1991.

3. Z-Mike Division of LaserMike Inc. (Formerly a Division of Zygo Corp.), Middlefield, CT, 06455-0448.

4. RS/1 is a trademark of BBN Software Products, 10 Fawcett Street, Cambridge, MA 02138.

5. T. R. Wilshaw, *"Measurement of Tensile Strength of Ceramics,"* Journal of The American Ceramic Society, February 1968, page 111.

6. Swanson Analysis Systems, Inc., ANSYS Rev. 4.4 and 5.0 Engineering Analysis System.

7. L. M. Powers, A. Starlinger, and J. P. Gyekenyesi, *"Ceramic Component Reliability With the Restructured NASA/Cares Computer Program,"* NASA Technical Memorandum 105856, 1992.

8. J. S. Cuccio, *"Life Prediction Methods for Ceramic Components of Advanced Vehicular Heat Engines,"* presented at ATDCCM, Dearborn, MI, October 18-21, 1993.

9. D. M. Tracey, *"3D Elastic Singularity Element for Evaluation of K Along an Arbitrary Crack Front,"* Int'l J. Fracture, **9**, pp.340-343, 1973.

10. H. E. Evans, *"Mechanisms of Creep Failure"* Elsevier Applied Science Publishers LTD., NY, 1984.

11. F. A. McClintock and A. S. Argon, *Mechanical Behavior of Materials*, Addison-Wesley Publishing Comp., Inc. (1966).

12. D. Chakraborty and A. K. Mukhopadhyay, *"Creep of Sintered Silicon Nitride,"* Ceramics International **15** (1989), 237-245.

13. F. H. Norton, *"The Creep of Steel at High Temperatures,"* McGraw-Hill, (1929).

14. J. L. Ding, K. C. Liu, and C. R. Brinkman, *"Development of a Constitutive Model for Creep and Life Prediction of Advanced Silicon Nitride Ceramics,"* Proceedings of the Annual Automotive Technology Development Contractors' Meeting, Dearborn, Michigan, Nov. 2-4, 1992, SAE, 583-592.

15. S. M. Wiederhorn, R. Krause and D. C. Cranmer, *"Tensile Creep Testing of Structural Ceramics,"* Proceedings of the Annual Automotive Technology Development Contractors' Meeting, Dearborn, Michigan, Oct. 28-31, 1991, SAE, 273-280.

16. Internal Saint-Gobain communication with R. L. Yeckley, 1993.

17. F. C. Monkman and N. J. Grant, *"An empirical Relationship Between Rupture Life and Minimum Creep Rate in Creep-Rupture Tests,"* Proc. Soc. Test. Mater. **56**, pp. 593-620 (1956).

18. S. B. Brown, K. H. Kim, and L. Anand, *An Internal Variable Constitutive Model for Hot Working of Metals*, International Journal of Plasticity, **Vol. 5**, pp. 95-13 (1985).

19. R. W. Evans, and B. Wilshire, *Creep of Metals and Alloys, The Institute of Metals*, London, 1985.

20. B. Wilshire and R. W. Evans, *Creep Behavior of Crystalline Solids, Progress in Creep and Fracture*, **Vol. 3**, Pineridge Press, Swansea, U.K., 1985.

21. R. W. Evans, T. Murakami, and B. Wilshire, *"The Generation of Long-Term Creep Data for Silicon Nitride Ceramics,"* British Ceramics Proceedings, **No. 39**, December 1987.

ORNL/Sub/87-SB045/2

INTERNAL DISTRIBUTION

Central Research Library (2)
Document Reference Section
Laboratory Records Department (2)
Laboratory Records, ORNL RC
ORNL Patent Section
M&C Records Office (3)
L. F. Allard, Jr.
L. D. Armstrong
D. L. Balltrip
R. L. Beatty
P. F. Becher
T. M. Besmann
P. J. Blau
E. E. Bloom
K. W. Boling
R. A. Bradley
C. R. Brinkman
V. R. Bullington
R. S. Carlsmith
P. T. Carlson
G. M. Caton
S. J. Chang
D. D. Conger
R. H. Cooper, Jr.
S. A. David
J. H. DeVan
J. L. Ding
M. K. Ferber
W. Fulkerson
R. L. Graves
D. L. Greene
H. W. Hayden, Jr.
E. E. Hoffman
C. R. Hubbard
M. A. Janney
D. R. Johnson (5)
F. W. Jones
R. R. Judkins
M. A. Karnitz
B. L. Keyes
H. D. Kimrey, Jr.
T. G. Kollie
K. C. Liu
E. L. Long, Jr.
W. D. Manly
R. W. McClung
D. J. McGuire
J. R. Merriman
T. A. Nolan
A. E. Pasto
M. H. Rawlins
J. L. Rich
C. R. Richmond
J M Robbins
G. V. Rogers, Jr.
M. L. Santella
A. C. Schaffhauser
S. Scott
E. J. Soderstrom
D. P. Stinton
R. W. Swindeman
M. C. Tate
V. J. Tennery
T. N. Tiegs
J. R. Weir, Jr.
B. H. West
S. G. Winslow
J. M. Wyrick
C. S. Yust

EXTERNAL DISTRIBUTION

Pioneering Research Info. Ctr.
E.I. Dupont de Nemours & Co. Inc.
Experimental Station
P.O. Box 80302
Wilmington DE 19880-0302

Jeffrey Abboud
U.S. Advanced Ceramics Assoc.
1600 Wilson Blvd., Suite 1008
Arlington VA 22209

James H. Adair
University of Florida
Materials Science & Engineering
317 MAE Bldg.
Gainesville FL 32611-2066

Donald F. Adams
University of Wyoming
Mechanical Engineering Department
P.O. Box 3295
Laramie WY 82071

Jalees Ahmad
AdTech Systems Research Inc.
Solid Mechanics
1342 N. Fairfield Road
Dayton OH 45432-2698

Yoshio Akimune
NISSAN Motor Co., Ltd.
Materials Research Laboratory
1 Natsushima-Cho
Yokosuka 237
JAPAN

Mufit Akinc
Iowa State University
322 Spedding Hall
Ames IA 50011

Ilhan A. Aksay
Princeton University
A313 Engineering Quadrangle
Princeton NJ 08544-5263

Richard L. Allor
Ford Motor Company
Materials Systems Reliability
P.O. Box 2053, Room S-2031
Dearborn MI 48121-2053

Joseph E. Amaral
Instron Corporation
Corporate Engineering Office
100 Royale Street
Canton MA 02021

Edward M. Anderson
Aluminum Company of America
N. American Industrial Chemical
P.O. Box 300
Bauxite AR 72011

Norman C. Anderson
Ceradyne, Inc.
Ceramic-to-Metal Division
3169 Redhill Avenue
Costa Mesa CA 92626

Don Anson
BCL
Thermal Power Systems
505 King Avenue
Columbus OH 43201-2693

Thomas Arbanas
G.B.C. Materials Corporation
580 Monastery Drive
Latrobe PA 15650-2698

Frank Armatis
3M Company
Building 60-1N-01
St. Paul MN 55144-1000

Everett B. Arnold
Detroit Diesel Corporation
Mechanical Systems Technology
13400 Outer Drive West
Detroit MI 48239-4001

Bertil Aronsson
Sandvik AB
S-12680
Stockholm Lerkrogsvagen 19
SWEDEN

Dennis Assanis
University of Illinois
Dept. of Mechanical Engineering
1206 W. Green Street
Urbana IL 61801

V. S. Avva
North Carolina A&T State Univ.
Dept. of Mechanical Engineering
Greensboro NC 27411

Patrick Badgley
Sky Technologies, Inc.
2815 Franklin Drive
Columbus IN 47201

Sunggi Baik
Pohang Institute of Sci. & Tech.
P.O. Box 125
Pohang 790-600
KOREA

John M. Bailey
Consultant
Caterpillar, Inc.
P.O. Box 1875
Peoria IL 61656-1875

Bob Baker
Ceradyne, Inc.
3169 Redhill Avenue
Costa Mesa CA 92626

Frank Baker
Aluminum Company of America
Alcoa Technical Center
Alcoa Center PA 15069

Clifford P. Ballard
AlliedSignal Aerospace Company
Ceramics Program
P.O. Box 1021
Morristown NJ 07962-1021

B. P. Bandyopadhyay
ELID Team
Wako Campus
2-1 Hirosawa Wako-shi
Saitama 351-01
JAPAN

P. M. Barnard
Ruston Gas Turbines Limited
P.O. Box 1
Lincoln LN2 5DJ
ENGLAND

Harold N. Barr
Hittman Corporation
9190 Red Branch Road
Columbia MD 21045

Renald D. Bartoe
Vesuvius McDanel
510 Ninth Avenue
Box 560
Beaver Falls PA 15010-0560

David L. Baty
Babcock & Wilcox - LRC
P.O. Box 11165
Lynchburg VA 24506-1165

Donald F. Baxter, Jr.
ASM International
Advanced Materials & Processes
Materials Park OH 44073-0002

M. Brad Beardsley
Caterpillar Inc.
Technical Center Bldg. E
P.O. Box 1875
Peoria IL 61656-1875

John C. Bell
Shell Research Limited
Thornton Research Centre
P.O. Box 1
Chester CH1 3SH
ENGLAND

M. Bentele
Xamag, Inc.
259 Melville Avenue
Fairfield CT 06430

Larry D. Bentsen
BFGoodrich Company
R&D Center
9921 Brecksville Road
Brecksville OH 44141

Louis Beregszazi
Defiance Precision Products
P.O. Drawer 428
Defiance OH 43512

Tom Bernecki
Northwestern University
1801 Maple Avenue
Evanston IL 60201-3135

Charles F. Bersch
Institute for Defense Analyses
1801 N. Beauregard Street
Alexandria VA 22311

Ram Bhatt
NASA Lewis Research Center
21000 Brookpark Road
Cleveland OH 44135

Deane I. Biehler
Caterpillar Inc.
Engineering Research Materials
P.O. Box 1875, Bldg. E
Peoria IL 61656-1875

John W. Bjerklie
Consolidated Natural Gas Service Co. Inc.
Research Department
Pittsburgh PA 15222-3199

William D. Bjorndahl
TRW, Inc.
One Space Park, MS:R6-2188
Building 01, Room 2040
Redondo Beach CA 90278

Keith A. Blakely
Advanced Refractory Technologies, Inc.
699 Hertel Avenue
Buffalo NY 14207

Edward G. Blanchard
Netzsch Inc.
119 Pickering Way
Exton PA 19341

Bruce Boardman
Deere and Company Technical Ctr.
3300 River Drive
Moline IL 61265

Hoechst Celanese Corporation
Short Hills NJ 07078

Russell Bockstedt
Hoechst Celanese Corporation
150 JFK Parkway
Short Hills NJ 07078

M. Boehmer
DLR German Aerospace Research Estab.
Postfach 90 60 58
D-5000 Koln 90
GERMANY

Lawrence P. Boesch
EER Systems Corp.
1593 Spring Hill Road
Vienna VA 22182-2239

Donald H. Boone
Boone & Associates
2412 Cascade Drive
Walnut Creek CA 94598-4313

Tom Booth
AlliedSignal, Inc.
AiResearch Los Angeles Division
2525 West 190th Street
Torrance CA 90509-2960

Tibor Bornemisza
Sundstrand Power Systems
4400 Ruffin Road
San Diego CA 92186-5757

J.A.M. Boulet
University of Tennessee
Engineering Science and Mechanics
Knoxville TN 37996-2030

H. Kent Bowen
Massachusetts Institute of Technology
77 Massachusetts Ave., Rm E40-434
Cambridge MA 02139

Leslie J. Bowen
Materials Systems
53 Hillcrest Road
Concord MA 01742

Steven C. Boyce
Air Force Office of Scientific Research
AFOSR/NA Bldg. 410
Bolling AFB DC 20332-6448

Gary L. Boyd
Ceramic Engineering Consulting
328 Sneath Way
Alpine CA 91901

Steve Bradley
UOP Research Center
50 E. Algonquin Road
Des Plaines IL 60017-6187

Michael C. Brands
Cummins Engine Company, Inc.
P.O. Box 3005, Mail Code 50179
Columbus IN 47201

Raymond J. Bratton
Westinghouse Science & Technology
1310 Beulah Road
Pittsburgh PA 15235

John J. Brennan
United Technologies Corporation
Silver Lane, MS:24
East Hartford CT 06108

Terrence K. Brog
Golden Technologies Company
4545 McIntyre Street
Golden CO 80403

Gunnar Broman
317 Fairlane Drive
Spartanburg SC 29302

Al Brown
High-Tech Materials Alert
P.O. Box 882
Dayton NJ 08810

Jesse J. Brown
VPI & SU
Ctr. for Advanced Ceram Materials
Blacksburg VA 24061-0256

Sherman D. Brown
University of Illinois
Materials Science and Engineering
105 South Goodwin Avenue
Urbana IL 61801

S. L. Bruner
Ceramatec, Inc.
2425 South 900 West
Salt Lake City UT 84119

Walter Bryzik
U.S. Army Tank Automotive Command
R&D Center, Propulsion Systems
Warren MI 48397-5000

S. J. Burden
2572 Devonwood
Troy MI 48098

Curt V. Burkland
AMERCOM, Inc.
8928 Fullbright Avenue
Chatsworth CA 91311

Bill Bustamante
AMERCOM, Inc.
8928 Fullbright Avenue
Chatsworth CA 91311

Oral Buyukozturk
Massachusetts Institute of Technology
77 Massachusetts Ave., Room 1-280
Cambridge MA 02139

David A. Caillet
Ethyl Corporation
451 Florida Street
Baton Rouge La 70801

Frederick J. Calnan
Heany Industries, Inc.
249 Briarwood Lane
Scottsville NY 14546

Roger Cannon
Rutgers University
P.O. Box 909
Piscataway NJ 08855-0909

Scott Cannon
P.O. Box 567254
Atlanta GA 30356

Harry W. Carpenter
1844 Fuerte Street
Fallbrook CA 92028

David Carruthers
Kyocera Industrial Ceramics
Company
P.O. Box 2279
Vancouver WA 98668-2279

Calvin H. Carter, Jr.
Cree Research, Inc.
2810 Meridian Parkway
Durham NC 27713

J. David Casey
35 Atlantis Street
West Roxbury MA 02132

Jere G. Castor
J. C. Enterprise
5078 N. 83rd Street
Scottsdale AZ 85250

James D. Cawley
Case Western Reserve University
Materials Science & Engineering
Cleveland OH 44106

Thomas C. Chadwick
Den-Mat Corporation
P.O. Box 1729
Santa Maria CA 93456

Ronald H. Chand
Chand Kare Technical Ceramics
2 Coppage Drive
Worcester MA 01603-1252

Robert E. Chaney
EG&G Idaho, Inc.
Idaho National Engineering Lab
P.O. Box 1625
Idaho Falls ID 83415-3525

Frank C. Chang
U.S. Army Materials Technology
AMTL-EMM
405 Arsenal Street
Watertown MA 02172

Nam S. Chang
Chrysler Corporation
12000 Chrysler Drive
Highland Park MI 48288-0001

William Chapman
Williams International Corp.
2280 W. Maple Road
Walled Lake MI 48390-0200

Ching-Fong Chen
LECO Corporation
3000 Lakeview Avenue
St. Joseph MI 49085

Frank Childs
EG&G Idaho, Inc.
Idaho National Engineering Lab
P.O. Box 1625
Idaho Falls ID 83415-3527

William J. Chmura
Torrington Company
59 Field Street
Torrington CT 06790-4942

Tsu-Wei Chou
University of Delaware
201 Spencer Laboratory
Newark DE 19716

R. J. Christopher
Ricardo Consulting Engineers
Bridge Works
Shoreham-By-Sea W. Sussex BN435FG
ENGLAND

Joel P. Clark
Massachusetts Institute of
Technology
Room 8-409
Cambridge MA 02139

Giorgio Clarotti
Commission of the European Comm
DGXII-C3, MO75, 1-53;
200 Rue de la Loi
B-1049 Brussels
BELGIUM

W. J. Clegg
ICI Advanced Materials
P.O. Box 11, The Heath
Runcorn Cheshire WA7 4QE
ENGLAND

Joseph Cleveland
GTE Products Corporation
Hawes Street
Towanda PA 18848-0504

William S. Coblenz
Adv. Research Projects Agency
3701 N. Fairfax Drive
Arlington VA 22203

Gloria M. Collins
ASTM
1916 Race Street
Philadelphia PA 19103

William C. Connors
Sundstrand Aviation Operations
Materials Science & Engineering
4747 Harrison Avenue
Rockford IL 61125-7002

John A. Coppola
Carborundum Company
Niagara Falls R&D Center
P.O. Box 832
Niagara Falls NY 14302

Normand D. Corbin
Norton Company
SGNICC/NRDC
Goddard Road
Northboro MA 01532-1545

Douglas Corey
AlliedSignal, Inc.
2525 West 190th Street, MS:T52
Torrance CA 90504-6099

Keith P. Costello
Chand/Kare Technical Ceramics
2 Coppage Drive
Worcester MA 01603-1252

Ed L. Courtright
Pacific Northwest Laboratory
MS:K3-59
Richland WA 99352

Anna Cox
Mitchell Market Reports
P.O. Box 23
Monmouth Gwent NP5 4YG
UNITED KINGDOM

J. Wesley Cox
BIRL
1801 Maple Avenue
Evanston IL 60201-3135

Art Cozens
Instron Corporation
3414 Snowden Avenue
Long Beach CA 90808

Mark Crawford
New Technology Week
4604 Monterey Drive
Annandale VA 22003

Richard A. Cree
Markets & Products, Inc.
P.O. Box 14328
Columbus OH 43214-0328

Les Crittenden
Vesuvius McDanel
Box 560
Beaver Falls PA 15010

William J. Croft
U.S. Army Materials Technology
405 Arsenal Street
Watertown MA 02172

M. J. Cronin
Mechanical Technology, Inc.
968 Albany-Shaker Road
Latham NY 12110

Gary M. Crosbie
Ford Motor Company
20000 Rotunda Drive
MD-2313, SRL Building
Dearborn MI 48121-2053

Floyd W. Crouse, Jr.
U.S. Department of Energy
Morgantown Energy Technology Ctr
P.O. Box 880
Morgantown WV 26505

John Cuccio
AlliedSignal Engines
P.O. Box 52180, MS:1302-2Q
Phoenix AZ 85072-2180

Raymond A. Cutler
Ceramatec, Inc.
2425 South 900 West
Salt Lake City UT 84119

Stephen C. Danforth
Rutgers University
P.O. Box 909
Piscataway NJ 08855-0909

Sankar Das Gupta
Electrofuel Manufacturing Co.
9 Hanna Avenue
Toronto Ontario MGK-1W8
CANADA

Frank Davis
AlliedSignal Aerospace Company
7550 Lucerne Drive, #203
Middleburg Heights OH 44130

Robert F. Davis
North Carolina State University
Materials Engineering Department
P.O. Box 7907
Raleigh NC 27695

Thomas DeAngelis
Carborundum Company
Niagara Falls R&D Center
P.O. Box 832
Niagara Falls NY 14302

Michael DeLuca
RSA Research Group
1534 Claas Ave.
Holbrook NY 11741

Gerald L. DePoorter
Colorado School of Mines
Metallurgical & Materials Engr
Golden CO 80401

J. F. DeRidder
Omni Electro Motive, Inc.
12 Seely Hill Road
Newfield NY 14867

Nick C. Dellow
Materials Technology Publications
40 Sotheron Road
Watford Herts WD1 2QA
UNITED KINGDOM

L. R. Dharani
University of Missouri-Rolla
224 M.E.
Rolla MO 65401

Douglas A. Dickerson
Union Carbide Specialty Powders
1555 Main Street
Indianapolis IN 46224

John Dodsworth
Vesuvius Research & Development
Technical Ceramics Group
Box 560
Beaver Falls PA 15010

B. Dogan
Institut fur Werkstofforschung
GKSS-Forschungszentrum Geesthacht
Max-Planck-Strasse
D-2054 Geesthacht
GERMANY

Alan Dragoo
U.S. Department of Energy
ER-131, MS:F-240
Washington DC 20817

Jean-Marie Drapier
FN Moteurs S.A.
Material and Processing
B-4041 Milmort (Herstal)
BELGIUM

Kenneth C. Dreitlein
United Technologies Research Ctr
Silver Lane
East Hartford CT 06108

Robin A.L. Drew
McGill University
3450 University Street
Montreal Quebec H3A 2A7
CANADA

Winston H. Duckworth
BCL
Columbus Division
505 King Avenue
Columbus OH 43201-2693

Bill Durako
Sundstrand Aviation Operations
P.O. Box 7002
Rockford IL 61125-7002

Ernest J. Duwell
3M Abrasive Systems Division
3M Center
St. Paul MN 55144-1000

Chuck J. Dziedzic
GTC Process Forming Systems
4545 McIntyre Street
Golden CO 80403

Robert J. Eagan
Sandia National Laboratories
Engineered Materials & Processes
P.O. Box 5800
Albuquerque NM 87185-5800

Jeffrey Eagleson
Lanxide Corporation
1001 Connecticut Avenue, N.W.
Washington DC 20036

Harry E. Eaton
United Technologies Corporation
Silver Lane
East Hartford CT 06108

Harvill C. Eaton
Louisiana State University
240 Thomas Boyd Hall
Baton Rouge LA 70803

Christopher A. Ebel
Carborundum Company
Technology Division
P.O. Box 832
Niagara Falls NY 14302-0832

J. J. Eberhardt
U.S. Department of Energy
Office of Transportation Matrl's
CE-34, Forrestal Building
Washington DC 20585

Jim Edler
Eaton Corporation
26201 Northwestern Highway
P.O. Box 766
Southfield MI 48037

G. A. Eisman
Dow Chemical Company
Ceramics and Advanced Materials
52 Building
Midland MI 48667

William A. Ellingson
Argonne National Laboratory
Energy Technology Division
9700 S. Cass Avenue
Argonne IL 60439

Anita Kaye M. Ellis
Machined Ceramics
629 N. Graham Street
Bowling Green KY 42101

Glen B. Engle
Nuclear & Aerospace Materials
16716 Martincoit Road
Poway CA 92064

Jeff Epstein
Ceramic Technologies, Inc.
12739 Ashford Knoll
Houston TX 77082

Kenneth A. Epstein
Dow Chemical Company
2030 Building
Midland MI 48674

Art Erdemir
Argonne National Laboratory
9700 S. Cass Avenue
Argonne IL 60439

E. M. Erwin
Lubrizol Corporation
1819 East 225th Street
Euclid OH 44117

John N. Eustis
U.S. Department of Energy
Industrial Energy Efficiency Div
CE-221, Forrestal Building
Washington DC 20585

W. L. Everitt
Kyocera International, Inc.
8611 Balboa Avenue
San Diego CA 92123

Gordon Q. Evison
332 S. Michigan Avenue
Suite 1730
Chicago IL 60604

John W. Fairbanks
U.S. Department of Energy
Office of Propulsion Systems
CE-322, Forrestal Building
Washington DC 20585

Tim Fawcett
Dow Chemical Company
Advanced Ceramics Laboratory
1776 Building
Midland MI 48674

Robert W. Fawley
Sundstrand Power Systems
Div. of Sundstrand Corporation
P.O. Box 85757
San Diego CA 92186-5757

John J. Fedorchak
GTE Products Corporation
Hawes Street
Towanda PA 18848-0504

Jeff T. Fenton
Vista Chemical Company
900 Threadneedle
Houston TX 77079

Larry Ferrell
Babcock & Wilcox
Old Forest Road
Lynchburg VA 24505

Raymond R. Fessler
BIRL
1801 Maple Avenue
Evanston IL 60201

Ross F. Firestone
Ross Firestone Company
188 Mary Street
Winnetka IL 60093-1520

Sharon L. Fletcher
Arthur D. Little, Inc.
15 Acorn Park
Cambridge MA 02140-2390

Thomas F. Foltz
Textron Specialty Materials
2 Industrial Avenue
Lowell MA 01851

Renee G. Ford
Materials and Processing Report
P.O. Box 72
Harrison NY 10528

John Formica
Supermaterials
2020 Lakeside Avenue
Cleveland OH 44114

Edwin Frame
Southwest Research Institute
P.O. Drawer 28510
San Antonio TX 78284

Armanet Francois
French Scientific Mission
4101 Reservoir Road, N.W.
Washington DC 20007-2176

R. G. Frank
Technology Assessment Group
10793 Bentley Pass Lane
Loveland OH 45140

David J. Franus
Forecast International
22 Commerce Road
Newtown CT 06470

Marc R. Freedman
NASA Lewis Research Center
21000 Brookpark Road, MS:49-3
Cleveland OH 44135

Douglas Freitag
Bayside Materials Technology
17 Rocky Glen Court
Brookeville MD 20833

Brian R.T. Frost
Argonne National Laboratory
9700 S. Cass Avenue, Bldg. 900
Argonne IL 60439

Lawrence R. Frost
Instron Corporation
100 Royall Street
Canton MA 02021

Xiren Fu
Shanghai Institute of Ceramics
1295 Ding-xi Road
Shanghai 200050
CHINA

J. P. Gallagher
University of Dayton Research Institute
300 College Park, JPC-250
Dayton OH 45469-0120

Garry Garvey
Golden Technologies Company Inc.
4545 McIntyre Street
Golden CO 80403

Richard Gates
NIST
Materials Bldg., A-256
Gaithersburg MD 20899

L. J. Gauckler
ETH-Zurich
Sonneggstrasse 5
CH-8092 Zurich 8092
SWITZERLAND

George E. Gazza
U.S. Army Materials Technology
Ceramics Research Division
405 Arsenal Street
Watertown MA 02172-0001

D. Gerster
CEA-DCOM
33 Rue De La Federation
Paris 75015
FRANCE

John Ghinazzi
Coors Technical Ceramics Company
1100 Commerce Park Drive
Oak Ridge TN 37830

Robert Giddings
General Electric Company
P.O. Box 8
Schenectady NY 12301

A. M. Glaeser
University of California
Lawrence Berkeley Laboratory
Hearst Mining Building
Berkeley CA 94720

Joseph W. Glatz
Naval Air Propulsion Center
Systems Engineering Division
510 Rocksville Road
Holland PA 18966

W. M. Goldberger
Superior Graphite Company
R&D
2175 E. Broad Street
Columbus OH 43209

Allan E. Goldman
U.S. Graphite, Inc.
907 W. Outer Drive
Oak Ridge TN 37830

Stephen T. Gonczy
Allied Signal Research
P.O. Box 5016
Des Plaines IL 60017

Jeffrey M. Gonzales
GTE Products Corporation
Hawes Street
Towanda PA 18848-0504

Robert J. Gottschall
U.S. Department of Energy
ER-131, MS:G-236
Washington DC 20585

Earl Graham
Cleveland State University
Dept. of Chemical Engineering
Euclid Avenue at East 24th Street
Cleveland OH 44115

John W. Graham
Astro Met, Inc.
9974 Springfield Pike
Cincinnati OH 45215

G. A. Graves
U. of Dayton Research Institute
300 College Park
Dayton OH 45469-0001

Robert E. Green, Jr.
Johns Hopkins University
Materials Science and Engineering
Baltimore MD 21218

Alex A. Greiner
Plint & Partners
Oaklands Park
Wokingham Berkshire RG11 2FD
UNITED KINGDOM

Lance Groseclose
General Motors Corporation
Allison Gas Turbine Division
P.O. Box 420, MS:W-5
Indianapolis IN 46206

Thomas J. Gross
U.S. Department of Energy
Transportation Technologies
CE-30, Forrestal Building
Washington DC 20585

Mark F. Gruninger
Union Carbide Corporation
Specialty Powder Business
1555 Main Street
Indianapolis IN 46224

Ernst Gugel
Cremer Forschungsinstitut
GmbH&Co.KG
Oeslauer Strasse 35
D-8633 Roedental 8633
GERMANY

John P. Gyekenyesi
NASA Lewis Research Center
21000 Brookpark Road, MS:6-1
Cleveland OH 44135

Nabil S. Hakim
Detroit Diesel Corporation
13400 Outer Drive West
Detroit MI 48239

Philip J. Haley
General Motors Corporation
P.O. Box 420, MS:T12A
Indianapolis IN 46236

Judith Hall
Fiber Materials, Inc.
Biddeford Industrial Park
5 Morin Street
Biddeford ME 04005

Y. Hamano
Kyocera Industrial Ceramics Corp.
5713 E. Fourth Plain Blvd.
Vancouver WA 98661-6857

Y. Harada
IIT Research Institute
10 West 35th Street
Chicago IL 60616

R. A. Harmon
25 Schalren Drive
Latham NY 12110

Norman H. Harris
Hughes Aircraft Company
P.O. Box 800520
Saugus CA 91380-0520

Alan M. Hart
Dow Chemical Company
1776 Building
Midland MI 48674

Pat E. Hart
Battelle Pacific Northwest Labs
Ceramics and Polymers Development
P.O. Box 999
Richland WA 99352

Michael H. Haselkorn
Caterpillar In.
Technical Center, Building E
P.O. Box 1875
Peoria IL 61656-1875

Debbie Haught
U.S. Department of Energy
Off. of Transportation Materials
EE-34, Forrestal Bldg.
Washington DC 20585

N. B. Havewala
Corning Inc.
SP-PR-11
Corning NY 14831

John Haygarth
Teledyne WAA Chang Albany
P.O. Box 460
Albany OR 97321

Norman L. Hecht
U. of Dayton Research Institute
300 College Park
Dayton OH 45469-0172

Peter W. Heitman
General Motors Corporation
P.O. Box 420, MS:W-5
Indianapolis IN 46206-0420

Robert W. Hendricks
VPI & SU
210 Holden Hall
Blacksburg VA 24061-0237

Thomas L. Henson
GTE Products Corporation
Chemical & Metallurgical Division
Hawes Street
Towanda PA 18848

Thomas P. Herbell
NASA Lewis Research Center
21000 Brookpark Road, MS:49-3
Cleveland OH 44135

Marlene Heroux
Rolls-Royce, Inc.
2849 Paces Ferry Road, Suite 450
Atlanta GA 30339-3769

Robert L. Hershey
Science Management Corporation
1255 New Hampshire Ave., N.W.
Suite 1033
Washington DC 20036

Hendrik Heystek
Bureau of Mines
Tuscaloosa Research Center
P.O. Box L
University AL 35486

Robert V. Hillery
GE Aircraft Engines
One Neumann Way, M.D. H85
Cincinnati OH 45215

Arthur Hindman
Instron Corporation
100 Royall Street
Canton MA 02021

Hans Erich Hintermann
CSEM
Rue Breguet 2
Neuchatel 2000
SWITZERLAND

Shinichi Hirano
Mazda R&D of North America, Inc.
1203 Woodridge Avenue
Ann Arbor MI 48105

Tommy Hiraoka
NGK Locke, Inc.
1000 Town Center
Southfield MI 48075

Fu H. Ho
General Atomics
P.O. Box 85608
San Diego CA 92186-9784

John M. Hobday
U.S. Department of Energy
Morgantown Energy Technology Ctr
P.O. Box 880
Morgantown WV 26507

Clarence Hoenig
Lawrence Livermore National Lab
P.O. Box 808, Mail Code L-369
Livermore CA 94550

Thomas Hollstein
Fraunhofer-Institut fur
Werkstoffmechanik
Wohlerstrasse 11
79108 Freiburg
GERMANY

Richard Holt
National Research Council Canada
Structures and Materials Lab
Ottawa Ontario K1A OR6
CANADA

Woodie Howe
Coors Technical Ceramics Company
1100 Commerce Park Drive
Oak Ridge TN 37830

Stephen M. Hsu
NIST
Gaithersburg MD 20899

Hann S. Huang
Argonne National Laboratory
9700 S. Cass Avenue
Argonne IL 60439-4815

Gene Huber
Precision Ferrites & Ceramics
5576 Corporate Drive
Cypress CA 90630

Harold A. Huckins
Princeton Advanced Technology
4 Bertram Place
Hilton Head SC 29928

Fred R. Huettic
Advanced Magnetics Inc.
45 Corey Lane
Mendham NJ 07945

Brian K. Humphrey
Lubrizol Petroleum Chemicals Co.
3000 Town Center, Suite 1340
Southfield MI 48075-1201

Robert M. Humrick
Dylon Ceramic Technologies
3100 Edgehill Road
Cleveland Heights OH 44118

Lorretta Inglehart
National Science Foundation
Division of Materials Research
1800 "G" Street, N.W., Room 408
Washington DC 20550

Michael S. Inoue
Kyocera International, Inc.
8611 Balboa Avenue
San Diego CA 92123-1580

Joseph C. Jackson
U.S. Advanced Ceramics Assoc.
1600 Wilson Blvd., Suite 1008
Arlington VA 22209

Osama Jadaan
U. of Wisconsin-Platteville
1 University Plaza
Platteville WI 53818

Said Jahanmir
NIST
Materials Bldg., Room A-237
Gaithersburg MD 20899

Curtis A. Johnson
General Electric Company
P.O. Box 8
Schenectady NY 12301

Sylvia Johnson
SRI International
333 Ravenswood Avenue
Menlo Park CA 94025

Thomas A. Johnson
Lanxide Corporation
P.O. Box 6077
Newark DE 19714-6077

W. S. Johnson
Indiana University
One City Centre, Suite 200
Bloomington IN 47405

Walter F. Jones
AFOSR/NA
110 Duncan Ave., Ste. B115
Washington DC 20332-0001

Jill E. Jonkouski
U.S. Department of Energy
9800 S. Cass Avenue
Argonne IL 60439-4899

L. A. Joo
Great Lakes Research Corporation
P.O. Box 1031
Elizabethton TN 37643

A. David Joseph
SPX Corporation
700 Terrace Point
Muskegon MI 49443

Adam Jostsons
Australian Nuclear Science &
Technology
New Illawarra Road
Lucas Heightss New South Wales
AUSTRALIA

Matthew K. Juneau
Ethyl Corporation
451 Florida Street
Baton Rouge LA 70801

Tom Kalamasz
Norton/TRW Ceramics
7A-4 Raymond Avenue
Salem NH 03079

Lyle R. Kallenbach
Phillips Petroleum
Mail Drop:123AL
Bartlesville OK 74004

Nick Kamiya
Kyocera Industrial Ceramics Corp.
25 Northwest Point Blvd., #450
Elk Grove Village IL 60007

Roy Kamo
Adiabatics, Inc.
3385 Commerce Park Drive
Columbus IN 47201

Chih-Chun Kao
Industrial Technology Research
Institute
195 Chung-Hsing Road, Sec. 4
Chutung Hsinchu 31015 R.O.C.
TAIWAN

Keith R. Karasek
AlliedSignal Aerospace Company
50 E. Algonquin Road
Des Plaines IL 60017-5016

Martha R. Kass
U.S. Department of Energy
Oak Ridge Operations
Building 4500N, MS:6269
Oak Ridge TN 37831-6269

Robert E. Kassel
Ceradyne, Inc.
3169 Redhill Avenue
Costa Mesa CA 92626

Allan Katz
Wright Laboratory
Metals and Ceramics Division
Wright-Patterson AFB OH 45433

R. Nathan Katz
Worcester Polytechnic Institute
100 Institute Road
Worcester MA 01609

Tony Kaushal
Detroit Diesel Corporation
13400 Outer Drive, West
Detroit MI 48239-4001

Ted Kawaguchi
Tokai Carbon America, Inc.
375 Park Avenue, Suite 3802
New York NY 10152

Noritsugu Kawashima
TOSHIBA Corporation
4-1 Ukishima-Cho
Kawasaki-Ku Kawasaki 210
JAPAN

Lisa Kempfer
Penton Publishing
1100 Superior Avenue
Cleveland OH 44114-2543

Frederick L. Kennard, III
AC Rochester
1300 N. Dort Highway
Flint MI 48556

David O. Kennedy
Lester B. Knight Cast Metals Inc.
549 W. Randolph Street
Chicago IL 60661

George Keros
Photon Physics
3175 Penobscot Building
Detroit MI 48226

Thomas Ketcham
Corning, Inc.
SP-DV-1-9
Corning NY 14831

Pramod K. Khandelwal
General Motors Corporation
Allison Gas Turbine Division
P.O. Box 420, MS:W05
Indianapolis IN 46206

Jim R. Kidwell
AlliedSignal Engines
P.O. Box 52180
Phoenix AZ 85072-2180

Shin Kim
The E-Land Group
19-8 ChangJeon-dong
Mapo-gu, Seoul 121-190
KOREA

W. C. King
Mack Truck, Z-41
1999 Pennsylvania Avneue
Hagerstown MD 21740

Carol Kirkpatrick
MSE, Inc.
P.O. Box 3767
Butte MT 59702

Tony Kirn
Caterpillar Inc.
Defense Products Department, JB7
Peoria IL 61629

James D. Kiser
NASA Lewis Research Center
21000 Brookpark Road, MS:49-3
Cleveland OH 44135

Max Klein
900 24th Street, N.W., Unit G
Washington DC 20037

Richard N. Kleiner
Golden Technologies Company
4545 McIntyre Street
Golden CO 80403

Stanley J. Klima
NASA Lewis Research Center
21000 Brookpark Road, MS:6-1
Cleveland OH 44135

Albert S. Kobayashi
University of Washington
Mechanical Engineering Department
Mail Stop:FU10
Seattle WA 98195

Shigeki Kobayashi
Toyota Central Research Labs
Nagakute Aichi 480-11
JAPAN

Richard A. Kole
Z-Tech Corporation
8 Dow Road
Bow NH 03304

Joseph A. Kovach
Eaton Corporation
32500 Chardon Road
Willoughby Hills OH 44094

Kenneth A. Kovaly
Technical Insights Inc.
P.O. Box 1304
Fort Lee NJ 07024-9967

Ralph G. Kraft
Spraying Systems Company
North Avenue at Schmale Road
Wheaton IL 60189-7900

Arthur Kranish
Trends Publishing Inc.
1079 National Press Building
Washington DC 20045

A. S. Krieger
Radiation Science, Inc.
P.O. Box 293
Belmont MA 02178

Pieter Krijgsman
Ceramic Design International
Holding B.V.
P.O. Box 68
Hattem 8050-AB
THE NETHERLANDS

Waltraud M. Kriven
University of Illinois
105 S. Goodwin Avenue
Urbana IL 61801

Edward J. Kubel, Jr.
ASM International
Advanced Materials & Processes
Materials Park OH 44073

Dave Kupperman
Argonne National Laboratory
9700 S. Cass Avenue
Argonne IL 60439

Oh-Hun Kwon
North Company
SGNICC/NRDC
Goddard Road
Northboro MA 01532-1545

W. J. Lackey
GTRI
Materials Science and Tech. Lab
Atlanta GA 30332

Jai Lala
Tenmat Ltd.
40 Somers Road
Rugby Warwickshire CV22 7DH
ENGLAND

Hari S. Lamba
General Motors Corporation
9301 West 55th Street
LaGrange IL 60525

Richard L. Landingham
Lawrence Livermore National Lab
P.O. Box 808, L-369
Livermore CA 94550

James Lankford
Southwest Research Institute
6220 Culebra Road
San Antonio TX 78228-0510

Stanley B. Lasday
Business News Publishing Co.
1910 Cochran Road, Suite 630
Pittsburgh PA 15220

S. K. Lau
Carborundum Company
Technology Division
P.O. Box 832, B-100
Niagara Falls NY 14302

J. Lawrence Lauderdale
Babcock & Wilcox
1850 "K" Street, Suite 950
Washington DC 20006

Jean F. LeCostaouec
Textron Specialty Materials
2 Industrial Avenue
Lowell MA 01851

Benson P. Lee
Technology Management, Inc.
4440 Warrensville Rd., Suite A
Cleveland OH 44128

Burtrand I. Lee
Clemson University
Olin Hall
Clemson SC 29634-0907

June-Gunn Lee
KIST
P.O. Box 131, Cheong-Ryang
Seoul 130-650
KOREA

Ran-Rong Lee
Ceramics Process Systems
Corporation
155 Fortune Boulevard
Mildford MA 01757

Stan Levine
NASA Lewis Research Center
21000 Brookpark Road, MS:49-3
Cleveland OH 44135

David Lewis, III
Naval Research Laboratory
Code 6370
Washington DC 20375-5343

Ai-Kang Li
Materials Research Labs., ITRI
195-5 Chung-Hsing Road, Sec. 4
Chutung Hsinchu 31015 R.O.C.
TAIWAN

Winston W. Liang
Hong Kong Industrial Technology
Centre
78 Tat Chee Avenue
4/F, HKPC Building -- Kowloon
HONG KONG

Robert Licht
Norton Company
SGNICC/NRDC
Goddard Road
Northboro MA 01532-1545

E. Lilley
Norton Company
SGNICC/NRDC
Goddard Road
Northboro MA 01532-1545

Chih-Kuang Lin
National Central University
Dept. of Mechanical Engineering
Chung-Li 32054
TAIWAN

Laura J. Lindberg
AlliedSignal Aerospace Company
Garrett Fluid Systems Division
P.O. Box 22200
Tempe AZ 85284-2200

Hans A. Lindner
Cremer Forschungsinstitut
GmbH&Co.KG
Oeslauer Strasse 35
D-8633 Rodental 8866
GERMANY

Ronald E. Loehman
Sandia National Laboratories
Chemistry & Ceramics Dept. 1840
P.O. Box 5800
Albuquerque NM 87185

Jeffrey C. Logas
Winona State University
115 Pasteur Hall
Winona MN 55987

Bill Long
Babcock & Wilcox
P.O. Box 11165
Lynchburg VA 24506

L. A. Lott
EG&G Idaho, Inc.
Idaho National Engineering Lab
P.O. Box 1625
Idaho Falls ID 83415-2209

Raouf O. Loutfy
MER Corporation
7960 S. Kolb Road
Tucson AZ 85706

Gordon R. Love
Aluminum Company of America
Alcoa Technical Center
Alcoa Center PA 15960

Lydia Luckevich
Ortech International
2395 Speakman Drive
Mississauga Ontario L5K 1B3
CANADA

James W. MacBeth
Carborundum Company
Structural Ceramics Division
P.O. Box 1054
Niagara Falls NY 14302

George Maczura
Aluminum Company of America
3450 Park Lane Drive
Pittsburgh PA 15275-1119

David Maginnis
Tinker AFB
OC-ALC/LIIRE
Tinker AFB OK 73145-5989

Frank Maginnis
Aspen Research, Inc.
220 Industrial Boulevard
Moore OK 73160

Tai-il Mah
Universal Energy Systems, Inc.
4401 Dayton-Xenia Road
Dayton OH 45432

Kenneth M. Maillar
Barbour Stockwell Company
83 Linskey Way
Cambridge MA 02142

S. G. Malghan
NIST
I-270 & Clopper Road
Gaithersburg MD 20899

Lars Malmrup
United Turbine AB
Box 13027
Malmo S-200 44
SWEDEN

John Mangels
Ceradyne, Inc.
3169 Redhill Avenue
Costa Mesa CA 92626

Murli Manghnani
University of Hawaii
2525 Correa Road
Honolulu HI 96822

Russell V. Mann
Matec Applied Sciences, Inc.
75 South Street
Hopkinton MA 01748

William R. Manning
Champion Aviation Products Div
P.O. Box 686
Liberty SC 29657

Ken Marnoch
Amercom, Inc.
8928 Fullbright Avenue
Chatsworth CA 91311

Robert A. Marra
Aluminum Company of America
Alcoa Technical Center
Alcoa Center PA 15069

Chauncey L. Martin
3M Company
3M Center, Building 60-1N-01
St. Paul MN 55144

Steve C. Martin
Advanced Refractory Technologies
699 Hertel Avenue
Buffalo NY 14207

Kelly J. Mather
William International Corporation
2280 W. Maple Road
Walled Lake MI 48088

James P. Mathers
3M Company
3M Center, Bldg. 201-3N-06
St. Paul MN 55144

Ron Mayville
Arthur D. Little, Inc.
15-163 Acorn Park
Cambridge MA 02140

F. N. Mazadarany
General Electric Company
Bldg. K-1, Room MB-159
P.O. Box 8
Schenectady NY 12301

James W. McCauley
Alfred University
Binns-Merrill Hall
Alfred NY 14802

Louis R. McCreight
2763 San Ramon Drive
Rancho Palos Verdes CA 90274

Colin F. McDonald
McDonald Thermal Engineering
1730 Castellana Road
La Jolla CA 92037

B. J. McEntire
Norton Company
10 Airport Park Road
East Granby CT 06026

Chuck McFadden
Coors Ceramics Company
600 9th Street
Golden CO 80401

Thomas D. McGee
Iowa State University
110 Engineering Annex
Ames IA 50011

Carol McGill
Corning Inc.
Sullivan Park, FR-02-08
Corning NY 14831

James McLaughlin
Sundstrand Power Systems
4400 Ruffin Road
P.O. Box 85757
San Diego CA 92186-5757

Matt McMonigle
U.S. Department of Energy
Improved Energy Productivity
CE-231, Forrestal Building
Washington DC 20585

J. C. McVickers
AlliedSignal Engines
P.O. Box 52180, MS:9317-2
Phoenix AZ 85072-2180

D. B. Meadowcroft
"Jura," The Ridgeway
Oxshott
Leatherhead Surrey KT22 OLG
UNITED KINGDOM

Joseph J. Meindl
Reynolds International, Inc.
6603 W. Broad Street
P.O. Box 27002
Richmond VA 23261-7003

Michael D. Meiser
AlliedSignal, Inc.
Ceramic Components
P.O. Box 2960, MS:T21
Torrance CA 90509-2960

George Messenger
National Research Council of
Canada
Building M-7
Ottawa Ontario K1A OR6
CANADA

D. Messier
U.S. Army Materials Technology
SLCMT-EMC
405 Arsenal Street
Watertown MA 02172-0001

Arthur G. Metcalfe
Arthur G. Metcalfe and
Associates, Inc.
2108 East 24th Street
National City CA 91950

R. Metselaar
Eindhoven University
P.O. Box 513
Endhoven 5600 MB
THE NETHERLANDS

David J. Michael
Harbison-Walker Refractories Co.
P.O. Box 98037
Pittsburgh PA 15227

Ken Michaels
Chrysler Motors Corporation
P.O. Box 1118, CIMS:418-17-09
Detroit MI 48288

Bernd Michel
Institute of Mechanics
P.O. Box 408
D-9010 Chemnitz
GERMANY

D. E. Miles
Commission of the European Comm.
rue de la Loi 200
B-1049 Brussels
BELGIUM

Carl E. Miller
AC Rochester
1300 N. Dort Highway, MS:32-31
Flint MI 48556

Charles W. Miller, Jr.
Centorr Furnaces/Vacuum
Industries
542 Amherst Street
Nashua NH 03063

R. Minimmi
Enichem America
2000 Cornwall Road
Monmouth Junction NJ 08852

Michele V. Mitchell
AlliedSignal, Inc.
Ceramic Components
P.O. Box 2960, MS:T21
Torrance CA 90509-2960

Howard Mizuhara
WESGO
477 Harbor Boulevard
Belmont CA 94002

Helen Moeller
Babcock & Wilcox
P.O. Box 11165
Lynchburg VA 24506-1165

Francois R. Mollard
Concurrent Technologies Corp.
1450 Scalp Avenue
Johnstown PA 15904-3374

Phil Mooney
Panametrics
221 Crescent Street
Waltham MA 02254

Geoffrey P. Morris
3M Company
3M Traffic Control Materials
Bldg. 209-BW-10, 3M Center
St. Paul MN 55144-1000

Jay A. Morrison
Rolls-Royce, Inc.
2849 Paces Ferry Road, Suite 450
Atlanta GA 30339-3769

Joel P. Moskowitz
Ceradyne, Inc.
3169 Redhill Avenue
Costa Mesa CA 92626

Brij Moudgil
University of Florida
Material Science & Engineering
Gainesville FL 32611

Christoph J. Mueller
Sprechsaal Publishing Group
P.O. Box 2962, Mauer 2
D-8630 Coburg
GERMANY

Thomas W. Mullan
Vapor Technologies Inc.
345 Route 17 South
Upper Saddle River NJ 07458

Theresa A. Mursick-Meyer
Norton Company
SGNICC/NRDC
Goddard Road
Northboro MA 01532-1545

M. K. Murthy
MkM Consultants International
10 Avoca Avenue, Unit 1906
Toronto Onntario M4T 2B7
CANADA

David L. Mustoe
Custom Technical Ceramics
8041 West I-70 Service Rd. Unit 6
Arvada CO 80002

Curtis V. Nakaishi
U.S. Department of Energy
Morgantown Energy Technology Ctr.
P.O. Box 880
Morgantown WV 26507-0880

Yoshio Nakamura
Faicera Research Institute
3-11-12 Misono
Sagamihara, Tokyo
JAPAN

Stefan Nann
Roland Berger & Partner GmbH
Georg-Glock-Str. 3
40474 Dusseldorf
GERMANY

K. S. Narasimhan
Hoeganaes Corporation
River Road
Riverton NJ 08077

Robert Naum
Applied Resources, Inc.
P.O. Box 241
Pittsford NY 14534

Malcolm Naylor
Cummins Engine Company, Inc.
P.O. Box 3005, Mail Code 50183
Columbus IN 47202-3005

Fred A. Nichols
Argonne National Laboratory
9700 S. Cass Avenue
Argonne IL 60439

H. Nickel
Forschungszentrum Juelich (KFA)
Postfach 1913
D-52425 Juelich
GERMANY

Dale E. Niesz
Rutgers University
Center for Ceramic Research
P.O. Box 909
Piscataway NJ 08855-0909

Paul W. Niskanen
Lanxide Corporation
P.O. Box 6077
Newark DE 19714-6077

David M. Nissley
United Technologies Corporation
Pratt & Whitney Aircraft
400 Main Street, MS:163-10
East Hartford CT 06108

Bruce E. Novich
Ceramics Process Systems Corp.
155 Fortune Boulevard
Milford MA 01757

Daniel Oblas
50 Meadowbrook Drive
Bedford MA 01730

Don Ohanehi
Magnetic Bearings, Inc.
1908 Sussex Road
Blacksburg VA 24060

Hitoshi Ohmori
ELID Team
Itabashi Branch
1-7 13 Kaga Itabashi
Tokyo 173
JAPAN

Robert Orenstein
General Electric Company
55-112, River Road
Schenectady NY 12345

Norb Osborn
Aerodyne Dallas
151 Regal Row, Suite 120
Dallas TX 75247

Richard Palicka
Cercom, Inc.
1960 Watson Way
Vista CA 92083

Muktesh Paliwal
GTE Products Corporation
Hawes Street
Towanda PA 18848

Joseph N. Panzarino
Norton Company
SGNICC/NRDC
Goddard Road
Northboro MA 01532-1545

Pellegrino Papa
Corning Inc.
MP-WX-02-1
Corning NY 14831

Terry Paquet
Boride Products Inc.
2879 Aero Park Drive
Traverse City MI 49684

E. Beth Pardue
MPC
8297 Williams Ferry Road
Lenior City TN 37771

Soon C. Park
3M Company
Building 142-4N-02
P.O. Box 2963
St. Paul MN 55144

Vijay M. Parthasarathy
Caterpillar/Solar Turbines
2200 Pacific Highway
P.O. Box 85376
San Diego CA 92186-5376

Harmut Paschke
Schott Glaswerke
Christoph-Dorner-Strasse 29
D-8300 Landshut
GERMANY

James W. Patten
Cummins Engine Company, Inc.
P.O. Box 3005, Mail Code 50183
Columbus IN 47202-3005

Robert A. Penty
Eastman Kodak Company
Kodak Park
Bldg., 326, 3rd Floor
Rochester NY 14652-5120

Robert W. Pepper
Textron Specialty Materials
2 Industrial Avenue
Lowell MA 01851

Peter Perdue
Detroit Diesel Corporation
13400 Outer Drive West,
Speed Code L-04
Detroit MI 48239-4001

John J. Petrovic
Los Alamos National Laboratory
Group MST-4, MS:G771
Los Alamos NM 87545

Frederick S. Pettit
University of Pittsburgh
Pittsburgh PA 15261

Ben A. Phillips
Phillips Engineering Company
721 Pleasant Street
St. Joseph MI 49085

Richard C. Phoenix
Ohmtek, Inc.
2160 Liberty Drive
Niagara Falls NY 14302

Bruce J. Pletka
Michigan Technological University
Metallurgical & Materials Engr.
Houghton MI 49931

John P. Pollinger
AlliedSignal, Inc.
Ceramic Components
P.O. Box 2960, MS:T21
Torrance CA 90509-2960

P. Popper
High Tech Ceramics International
Journal
22 Pembroke Drive - Westlands
Newcastle-under-Lyme
Staffs ST5 2JN
ENGLAND

F. Porz
Universitat Karlsruhe
Institut fur Keramik Im
Maschinendau
Postfach 6980
D-76128 Karlsruhe
GERMANY

Harry L. Potma
Royal Netherlands Embassy
Science and Technology
4200 Linnean Avenue, N.W.
Washington DC 20008

Bob R. Powell
North American Operations
Metallurgy Department
Box 9055
Warren MI 48090-9055

Stephen C. Pred
ICD Group, Inc.
1100 Valley Brook Avenue
Lyndhurst NJ 07071

Karl M. Prewo
United Technologies Research Ctr.
411 Silver Lane, MS:24
East Hartford CT 06108

Vimal K. Pujari
Norton Company
SGNICC/NRDC
Goddard Road
Northboro MA 01532-1545

George Quinn
NIST
Ceramics Division, Bldg. 223
Gaithersburg MD 20899

Ramas V. Raman
Ceracon, Inc.
1101 N. Market Boulevard, Suite 9
Sacramento CA 95834

Charles F. Rapp
Owens Corning Fiberglass
2790 Columbus Road
Granville OH 43023-1200

Dennis W. Readey
Colorado School of Mines
Metallurgy and Materials Engr.
Golden CO 80401

Wilfred J. Rebello
PAR Enterprises, Inc.
12601 Clifton Hunt Lane
Clifton VA 22024

Harold Rechter
Chicago Fire Brick Company
7531 S. Ashland Avenue
Chicago IL 60620

Robert R. Reeber
U.S. Army Research Office
P.O. Box 12211
Research Triangle Park NC
27709-2211

K. L. Reifsnider
VPI & SU
Engineering Science and Mechanics
Blacksburg VA 24061

Paul E. Rempes
McDonnell Douglass Aircraft Co.
P.O. Box 516, Mail Code:0642263
St. Louis MO 63166-0516

Gopal S. Revankar
John Deere Company
3300 River Drive
Moline IL 61265

K. Y. Rhee
Rutgers University
P.O. Box 909
Piscataway NJ 08854

James Rhodes
Advanced Composite Materials Corp
1525 S. Buncombe Road
Greer SC 29651

Roy W. Rice
W. R. Grace and Company
7379 Route 32
Columbia MD 21044

David W. Richerson
2093 E. Delmont Drive
Salt Lake City UT 84117

Tomas Richter
J. H. France Refractories
1944 Clarence Road
Snow Shoe PA 16874

Michel Rigaud
Ecole Polytechnique
Campus Universite De Montreal
P.O. Box 6079, Station A
Montreal, P.Q. Quebec H3C 3A7
CANADA

John E. Ritter
University of Massachusetts
Mechanical Engineering Department
Amherst MA 01003

Frank L. Roberge
AlliedSignal Engines
P.O. Box 52180
Phoenix AZ 85072-2180

W. Eric Roberts
Advanced Ceramic Technology, Inc.
990 "F" Enterprise Street
Orange CA 92667

Y. G. Roman
TNO TPD Keramick
P.O. Box 595
Einhoven 5600 AN
HOLLAND

Michael Rossetti
Arthur D. Little, Inc.
15 Acorn Park
Cambridge MA 01240

Barry Rossing
Lanxide Corporation
P.O. Box 6077
Newark DE 19714-6077

Steven L. Rotz
Lubrizol Corporation
29400 Lakeland Boulevard
Wickliffe OH 44092

Robert Ruh
Wright Laboratory
WL/MLLM
Wright-Patterson AFB OH 45433

Robert J. Russell
17 Highgate Road
Framingham MA 01701

Jon A. Salem
NASA Lewis Research Center
21000 Brookpark Road
Cleveland OH 44135

W. A. Sanders
NASA Lewis Research Center
21000 Brookpark Road, MS:49-3
Cleveland OH 44135

J. Sankar
North Carolina A&T State Univ.
Dept. of Mechanical Engineering
Greensboro NC 27406

Yasushi Sato
NGK Spark Plugs (U.S.A.), Inc.
1200 Business Center Drive, #300
Mt. Prospect IL 60056

Maxine L. Savitz
AlliedSignal, Inc.
Ceramic Components
P.O. Box 2960, MS:T21
Torrance CA 90509-2960

Ashok Saxena
GTRI
Materials Engineering
Atlanta GA 30332-0245

David W. Scanlon
Instron Corporation
100 Royall Street
Canton MA 02021

Charles A. Schacht
Schacht Consulting Services
12 Holland Road
Pittsburgh PA 15235

Robert E. Schafrik
National Materials Advisory Board
2101 Constitution Ave., N.W.
Washington DC 20418

James Schienle
AlliedSignal Engines
P.O. Box 52180, MS:1302-2P
Phoenix AZ 85072-2180

John C. Schneider
San Juan Technologies, Inc.
3210 Arena Road
Colorado Springs CO 80921-1503

Gary Schnittgrund
Rocketdyne, BA05
6633 Canoga Avenue
Canoga Park CA 91303

Mark Schomp
Lonza, Inc.
17-17 Route 208
Fair Lann NJ 07410

Joop Schoonman
Delft University of Technology
P.O. Box 5045
2600 GA Delft
THE NETHERLANDS

Robert B. Schulz
U.S. Department of Energy
Office of Transportation Matrls.
CE-34, Forrestal Building
Washington DC 20585

Murray A. Schwartz
Materials Technology Consulting
30 Orchard Way, North
Potomac MD 20854

Peter Schwarzkopf
SRI International
333 Ravenswood Avenue
Menlo Park CA 94025

William T. Schwessinger
Multi-Arc Scientific Coatings
1064 Chicago Road
Troy MI 48083-4297

W. D. Scott
University of Washington
Materials Science Department
Mail Stop:FB10
Seattle WA 98195

Nancy Scoville
Thermo Electron Technologies
P.O. Box 9046
Waltham MA 02254-9046

Thomas M. Sebestyen
U.S. Department of Energy
Advanced Propulsion Division
CE-322, Forrestal Building
Washington DC 20585

Brian Seegmiller
Coors Ceramics Company
600 9th Street
Golden CO 80401

T. B. Selover
AICRE/DIPPR
3575 Traver Road
Shaker Heights OH 44122

Charles E. Semler
Semler Materials Services
4160 Mumford Court
Columbus OH 43220

Thomas Service
Service Engineering Laboratory
324 Wells Street
Greenfield MA 01301

Kish Seth
Ethyl Corporation
P.O. Box 341
Baton Rouge LA 70821

William J. Shack
Argonne National Laboratory
9700 S. Cass Avenue, Bldg. 212
Argonne IL 60439

Peter T.B. Shaffer
Technical Ceramics Laboratories,
4045 Nine/McFarland Drive
Alpharetta GA 30201

Richard K. Shaltens
NASA Lewis Research Center
21000 Brookpark Road, MS:302-2
Cleveland OH 44135

Robert S. Shane
1904 NW 22nd Street
Stuart FL 34994-9270

Ravi Shankar
Chromalloy
Research and Technology Division
Blaisdell Road
Orangeburg NY 10962

Terence Sheehan
Alpex Wheel Company
727 Berkley Street
New Milford NJ 07646

Dinesh K. Shetty
University of Utah
Materials Science and Engineering
Salt Lake City UT 84112

Masahide Shimizu
New Ceramics Association
Shirasagi 2-13-1-208, Nakano-ku
Tokyo 165
JAPAN

Thomas Shreves
American Ceramic Society, Inc.
735 Ceramic Place
Westerville OH 43081-8720

Jack D. Sibold
Coors Ceramics Company
4545 McIntyre Street
Golden CO 80403

Johann Siebels
Volkswagen AG
Werkstofftechnologie
Postfach 3180
Wolfsburg 1
GERMANY

George H. Siegel
Point North Associates, Inc.
P.O. Box 907
Madison NJ 07940

Richard Silberglitt
FM Technologies, Inc.
10529-B Braddock Road
Fairfax VA 22032

Mary Silverberg
Norton Company
SGNICC/NRDC
Goddard Road
Northboro MA 01532-1545

Gurpreet Singh
Department of the Navy
Code 56X31
Washington DC 20362-5101

Maurice J. Sinnott
University of Michigan
5106 IST Building
Ann Arbor MI 48109-2099

John Skildum
3M Company
3M Center
Building 224-2S-25
St. Paul MN 55144

Richard H. Smoak
Smoak & Associates
3554 Hollyslope Road
Altadena CA 91001-3923

Jay R. Smyth
AlliedSignal Engines
111 S. 34th Street, MS:503-412
Phoenix AZ 85034

Rafal A. Sobotowski
British Petroleum Company
Technical Center, Broadway
3092 Broadway Avenue
Cleveland OH 44115

S. Somiya
Nishi Tokyo University
3-7-19 Seijo, Setagaya
Tokyo 157
JAPAN

Boyd W. Sorenson
DuPont Lanxide Composites
1300 Marrows Road
Newark DE 19711

Charles A. Sorrell
U.S. Department of Energy
Advanced Industrial Concepts
CE-232, Forrestal Building
Washington DC 20585

C. Spencer
EA Technology
Capenhurst Chester CH1 6ES
UNITED KINGDOM

Allen Spizzo
Hercules Inc.
Hercules Plaza
Wilmington DE 19894

Richard M. Spriggs
Alfred University
Center for Advanced Ceramic
Technology
Alfred NY 14802

Charles Spuckler
NASA Lewis Research Center
21000 Brookpark Road, MS:5-11
Cleveland OH 44135-3191

M. Srinivasan
Material Solutions
P.O. Box 663
Grand Island NY 14702-0663

Gordon L. Starr
Cummins Engine Company, Inc.
P.O. Box 3005, Mail Code:50182
Columbus IN 47202-3005

Tom Stillwagon
AlliedSignal, Inc.
Ceramic Components
P.O. Box 2960, MS:T21
Torrance CA 90509-2960

H. M. Stoller
TPL Inc.
3754 Hawkins, N.E.
Albuquerque NM 87109

Paul D. Stone
Dow Chemical USA
1776 "Eye" Street, N.W., #575
Washington DC 20006

F. W. Stringer
Aero & Industrial Technology Ltd.
P.O. Box 46, Wood Top
Burnley Lancashire BB11 4BX
UNITED KINGDOM

Thomas N. Strom
NASA Lewis Research Center
21000 Brookpark Road, MS:86-6
Cleveland OH 44135

M. F. Stroosnijder
Institute for Advanced Materials
Joint Research Centre
21020 Ispra (VA)
ITALY

Karsten Styhr
30604 Ganado Drive
Rancho Palos Verdes CA 90274

T. S. Sudarshan
Materials Modification, Inc.
2929-P1 Eskridge Center
Fairfax VA 22031

Glenn J. Sundberg
Norton Company
Goddard Road
Northboro, MA 01532-1545

M. J. Sundaresan
University of Miami
P.O. Box 248294
Coral Gables FL 33124

Patrick L. Sutton
U.S. Department of Energy
Office of Propulsion Systems
CE-322, Forrestal Building
Washington DC 20585

Willard H. Sutton
United Technologies Corporation
Silver Lane, MS:24
East Hartford CT 06108

J. J. Swab
U.S. Army Materials Technology
Ceramics Research Division,
SLCMT-EMC
405 Arsenal Street
Watertown MA 02172

Robert E. Swanson
Metalworking Technology, Inc.
1450 Scalp Avenue
Johnstown PA 15904

Steve Szaruga
Air Force Wright Aeronautical Lab
WL/MLBC
Wright-Patterson AFB OH
45433-6533

Yo Tajima
NGK Spark Plug Company
2808 Iwasaki
Komaki-shi Aichi-ken 485
JAPAN

Fred Teeter
5 Tralee Terrace
East Amherst NY 14051

Monika O. Ten Eyck
Carborundum Microelectronics
P.O. Box 2467
Niagara Falls NY 14302-2467

David F. Thompson
Corning Glass Works
SP-DV-02-1
Corning NY 14831

Merle L. Thorpe
Hobart Tafa Technologies, Inc.
20 Ridge Road
Concord NH 03301-3010

T. Y. Tien
University of Michigan
Materials Science and Engineering
Dow Building
Ann Arbor MI 48103

D. M. Tracey
Norton Company
SGNICC/NRDC
Goddard Road
Northboro MA 01532-1545

L. J. Trostel, Jr.
Box 199
Princeton MA 01541

W. T. Tucker
General Electric Company
P.O. Box 8, Bldg. K1-4C35
Schenectady NY 12301

Masanori Ueki
Nippon Steel Corporation
1618 Ida
Nakahara-Ku Kawasaki 211
JAPAN

Filippo M. Ugolini
ATA Studio
Via Degli Scipioni, 268A
ROMA, 00192
ITALY

Donald L. Vaccari
General Motors Corporation
Allison Gas Turbines
P.O. Box 420, Speed Code S49
Indianapolis IN 46206-0420

Carl F. Van Conant
Boride Products, Inc.
2879 Aero Park Drive
Traverse City MI 49684

Marcel H. Van De Voorde
Commission of the European Comm.
P.O. Box 2
1755 ZG Petten
THE NETHERLANDS

O. Van Der Biest
Katholieke Universiteit Leuven
Dept. Metaalkunde en Toegepaste
de Croylaan 2
B-3030 Leuven
BELGIUM

Michael Vannier
Washington University, St. Louis
510 S. Kings Highway
St. Louis MO 63110

Ara M. Vartabedian
Norton Company
Goddard Road
Northboro, MA 01532-1545

Stan Venkatesan
Southern Coke & Coal Corporation
P.O. Box 52383
Knoxville TN 37950

V. Venkateswaran
Carborundum Company
Niagara Falls R&D Center
P.O. Box 832
Niagara Falls NY 14302

Dennis Viechnicki
U.S. Army Materials Technology
405 Arsenal Street
Watertown MA 02172-0001

Ted Vojnovich
U.S. Department of Energy, ST-311
Office of Energy Research, 3F077P
Washington DC 20585

John D. Volt
E.I. Dupont de Nemours & Co. Inc.
P.O. Box 80262
Wilmington DE 19880

John B. Wachtman
Rutgers University
P.O. Box 909
Piscataway NJ 08855

Shigetaka Wada
Toyota Central Research Labs
Nagakute Aichi 480-11
JAPAN

Janet Wade
AlliedSignal Engines
P.O. Box 52180, MS:1303-2
Phoenix AZ 85072-2180

Jon A. Wade
Norton Company
Goddard Road
Northboro, MA 01532-1545

Richard L. Wagner
Ceramic Technologies, Inc.
537 Turtle Creek South Dr., #24D
Indianapolis IN 46227

J. Bruce Wagner, Jr.
Arizona State University
Center for Solid State Science
Tempe AZ 85287-1704

Daniel J. Wahlen
Kohler, Co.
444 Highland Drive
Kohler WI 53044

Ingrid Wahlgren
Royal Institute of Technology
Studsvik Library
S-611 82 Nykoping
SWEDEN

Ron H. Walecki
AlliedSignal, Inc.
P.O. Box 2960, MS:T21
Torrance CA 90509-2960

Michael S. Walsh
Vapor Technologies Inc.
6300 Gunpark Drive
Boulder CO 80301

Chien-Min Wang
Industrial Technology Research Institute
195 Chung-Hsing Road, Sec. 4
Chutung Hsinchu 31015 R.O.C.
TAIWAN

Robert M. Washburn
ASMT
11203 Colima Road
Whittier CA 90604

Gerald Q. Weaver
Carborundum Specialty Products
42 Linus Allain Avenue
Gardner MA 01440-2478

Kevin Webber
Toyota Technical Center, U.S.A.
1410 Woodridge, RR7
Ann Arbor MI 48105

Karen E. Weber
Detroit Diesel Corporation
13400 Outer Drive West
Detroit MI 48239-4001

James K. Weddell
Du Pont Lanxide Composites Inc.
P.O. Box 6100
Newark DE 19714-6100

R. W. Weeks
Argonne National Laboratory
MCT-212
9700 S. Cass Avenue
Argonne IL 60439

Ludwig Weiler
ASEA Brown Boveri AG
Eppelheimer Str. 82
D-6900 Heidelberg
GERMANY

James Wessel
Dow Corning Corporation
1800 "M" Street, N.W., #325 South
Washington DC 20036

Robert D. West
Therm Advanced Ceramics
P.O. Box 220
Ithaca NY 14851

Thomas J. Whalen
Ford Motor Company
SRL Bldg., Mail Drop 2313
P.O. Box 2053
Dearborn MI 48121-2053

Charles S. White
Norton Company
Goddard Road
Northboro, MA 01532-1545

Ian A. White
Hoeganaes Corporation
River Road
Riverton NJ 08077

Sheldon M. Wiederhorn
NIST
Building 223, Room A329
Gaithersburg MD 20899

John F. Wight
Alfred University
McMahon Building
Alfred NY 14802

D. S. Wilkinson
McMaster University
1280 Main Street, West
Hamilton Ontario L8S 4L7
CANADA

James C. Williams
General Electric Company
Engineering Materials Technology
One Neumann Way, Mail Drop:H85
Cincinnati OH 45215-6301

Steve J. Williams
RCG Hagler Bailly, Inc.
1530 Wilson Boulevard, Suite 900
Arlington VA 22209-2406

Thomas A. Williams
National Renewable Energy Lab
1617 Cole Boulevard
Golden CO 80401

Craig A. Willkens
Norton Company
SGNICC/NRDC
Goddard Road
Northboro MA 01532-1545

Roger R. Wills
TRW, Inc.
Valve Division
1455 East 185th Street
Cleveland OH 44110

David Gordon Wilson
Massachusetts Institute of Technology
77 Massachusetts Ave., Room 3-455
Cambridge MA 02139

Matthew F. Winkler
Seaworthy Systems, Inc.
P.O. Box 965
Essex CT 06426

Gerhard Winter
Hermann C. Starck Berlin GmbH
P.O. Box 25 40
D-3380 Goslar 3380
GERMANY

William T. Wintucky
NASA Lewis Research Center
Terrestrial Propulsion Office
21000 Brookpark Road, MS:86-6
Cleveland OH 44135

Thomas J. Wissing
Eaton Corporation
Engineering and Research Center
P.O. Box 766
Southfield MI 48037

James C. Withers
MER Corporation
7960 S. Kolb Road
Building F
Tucson AZ 85706

Dale E. Wittmer
Southern Illinois University
Mechanical Engineering Department
Carbondale IL 62901

Warren W. Wolf
Owens Corning Fiberglass
2790 Columbus Road, Route 16
Granville OH 43023

Egon E. Wolff
Caterpillar Inc.
Technical Center
P.O. Box 1875
Peoria IL 61656-1875

George W. Wolter
Howmet Turbine Components Corp.
Technical Center
699 Benston Road
Whitehall MI 49461

James C. Wood
NASA Lewis Research Center
21000 Brookpark Road, MS:86-6
Cleveland OH 44135

Marrill Wood
LECO Corporation
P.O. Box 211688
Augusta GA 30917-1688

Wayne L. Worrell
University of Pennsylvania
3231 Walnut Street
Philadelphia PA 19104

John F. Wosinski
Corning Inc.
ME-2 E-5 H8
Corning NY 14830

Ian G. Wright
BCL
505 King Avenue
Columbus OH 43201

Ruth Wroe
ERDC
Capenhurst Chester CH1 6ES
ENGLAND

Bernard J. Wrona
Advanced Composite Materials Corp
1525 S. Buncombe Road
Greer SC 29651

Carl C. M. Wu
Naval Research Laboratory
Ceramic Branch, Code 6373
Washington DC 20375

John C. Wurst
U. of Dayton Research Institute
300 College Park
Dayton OH 45469-0101

Neil Wyant
ARCH Development Corp.
9700 S. Cass Avenue, Bldg. 202
Argonne IL 60439

Roy Yamamoto
Texaco Inc.
P.O. Box 509
Beacon NY 12508-0509

John Yamanis
AlliedSignal Aerospace Company
P.O. Box 1021
Morristown NJ 07962-1021

Harry C. Yeh
AlliedSignal, Inc.
Ceramic Components
P.O. Box 2960, MS:T21
Torrance CA 90509-2960

Hiroshi Yokoyama
Hitachi Research Lab
4026 Kuji-Cho
Hitachi-shi Ibaraki 319-12
JAPAN

Thomas M. Yonushonis
Cummins Engine Company, Inc.
P.O. Box 3005, Mail Code 50183
Columbus IN 47202-3005

Thomas J. Yost
Corning Inc.
Technical Products Div., 21-1-2
Corning NY 14831

Jong Yung
Sundstrand Aviation Operations
4747 Harrison Avenue
Rockford IL 61125

A. L. Zadoks
Caterpillar Inc.
Technical Center, Building L
P.O. Box 1875
Peoria IL 61656-1875

Avi Zangvil
University of Illinois
104 S. Goodwin Avenue
Urbana IL 61801

Charles H. Zenuk
Transtech
6662 E. Paseo San Andres
Tucson AZ 85710-2106

Carl Zweben
General Electric Company
P.O. Box 8555, VFSC/V4019
Philadelphia PA 19101

Department of Energy
Oak Ridge Operations Office
Assistant Manager for Energy
Research and Development
P.O. Box 2001
Oak Ridge, TN 37831-8600

Department of Energy (2)
Office of Scientific and
Technical
Information
Office of Information Services
P.O. Box 62
Oak Ridge, TN 37831

For distribution by microfiche as shown in DOE/OSTI-4500, Distribution Category UC-332 (Ceramics/Advanced Materials).